THE UNIVERSITY OF NOTTINGHAM

NOTTINGHAM GEOSPATIAL INSTITUTE

ESTIMATION AND ANALYSIS OF MULTI GNSS DIFFERENTIAL CODE BIASES USING A HARDWARE SIGNAL SIMULATOR

MUHAMMAD AMMAR

BE (CIVIL), MSC (ENGINEERING SURVEYING)

Thesis submitted to the University of Nottingham for the degree of Doctor of Philosophy

2018

ABSTRACT

The ionosphere has the largest contribution to the Global Navigation Satellite System (GNSS) error budget. Its background effect can be mostly modelled, but sharp gradients in its Total Electron Content (TEC) adversely affect differential GNSS due to error decorrelation. Furthermore, irregularities in the ionosphere cause signal fluctuations known as scintillation, which may lead to cycle slips, accuracy degradation and even loss of receiver lock on satellite. In the last few decades, specialized GNSS Ionospheric Scintillation Monitor Receivers (ISMRs) have been developed with a view to support continuous ionospheric monitoring and modelling by estimating TEC and different scintillation parameters, and to help develop future receivers with robust tracking under extreme ionospheric conditions. However, it is not a straight forward task to derive accurate TEC information from these specialized receivers because the recorded pseudorange measurements are contaminated by instrumental biases, the so-called Differential Code Biases (DCBs).

The Nottingham Geospatial Institute (NGI) – former Institute of Engineering Surveying and Space Geodesy (IESSG) – pioneered and currently undertakes scintillation and TEC monitoring in Northern Europe using dual frequency GPS receivers, the NovAtel/AJ Systems GSV4004, and in the last decade the relatively new multi-frequency multi-constellation Septentrio PolaRxS Pro receivers. Considering the hardware delays existing within these scintillation monitors to be stable for reasonable periods of time, the recorded TEC measurements have been used quite successfully on a relative basis in a number of experiments. Yet, to enable the calculation of absolute TEC, either for ionospheric monitoring or to facilitate non-differential positioning techniques such as Precise Point Positioning (PPP), these (and indeed any other conventional multi-frequency) receivers must be calibrated to account for their respective DCBs.

The research work presented in this thesis has been carried out in two main phases. The first phase involves estimating the DCB of a multi frequency, multi constellation GNSS receiver (such as the Septentrio PolaRxS Pro) using a hardware signal simulator, whereby the state of the ionosphere and other variables can be controlled. It has been shown that a hardware signal simulator such as the Spirent GSS8000 can be used effectively to estimate a consistent and more realistic set of DCBs between different signal pairs for any multi frequency, multi constellation receiver.

The second phase replicates the procedure carried out by the International GNSS Service (IGS) or the Multi GNSS EXperiment (MGEX) to determine receiver and satellite DCBs in a global ionospheric analysis using the IGS/MGEX network. By including the calibrated receiver from the first phase in this network, it has been proved that for all practical purposes of ionospheric modelling, using the 'known' receiver DCB of that receiver as an external constraint, is a valid approach to resolving the rank deficiency problem that arises in DCB estimation for receiver/satellite networks.

One final aspect that this research aims to address was the possible benefit of estimated DCBs in PPP processing. From initial investigations, no plausible benefit was observed and hence it was decided not to proceed further because of time constraints. The indications are that the effect of the estimated DCBs cannot be observed in PPP while working with the Ionospheric Free (IF) combination, whereas in the case of PPP based on uncombined raw observations, the estimated DCBs derived from relatively noisy pseudoranges in comparison to the carrier phase observations, are not of sufficient accuracy to be used for correcting the ionospheric delay. This needs to be further investigated in future.

ACKNOWLEDGEMENTS

Indeed, all praises and glory are for Allah Almighty, the Creator of the Universe and my every success and achievement is due to His mercy and favour.

First, I would like to specially thank my main supervisor, Dr Marcio Aquino and my co-supervisors, Dr Sreeja Vadakke Veettil and Dr Marcus Andreotti, who have borne the brunt of my relentless and never-ending questions. Their guidance, understanding of the subject and patience surely made this research a fascinating and well-rounded experience for me.

I would like to thank my colleagues at Nottingham Geospatial Institute and especially Francesco Basile, who have facilitated and contributed to my research. A special shout out to Jean-Marie Sleewaegen at Septentrio for his invaluable feedback and guidance to my research queries.

I would like to express my deepest gratitude to the National University of Sciences and Technology (NUST), Pakistan, and to the Faculty of Engineering, the University of Nottingham, United Kingdom (UK), for sponsoring this research and providing me this precious opportunity to pursue my doctorate dream at one of the finest institutes in UK. I believe I would not have been able to achieve this milestone without their cooperation & financial support.

Last but not least, I would like to thank my spouse, my kids, my parents and my siblings for their prayers, love, patience and never-ending support. I hereby dedicate this dissertation to all the wonderful people who have either directly or indirectly contributed to this research.

PAPER PUBLISHED

Ammar, M., Aquino, M., Vadakke Veettil, S. and Andreotti, M. (2018) Estimation and Analysis of Multi GNSS Differential Code Biases Using a Hardware Signal Simulator, *GPS Solutions*, 22: 32. https://doi.org/10.1007/s10291-018-0700-7. (See Appendix A)

TABLE OF CONTENTS

CONSTANTS AND PARAMETERS

$\overrightarrow{B_0}$:	Geomagnetic field vector, B ≈ 3.12×10^{-5} T (i.e. magnitude of $\overrightarrow{B_0}$ on the surface of the Earth at the geomagnetic equator) [Tesla, T = kg / (C.s) where C: Coulomb]
c =	299792458 m/s, speed of light
e =	1.60218×10^{-19} C
ϵ_o=	$8.85418782 \times 10^{-12}$ $C^2 N^{-1} m^{-2}$ (C: Coulomb, N: Newton)
f =	c / λ, Carrier frequency of GNSS signals (λ: signal wavelength)
f_{L1} =	1575.42 MHz (GPS and Galileo share this frequency)
f_{L2} =	1227.6 MHz (GPS only)
f_{L5} =	1176.45 MHz (GPS and Galileo share this frequency)
κ =	$e^2/8\pi^2 \epsilon_o m_e = 40.3$ m^3s^{-2} (Constant Term)
m_e =	9.10939×10^{-31} kg
μ_o=	$4\pi \times 10^{-7}$ $WbA^{-1}m^{-1}$ (Wb: Webers, A: Ampere)
N_e :	Electron number density (at a point in the ionosphere)

ACRONYMS

AC	Analysis Centre
ACU	Auto Calibration Utility
ADC	Analog/Digital Converter
AFRL	Air Force Research Laboratory
AGC	Automatic Gain Control
ANOVA-I	One Way Analysis of Variance
B_{GD}	Broadcast Group Delay (Galileo)
C/N0	Signal to Noise Ratio
C1	Civilian C/A code on GPS L1 carrier
CODE	Center for Orbit Determination in Europe
CIGALA	Concept for Ionospheric-Scintillation Mitigation for Professional GNSS in Latin America
DCB	Differential Code Bias
DLL	Delay Locked Loop
DSP	Digital Signal Processing
E1	Code on Galileo L1 Carrier
E5a	Code on Galielo L5 Carrier
EM	Electromagnetic
ESA	European Space Agency
ESOC	European Space Operations Centre
EUV	Extreme Ultraviolet
FPGA	Field-Programmable Gate Array
gAGE	group of Astronomy and GEomatics
GEONET	GPS Earth Observation Network
GIM	Global Ionospheric Map

GNSS	Global Navigation Satellite System
GSV	GPS Silicon Valley
GUI	Graphical User Interface
HF	High Frequency
IFB	Inter-Frequency Bias
IGGCAS	Institute of Geology and Geophysics, Chinese Academy of Sciences
IGS	International GNSS Service
IOV	In Orbit Validation
IPP	Ionospheric Pierce Point
IQR	Interquartile Range
ISMR	Ionospheric Scintillation Monitor Receiver
JPL	Jet Propulsion Laboratory
IESSG	Institute of Engineering Surveying and Space Geodesy
IONEX	IONosphere Map Exchange Format
L1	GPS L1 Carrier (f_{L1}) – Similar to Galileo L1 Carrier
L2	GPS L2 Carrier (f_{L2})
L5	GPS L5 Carrier (f_{L5}) – Similar to Galileo L5 Carrier
LSQ	Least Squares
MCU	Multi-box Combiner Unit
MF	Mapping Function
MGEX	Multi GNSS Experiment
MSLM	Modified Single Layer Model
NGI	Nottingham Geospatial Institute
OCXO	Oven Controlled Crystal Oscillator
P1	Precision code on L1 carrier
P2	Precision code on L2 carrier

PLL	Phase Locked Loop
PPP	Precise Point Positioning
PRN	Pseudo Random Noise
RF	Radio Frequency
RINEX	Receiver Independent Exchange Format
SBAS	Satellite Based Augmentation System
SBIR	Small Business Innovative Research
SGC	Signal Generator Chassis
STEC	Slant Total Electron Content
SH	Spherical Harmonics
TCXO	Temperature Controlled Crystal Oscillator
TEC	Total Electron Content (= 10^{16} electrons-metre^{-2})
TECU	TEC Units
T_{GD}	Estimated Group Delay Differential
TOW	Time of Week
UPC	Technical University of Catalonia
UT	Universal Time
UNESP	Universidade Estadual Paulista
VTEC	Vertical Total Electron Content
ZM	Zero Mean

LIST OF FIGURES

LIST OF TABLES

CHAPTER 1

INTRODUCTION

The ionosphere has the largest contribution to the Global Navigation Satellite System (GNSS) error budget. Its background effect can be mostly modelled, but sharp gradients in its Total Electron Content (TEC) adversely affect differential GNSS due to error decorrelation. Furthermore, irregularities in the ionosphere cause signal fluctuations known as scintillation, which may lead to cycle slips, accuracy degradation and even loss of receiver lock on satellite. In the last few decades, specialized GNSS Ionospheric Scintillation Monitor Receivers (ISMRs) have been developed with a view to support continuous ionospheric monitoring and modelling by estimating TEC and different scintillation parameters, and to help develop future receivers with robust tracking under extreme ionospheric conditions. However, it is not a straight forward task to derive accurate TEC information from these specialized receivers because, just like conventional GNSS receivers, the recorded pseudorange and carrier phase measurements are contaminated by instrumental biases or hardware delays. These are frequency dependent delays which the GNSS signals experience while passing through the radio frequency (RF) circuitry and the different components of the satellite and the receiver hardware. The situation becomes more complicated as these code and phase delays are not only frequency dependent but also not measurable in an absolute sense. Keeping that in consideration, if accurate TEC values are required, these hardware delays for every possible GNSS signal need to be estimated and removed. To get around the problem of inaccessible absolute delays, in the case of code pseudoranges, one must rely on the difference of two individual code delays existing between two codes on the same signal (i.e. intra frequency bias) as in the case of C1 and P1, or between two codes on two different carrier signals (i.e. inter frequency bias) as in the case of P1 and P2. These inter and intra frequency biases are frequently referred to as the Differential Code Biases (DCBs). Depending upon whether they refer to either satellite or receiver, these can be further categorised into satellite and receiver DCBs (Wilson and Mannucci, 1993). Working with the legacy GPS signals, ignoring the satellite and receiver DCBs when computing TEC may result in an error of up to 20 TECU (or 7 ns) for satellites and 40 TECU (or 14 ns) for receivers, and their cumulative effect can reach as much as 100 TECU (or 35 ns) in many cases (Sardón et al., 1994). If not accounted for, these can also sometimes lead to physically meaningless negative TEC values (Ma and Maruyama, 2003; Mylnikova et al., 2015). This could become even worse for the more recent GNSS signals such as in the case of Galileo, where receiver DCB values in the order of 263 TECU (or 100 ns) had been found to exist between E1 and E5b signals (Montenbruck et al., 2014; Wang et al., 2015). So, for precise and accurate ionospheric modelling, these cannot be ignored and must be properly estimated and applied. On the other hand, in the case of carrier phase observations, the situation is more complex because of the presence of ambiguities. The inter frequency phase biases are not studied herein, as they are considered to be beyond the scope of this research.

1.1. **Motivation of the Research**

The Nottingham Geospatial Institute (NGI) – former Institute of Engineering Surveying and Space Geodesy (IESSG) – pioneered and currently undertakes scintillation and TEC monitoring in Northern Europe using dual frequency GPS receivers such as the NovAtel/AJ Systems GSV4004, and the relatively new multi-frequency multi-constellation Septentrio PolaRxS Pro receivers. Considering the hardware delays existing within these scintillation monitors to be stable for reasonable periods of time, the recorded TEC measurements have been used quite successfully on a relative basis in a number of experiments. Yet, to enable the calculation of absolute TEC for ionospheric monitoring, these receivers must be calibrated to account for their respective DCBs. In terms of multi-frequency multi-constellation conventional receivers, this will also facilitate precise GNSS applications such as high-precision GNSS satellite clock estimation, time transfer among GNSS observing stations and code-based resolution of carrier phase ambiguities (Dach et al., 2007).

With the advent of modernized GPS, GLONASS and the new Galileo and Beidou signals in addition to the legacy GPS and GLONASS signals, a variety of signal pairs is available to the users to compute TEC. However, the associated DCBs and different available tracking modes such as pilot only and combined, make the accurate TEC computation even more challenging.

In positioning, the receiver DCBs are frequently ignored as these are absorbed in the estimated receiver clock offset but the same cannot be done with the satellites DCB. This is because of the fact that both the broadcast and precise satellite clocks are derived from a linear ionospheric free combination of the satellite code biases. Hence while estimating position, the satellite DCBs must be properly applied by deriving them from either the broadcast ephemeris (Estimated Group Delay Differential or 'T_{GD}' parameter in GPS / Broadcast

Group Delay or 'B_{GD}' parameter in Galileo) or retrieved from the International GNSS Service (IGS) published DCB products. What is important here is to maintain consistency between the broadcast or precise clock products and the respective satellite DCBs from which these are derived. To facilitate the GNSS users, the DCB products are routinely estimated and published online free of charge by different Analysis Centres (ACs) of the IGS as a by-product of their local or global ionospheric analyses for all the available satellites in different constellations and a selected number of IGS or MGEX (Multi GNSS Experiment) stations. These are reported as part of Global Ionosphere Maps (GIMs) in Ionosphere map Exchange format – IONEX (Schaer et al., 1998) or as independent DCB products. A linear geometric combination of code based pseudoranges is employed by the ACs to derive the DCBs on a daily basis along with a set of ionospheric coefficients. However, the solution of this system by Least Squares has a rank defect and an external constraint must be employed to break this rank deficiency and enable to separate the satellite DCBs from the receiver DCBs. This is achieved by the various ACs of the IGS by constraining the mean of the satellites DCBs to zero, in a so-called 'zero mean (ZM)' constraint. Consequently, with the routine changes carried out in the satellite constellations, frequent jumps can be observed in the estimated DCBs because of the fluctuation in this arbitrary ZM reference (Zhong et al., 2015). In contrast to this, rather than assuming the artificial ZM constraint, the problem of rank deficiency can also be resolved by constraining the solution to a known receiver DCB in the network instead. The advantage of using this approach is that a more realistic and stable set of satellite and receiver DCBs is estimated. Apart from receiver calibration, this research also aims at investigating the electronics/signal processing taking place within the satellite and the receiver hardware.

For global TEC monitoring and other related applications, it would be quite convenient to select a receiver in the IGS or MGEX network which would result in the regular estimation of its DCB. However, as in a general situation this receiver will not be part of the network, its DCB must be obtained from the manufacturer or otherwise carefully estimated through a technique that can ensure consistency with the available published set of satellite DCBs. So, the primary motivation of this research is to estimate the DCB of a single receiver for all available GNSS signal pairs using a hardware signal simulator while considering the impact of all variables involved and then to include this receiver, whose DCB is now known, in a global network of stations to estimate the DCBs of all the satellites and stations involved.

Based on the discussion presented above, the research work has been carried out in two different phases. The first phase involved establishing a standard procedure to determine the DCB of a Septentrio PolaRxS Pro scintillation receiver available at the NGI, with a view to pave the way for estimating these biases for any multi frequency, multi constellation GNSS receiver. The approach that was pursued in DCB estimation is through simulation, where the state of the ionosphere and other variables can be controlled using a hardware signal simulator such as the Spirent GSS8000 or the Spirent GSS9000. This allowed the receiver bias to be isolated (for different signal pairs), but brought in additional problems such as biases existing within the simulator or biases coming from the associated equipment, such as antenna, cable, connectors, etc.

(Ammar, 2011). Once the calibration procedure was established, it can be applicable for calibrating any conventional multi-frequency, multi-constellation GNSS receiver. In the second phase, the procedure as followed by the IGS or the MGEX to estimate the satellite and receiver DCBs in a global ionospheric analysis, was replicated. This was done by collecting open sky data with the calibrated receiver and then processing it along with other IGS or MGEX stations to estimate the satellite and receiver DCBs of the entire network. Two additional multi-frequency and multi-constellation receivers were also brought into the research to validate the DCB estimates from the first stage. One last aspect of the research was to try to assess the possible impact of the estimated DCBs in PPP processing.

1.2. **Aims and Objectives**

The main aims and objectives of this research are as follows:

1) Working with GPS legacy signals, establish a standard procedure for determining the calibration parameters in terms of DCBs of any multi-frequency, multi constellation GNSS receiver by:
    - Investigating the internal biases existing between the different channels of the hardware signal generator, their influence on the receiver DCB and estimating necessary correction parameters.
    - Exploring the effect of the connecting cable and other miscellaneous hardware on the receiver DCB and estimating necessary correction parameters.
2) Repeat 1) by working with modernised GPS and new Galileo signals.

3) Working with GPS (both legacy and modernised) signals and new Galileo signals, devise a strategy to estimate the satellite and the receiver DCBs in a global network of stations by incorporating the calibrated receiver from 1) and 2).
4) Working with GPS (both legacy and modernised) signals and new Galileo signals, draw a comparison between the DCBs as estimated in 3) using different external constraints.
5) Provide initial insight on the possible impact of the estimated DCBs in PPP processing.

1.3 **Literature Overview**

1.3.1 **Previous work at NGI**

The NGI has been monitoring TEC and ionospheric scintillation in Northern Europe since June 2001 using GPS dual frequency NovAtel/AJ Systems GSV4004 receivers (Aquino, 2005). For accurate TEC computation, these TEC and scintillation monitors must be calibrated and supplied with a parameter 'TEC_{CAL}' i.e. the user defined TEC offset to account for L_1/L_2 differential delay (GPS Silicon Valley, 2004). Dodson et al. (2001) demonstrated an empirical way of determining TEC_{CAL} based on comparing the TEC given by the monitor with TEC given by the Bernese software as extracted from a co-located dual frequency receiver.

In 2010, NGI in collaboration with Universidade Estadual Paulista (UNESP), Brazil, carried out an investigation to study the influence of different cable lengths on receiver DCB estimation using a hardware signal simulator. However, this research did not result in any publication.

The current PhD research follows on from the work of Ammar (2011), in which an attempt was made to establish the calibration parameters in terms of DCBs for both the GSV4004 and PolaRxS Pro ISMRs using the Spirent GSS8000 hardware signal simulator. The important conclusions drawn from that research were as follows:

- The hardware signal simulator such as Spirent GSS8000 can be effectively used to remove the ionospheric delay experienced by the different signals and their respective modulations.
- The estimation of the receiver DCB is corrupted by the hardware delays originating within the simulator and the connecting cable.
- If accurate results are to be achieved while working with a hardware signal simulator, it is important to account for the systematic errors coming from the simulator channels and associated equipment such as antenna cable, splitter, etc.
- The TEC measurements made by the PolaRxS Pro receiver are too noisy if unsmoothed pseudoranges are used. So, a note of caution is made to use it with appropriate care.
- As opposed to the PolaRxS Pro, TEC measurements made by the GSV4004 receivers are relatively smooth but once the Code/Carrier divergence plots on different carrier signals are drawn, they show large divergence even when the ionosphere is correctly set to zero. So, the

GSV4004 monitor must be used with caution in any future calibration research.

1.3.2 **Previous work elsewhere**

Van Dierendonck (1999) and Van Dierendonck and Hua (2001) defined a calibration procedure for GSV4004 monitors, by comparing their estimated TEC data with a 'reference' TEC, such as that generated by the IGS or a Satellite Based Augmentation System (SBAS), an approach attempted in Dodson et al. (2001).

Calibration of receivers is directly related with the estimation of the satellite and receiver DCBs which is a time-consuming process that depends on the following assumptions (Ma and Maruyama, 2003):

- The electron distribution lies in a thin shell at a fixed height above the Earth;
- The TEC is time-dependent in a reference frame fixed with reference to the Earth-Sun axis;
- The satellite and receiver biases are constant over several hours.

In the early days, the ionosphere was observed with a single GPS receiver, the instrumental biases and the TEC were assessed by modelling TEC as a polynomial of latitude and longitude based on the assumption of a smooth ionospheric behaviour (Lanyi and Roth, 1988; Coco et al., 1991). Later with both day time and night time data from several GPS receivers, the TEC and the biases were simulated with a random walk stochastic process and solved by using a Kalman filter approach (Sardon et al., 1994; Sunehra et al., 2010). Based on a spherical surface harmonic expansion of the TEC in latitude and longitude, the instrumental biases were removed, and the Northern hemisphere map of TEC was obtained with an early sparse global GPS network of just 30 stations (Wilson et al., 1995). With the global network of over 100 GPS receivers, the Jet Propulsion Laboratory (JPL) models the vertical TEC in a solar-geomagnetic reference frame using bi-cubic splines on a spherical surface of 2.5° by 5.0° latitude and longitude. Then a Kalman filter is applied to solve simultaneously for TEC and instrumental biases (Mannucci et al., 1998; Iijima et al., 1999). Using around 300 GPS receivers selected homogeneously from the GPS Earth Observation Network (GEONET) in Japan, and assuming that the TEC is identical at any point within a 2° by 2° grid block, the TEC over Japan and instrumental biases were determined with a least squares (LSQ) fitting technique (Ma and Maruyama, 2003). A similar approach has been used by Ma et al. (2014) to determine DCBs of all the GPS satellites and 4 GPS receivers located in the equatorial anomaly region in southeast China. So, based on the distribution of GPS stations included in the estimation process, the different methods presented above can be classified into methods focusing on global, regional or single GPS station (Zhang et al., 2014).

To conclude, different algorithms have been proposed in the past for estimating the DCBs and for single station receiver DCB estimation, these can be roughly categorized in two groups (Arikan et al., 2008; Komjathy et al., 2005; Li et al., 2014, Li et al., 2017). The first group models Vertical TEC (VTEC) as a polynomial that is a function of ionospheric pierce point coordinates in a coordinate system referenced to the earth-sun axis. Both the satellite and receiver DCBs are considered as unknowns along with other coefficients and are solved for in a LSQ solution (Lanyi and Roth, 1988; Sardón et al., 1994; Jakowski et al., 1996; Lin, 2001; Otsuka et al., 2002, Rao, 2007; Yuan et al., 2007; Mayer et al., 2011; Durmaz and Karslioglu, 2015). The second group uses the method of minimization of the standard deviation of VTEC using different receiver trial biases and the one that minimizes the standard deviation of computed VTEC is chosen as the receiver bias for that particular station (Ma and Maruyama, 2003; Zhang et al., 2003; Komjathy et al., 2005; Arikan et al., 2008, Montenbruck et al., 2014). Because of the underlying assumptions, all these estimation techniques have their own limitations. The ionosphere exhibits both spatial and temporal variations under the impact of space weather and this in turn can seriously degrade the precision of the estimated DCB from the GNSS data. Zhang et al. (2009) statistically studied the differences of the instrumental biases estimated from the GPS data between active and quiet geomagnetic days and found that the RMS of receiver DCBs estimated on active days is larger than that on quiet days. Zhang et al. (2010) also statistically studied the precision of instrumental biases estimated from GPS data observed in middle and low latitude regions and found that the receiver DCBs estimated in low latitude were more variable than those in middle latitude, which was attributed to the difference of the ionospheric morphology between low and middle latitudes.

As per Hernandez-Pajares et al. (2009), the IGS analysis centres, namely, the Centre for Orbit Determination in Europe (CODE), University of Berne, Switzerland; JPL, Pasadena, CA, USA; European Space Operations Centre (ESOC) of European Space Agency (ESA), Darmstadt, Germany; and research group of Astronomy and GEomatics (gAGE) of Technical University of

Catalonia (UPC), are actively involved in producing VTEC maps along with the DCBs for all the satellites and a few of the IGS stations using different approaches (Schaer, 1999; Feltens, 1998, 2007; Mannucci et al., 1998, Hernandez-Pajares et al., 1997) and these are made available to IGS in an agreed IONEX format with a resolution of 2 hour, 5° and 2.5° in time, longitude and latitude respectively. Most of the IGS receiver DCBs provided in the IONEX files are monthly averages of daily values and do not represent the daily variations (Arikan et al., 2008). Also, the DCB values provided by these IGS analysis centres in IONEX files are not always in accordance with each other (Brunini et al., 2005). In terms of accuracy, the GIMs have a quoted accuracy of 2-9 TECU, whereas, the DCBs have a not so well-defined accuracy of few tenths of a nanosecond (Dyrud et al., 2008). In the global ionospheric analysis, the satellite and receiver specific DCBs are separated based on the assumption of additive biases and zero-mean condition for the satellite biases within a constellation (Montenbruck et al., 2014). As per Schaer (1999), this is because only the relative DCBs (e.g. relative to a reference satellite) affect ionospheric mapping and single-point positioning and hence the zero mean represents a very stable but virtual bias. Also, in this way, the satellite DCBs are in fact more accurately determined than the receiver DCBs, provided a network of many receivers is processed. It is because a receiver DCB is only observed by the corresponding receiver itself, whereas, a satellite DCB is theoretically observed by all the involved receivers at least on a 24 hours basis.

TEC mismodeling is another factor that can lead to less accurate receiver DCB (especially for equatorial stations attributed to the marked dynamics of the equatorial ionosphere or the bad receiver performance in that region) than a satellite DCB because the entire TEC above each receiver is relevant (Schaer, 1999). On the whole, it is envisaged that both the short-term and long-term variations in IGS computed DCBs are influenced by the ionospheric variability (Zhang et al., 2014) in addition to a shift produced in the common DCB reference because of the changes carried out in satellite constellations (Zhong et al., 2015). Similar to the CODE strategy, a MATLAB based tool was developed by Jin et al. (2012) to estimate global or regional GNSS satellite and receiver DCBs. This open access tool has been modified in this research to include the newer GNSS signals and to work with the 'known' receiver DCB constraint in addition to the ZM constraint in the estimation of network DCBs. The detailed description of this tool is presented in Section 3.5.

Absolute satellite and receiver DCBs cannot be measured directly by any existing practical method and therefore it has been common practice to estimate these biases from a variety of techniques as presented earlier. These biases are however crucial for accurate TEC estimation and for non-differential GNSS techniques such as PPP. Therefore, this research is relevant because it introduces a technique for satellite and receiver DCB estimation by first estimating the DCB of a reference receiver through simulation and subsequently 'inserting' this receiver in a global network for processing. For this, a Septentrio PolaRxS Pro ISMR, referred to hereafter as 'SEPT', was used in conjunction with the Spirent GSS8000 hardware simulator, in a simulation where the state of the ionosphere, troposphere and the other group delays could be controlled, as demonstrated in Ammar (2011). Once the DCB of this receiver has been estimated, it is then used to constrain the solution in a global network of stations following the strategy implemented by the CODE, to ultimately estimate the DCBs of all the satellites and the receivers involved in the network. The final results should produce a consistent set of stable DCBs, which are closer to their physical values and therefore more realistic use in TEC monitoring applications. For validation purposes, another Septentrio PolaRxS Pro ISMR and a Javad Triumph–I receiver were also exploited. These are referred to hereafter as 'SEP2' and 'JAVD', respectively. Moreover, the idea of working with an ISMR as a primary receiver was originally conceived because of the specific feature of this receiver to estimate TEC for ionospheric monitoring purposes, where the estimation of DCBs is desirable so that absolute and calibrated TEC i.e. the one corrected for DCBs, can be obtained. It is also believed that the performance of the ISMRs in terms of hardware configuration is better than the geodetic receivers, based on the following key points:

- The ISMR is equipped with a better and more stable oven-controlled clock i.e. Oven Controlled Crystal Oscillator (OCXO) as opposed to geodetic receiver which has a temperature-controlled clock i.e. Temperature Controlled Crystal Oscillator (TCXO). A better clock will make the receiver more robust against variations of the satellite signals. Under ideal circumstances, assuming a text-book receiver design, it is agreed that the receiver clock noise would cancel entirely. However, receivers may not be designed as such, e.g. it is generally assumed that the signals are converted from analog to digital domain by a single Analog/Digital Converter (ADC), which may not be the case. In the case of more than one ADC (e.g. one for

L1, one for L2), then this means that the receiver 'clock' is no longer exactly the same for each frequency in the receiver, therefore affecting inter-frequency biases. In this case, a receiver that has a more stable, less jittery clock will have a more stable 'clock' throughout the receiver's conversion and processing system. Figure 1.1, as presented by Sleewaegen (2012), consolidates the above statement and the effectiveness of using an OCXO over TCXO during scintillation monitoring (see Section 2.2 for detailed explanation about scintillation).

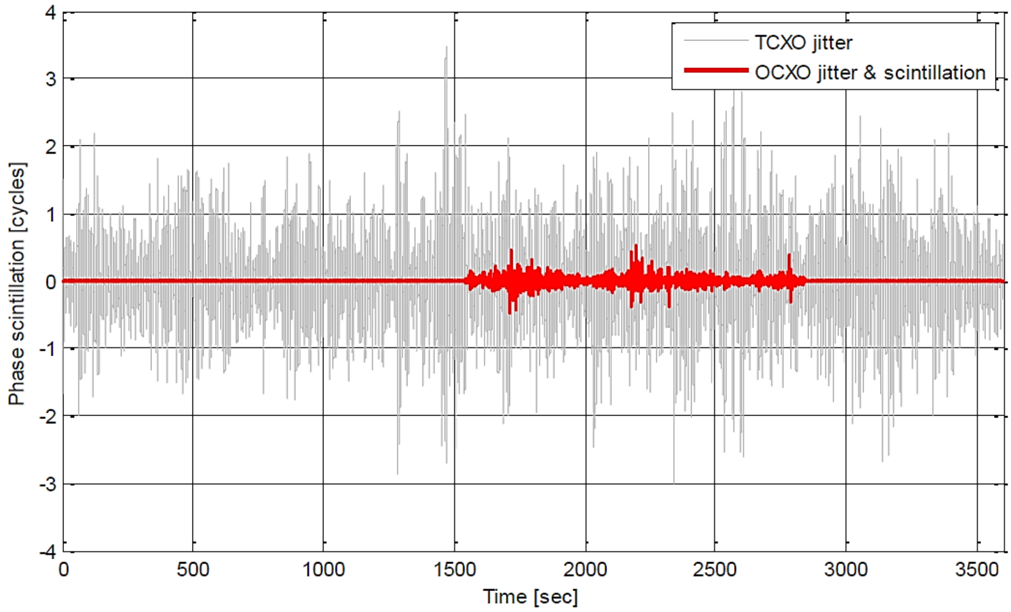

Fig. 1.1 Comparison of TCXO and OCXO jitters during a scintillation event (Sleewaegen, 2012)

- According to Andreotti (2016), if the GNSS signal propagation is affected by ionospheric effects, an ISMR (with a more stable clock) has a better chance to estimate the ionospheric errors than a geodetic one (see Figure 1.2).

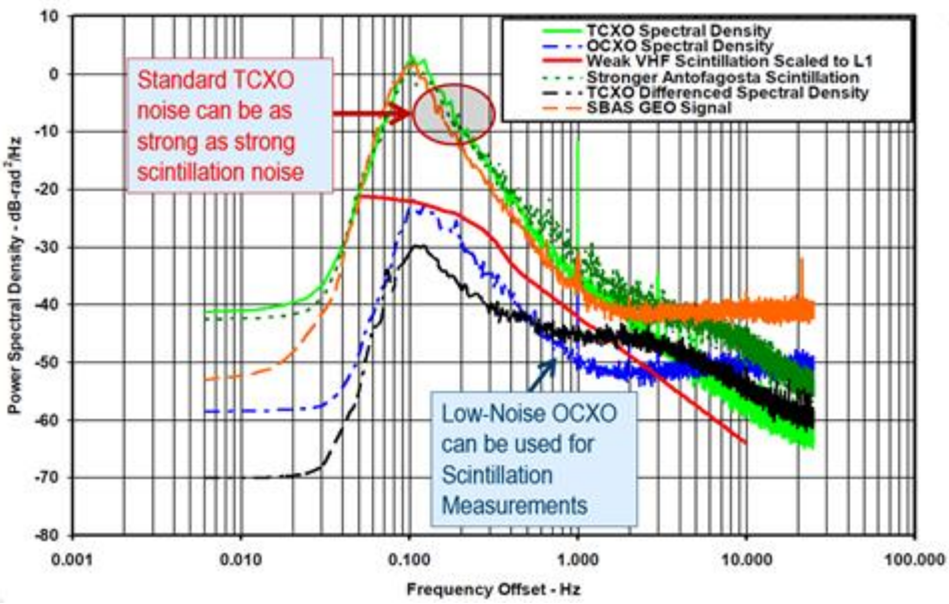

Fig. 1.2 Noise Spectrum Comparison (Andreotti, 2016)

- The tracking loop parameters do influence the DCB estimation. However, in an ISMR, because it has a 'quieter' clock, the PLL bandwidth can be reduced considerably, therefore leading to a better DCB estimation. Lower clock noise also leads to a simplified tracking loop design, which in turn reduces the time bias of the tracking loop (due to a reduced order of the tracking loop implementation). Septentrio design uses a 0.25Hz bandwidth and 2nd order tracking loop, whereas for a geodetic receiver these would be respectively around 0.4Hz (therefore noisier) and 3rd order (therefore 'slow').

Nevertheless, the proposed technique can be applied to any conventional multi-frequency, multi-constellation receiver, as long as its capabilities can be reflected in the GNSS simulator.

With reference to the use of simulators in DCB estimation, it is important to remember that the DCB estimates can vary between simulators, based on their ability to generate high quality signals and on their intrinsic hardware delays. Further complications can arise from the fact that there may exist differences between live and simulated signals depending on correlator spacing and multipath mitigation techniques (Hauschild and Montenbruck, 2016). This would not be a problem in TEC monitoring due to relative time independence of the satellite and receiver DCBs but for other precise operations such as time transfer, this must be given due consideration.

Figure 1.3 shows the DCBs that are part of the reception chain of a GNSS receiver (Sleewaegen, 2015):

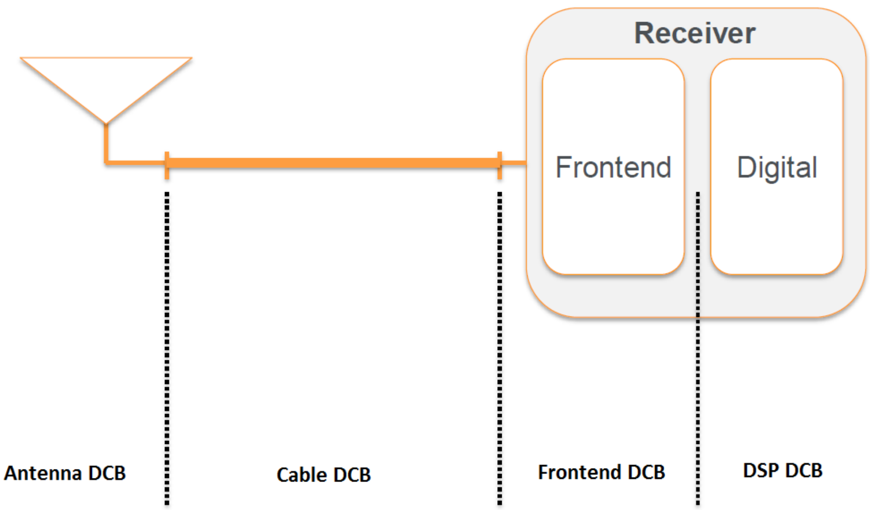

Fig. 1.3 DCBs in the reception chain (Sleewaegen, 2015).

It is to be noted that the receiver DCB itself comprises of a DCB originating because of the delays experienced by the signals within the frontend of the receiver and a DCB that arises because of the delays occurring within the Digital Signal Processing (DSP) unit of the receiver. The good thing is that the DSP DCBs for Septentrio receivers are usually well known by the manufacturer and are compensated for in the firmware. The frontend DCBs in Septentrio receivers are also compensated for the nominal DCB but there may still remain residual DCBs at the level of few nanoseconds (Sleewaegen, 2015). Another key point to remember here is that this compensation process is all vendor specific and the

DCBs (frontend and DSP) are not necessarily compensated all the time (Sleewaegen, 2017). So, pertinent to this research, the residual DCB still exists in the Septentrio receivers and needs to be investigated and analyzed. The antenna and cable DCBs are discussed later in Section 3.6.

1.4 **Outline of the Thesis**

This thesis is composed of eight chapters as shown in Figure 1.4.

Chapter 1	○ Introduction (Motivation and Literature Review)
Chapter 2	○ The Ionosphere and its effects on GNSS
Chapter 3	○ Differential Code Biases in the context of TEC Estimation and PPP Processing
Chapter 4	○ Instrumentation
Chapter 5	○ Methodology
Chapter 6	○ Results and Discussions – Estimated Receiver DCBs using Simulator
Chapter 7	○ Results and Discussions – Estimated Satellite and Receiver DCBs using Real Data
Chapter 8	○ Conclusions and Recommendations for Future Work

Fig. 1.4 Schematic for the thesis outline.

Chapter 1 gives the introduction to the research carried out, specifically covering the two important aspects of motivation and the literature review, that has led to this research.

Chapter 2 gives a short background of the ionosphere and its effects on GNSS signals. It also presents the evolution of ionospheric scintillation and TEC monitor receivers.

Chapter 3 covers the available legacy and modernised GPS and Galileo signals. It also presents the basics of differential code biases from scratch. The possible impact of DCBs in PPP processing is also discussed at the end of this chapter.

Chapters 4 and 5 present the instrumentation and methodology that has been adopted in this research.

A detailed discussion on the estimated receivers DCBs using simulator along with the presentation of results has been carried out in Chapter 6.

A detailed discussion on the estimated satellite and receiver DCBs using real data (based on CODE strategy) along with the presentation of results has been carried out in Chapter 7.

The conclusions drawn and the recommendations for future work are presented in Chapter 8.

Finally, the references and the appendices are presented towards the end of this thesis.

CHAPTER 2

The Ionosphere and its effects on GNSS

2.1 **The Ionosphere**

The Earth's ionosphere is a partially ionized region that envelops the Earth and extends from ~50 km above its surface to ~1000 km. The ionosphere is characterized by the presence of negatively charged free electrons and positively charged atoms and molecules called ions. Collectively, this ionized gaseous medium is referred to as *plasma*. It is formed by *photoionization* which occurs due to the interaction of solar X-rays and extreme ultraviolet (EUV) radiation with the neutral atmospheric constituents. Under the influence of Earth's gravity field, the presence of free electrons and ions in the ionosphere affect the propagation of the electromagnetic (EM) waves like the GNSS signals passing through the ionosphere (Ratcliffe, 1972).

2.1.1 **Vertical Profile of the Ionosphere**

The behaviour of electron density versus altitude is an important parameter for describing different regions/layers of the ionosphere. Figure 2.1 shows the typical daytime structure of the ionosphere.

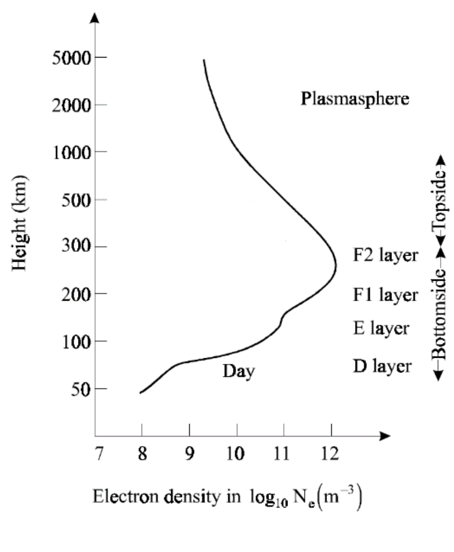

Fig. 2.1 Typical daytime structure of the ionosphere (Davies, 1990)

In order of increasing altitude and increasing electron concentration, the ionosphere can be primarily divided into three regions: D, E and F. Under certain solar-terrestrial conditions, distinct layers may be observed within these regions, such as F1 and F2 within the F region, which are also shown in Figure 2.1. According to Tascione (1988), these regions develop because:

- The solar spectrum deposits its energy at various heights depending on the absorption characteristics of the atmosphere
- The physics of recombination depends on the atmospheric density which changes with height, and
- The composition of the atmosphere changes with height

For general GNSS users, it is important to know that (Klobuchar, 1996):

- The D region (50 - 90 km approximately) has no measurable effect on GNSS frequencies.
- The normal E region (90 – 140 km approximately) also has a negligible effect on GNSS frequencies.
- The normal F1 layer (140 – 210 km approximately) combined with the E region can contribute up to 10% of the effect of the ionosphere on the propagation of GNSS signals.
- The 24-hour present F2 layer (210 – 1000 km approximately) and some part of the F1 layer cause most of the problems for radio wave propagation at GNSS frequencies.

2.1.2 **Total Electron Content**

The ionospheric Total Electron Content or simply TEC is described as the integrated number of free electrons along the path of a trans-ionospheric signal and is perhaps the most important parameter representing the level of ionization in the ionosphere. It is a function of time of day, season, geographic location, solar and geomagnetic activity. It varies mainly with the solar radiation such that it increases as the number of sunspots increases and on a daily average, it starts to increase at sunrise, reaches a maximum around mid-day and decreases at sunset (Leick, 2004). TEC is usually expressed in TEC Units (TECU), where one TECU corresponds to 10^{16} electrons contained in a vertical column of 1-square-metre cross-section and extending along the line of sight of the receiver to the end of the effective ionosphere (see Figure 2.2).

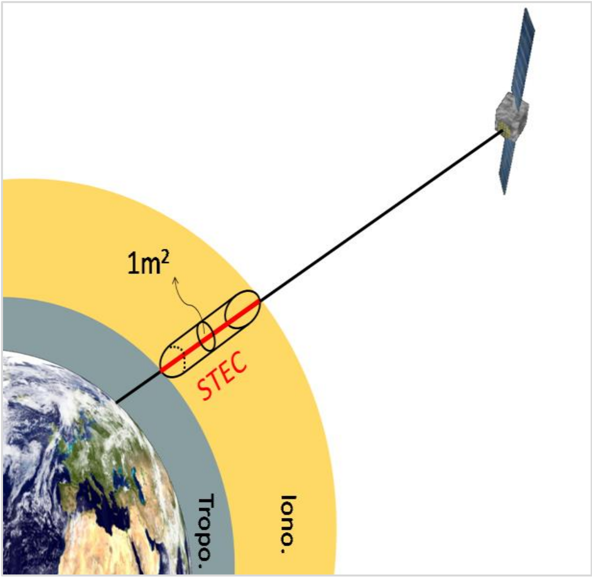

Fig. 2.2 Pictorial representation of STEC or simply TEC (Carrano, 2012)

The line of sight or slant TEC (STEC) is given as:

$$\text{STEC} = \int N_e dl \tag{2.1}$$

where N_e denotes the electron density along the signal path and dl is the length element along the signal path.

2.1.3 **Solar Activity**

Since ionization is primarily driven by X-rays and EUV radiation from the sun, it can be referred to as a function of solar activity. Sunspots are among the most notable phenomena on the solar surface (photosphere) characterizing the solar activity (Schaer, 1999). These are small magnetic regions of varying dimensions that appear as dark areas in the solar disk with magnetic field strengths thousands of times stronger than the Earth's magnetic field (Leick, 2004). The sunspot number has been routinely estimated by Zurich observatory since 1849 (Figure 2.3). According to this, the sunspot activities follow a periodic variation, with a main period of 11 years known as 'Solar Cycle'. This, however, is not always 11 years and can vary from 8 to 14 years.

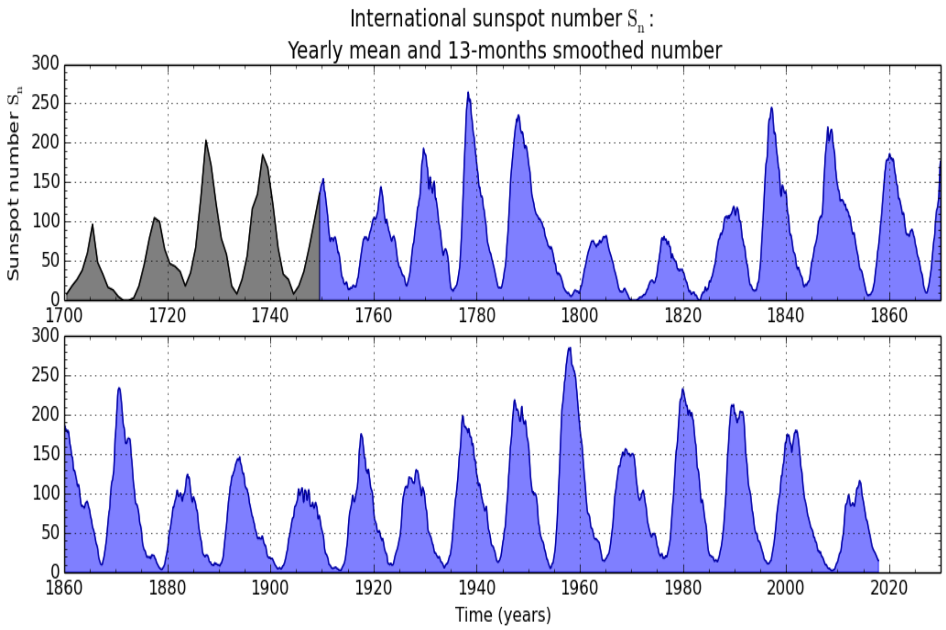

Fig. 2.3 The yearly and monthly sunspot numbers from 1700 up to present (SILSO, 2017)

2.1.4 <u>Geomagnetic Field</u>

The geomagnetic field plays an important role in the formation of the ionosphere. The initial approximation of the Earth's magnetic field is that of a uniformly magnetized sphere with a centre dipole axis which is slightly offset from the Earth's rotational axis. The dipole axis cuts the Earth's surface at the north (*boreal*) and south (*austral*) poles, which are referred to as the *geomagnetic poles*. The *geomagnetic equator* is formed by the intersection of the plane passing through the Earth's center perpendicular to the dipole axis with the Earth's surface. At the geomagnetic poles, the geomagnetic field is vertical to the Earth's surface and at the geomagnetic equator, the geomagnetic field is horizontal to the Earth's surface. The geomagnetic behaviour closer to the surface of the Earth can be well approximated by a simple magnetic dipole but in space, under the interaction with the charged particles of the solar wind, the geomagnetic field gets distorted in such a way that the lines on the side facing the Sun get compressed and the lines on the opposite side get extended in a complicated manner, generating something resembling the tail of a comet. When the geomagnetic field varies smoothly with time, the corresponding days are referred to as geomagnetically *quiet* days (Q-days) and when this is not the case, the corresponding days are referred to as geomagnetically *disturbed* days (D-days). The disturbed days are often associated with increased ionospheric activity.

2.1.5 **Ionospheric Disturbances**

The solar events and the disturbances in the geomagnetic field can give rise to ionospheric disturbances. Under extreme solar conditions (such as a major solar flare or a coronal mass ejection – CME) or intense geomagnetic activity (such as a geomagnetic storm), these ionospheric disturbances can take the shape of ionospheric storms. According to Zolesi and Cander, (2014), the ionospheric disturbances can be:

- Direct effects, caused by rapid changes in solar UV radiation and X-ray illumination of the Earth's ionosphere and atmosphere during solar flares, and
- Indirect effects, caused by complex interactions between the solar wind and the coupled magnetosphere-ionosphere-atmosphere system.

2.1.6 **Geomagnetic Indices:**

The daily variation in the Earth's magnetic field under the solar events can provide a good indication about the ionospheric activity. It can also serve as a convenient proxy for geomagnetic storms. Several geomagnetic indices such as K-index, Kp, Ap, etc. have been used for a number of years to describe the variations in the geomagnetic field.

Kp-index: The 3-hour Kp index is the most widely used planetary index. It is computed as an arithmetic mean of the K-indices which are computed at selected geomagnetic observatories after every 3 hour of the universal time day (UT) by observing the irregular variations in the Cartesian components of the Earth's magnetic field. The 13 geomagnetic observatories lie between 44 degrees and 60 degrees northern or southern geomagnetic latitude. The Kp index is usually expressed in one-third units by adding the signs, –, 0, + to the numbers 0 to 9, thereby providing a 28-step scale. It is extremely useful in evaluating D-days and Q-days (Zolesi and Cander, 2014).

Ap Index: The geomagnetic planetary Ap index for a universal day is computed as the average of eight 3-hour *ap indices.* The ap index or equivalent planetary amplitude is a linear index which is derived from the Kp index and ranges from 0 to 400 (Zolesi and Cander, 2014).

The DCBs are frequently estimated on a daily basis. That is why, the Ap indices have been used in this research to evaluate the DCB estimation in relation to the ionospheric variability.

2.1.7 **Geographic regions of the ionosphere**

Based on the ionospheric behaviour, the Earth can be divided into three distinct regions:

- High latitudes, where the geomagnetic latitude is between 60^{o} to 90^{o} on either side of the geomagnetic equator and are characterised by ionospheric variability due to the connection between the interplanetary plasma and the magnetosphere through the geomagnetic field. The high latitudes region is further sub-divided into *auroral* and *polar cap* regions. Excitation of particles in the neutral atmosphere by energised plasma under the influence of the vertical geomagnetic field produces visible light overhead which is termed as *aurora*. The auroral activity is one of the main characteristics of auroral regions. They often appear as relatively narrow rings situated between geomagnetic latitudes of about 64º to 70º (Davies, 1990). The geographical regions enclosed by the auroral rings are termed as polar caps which are largely affected by solar flares and CMEs, causing D layer electron density enhancements (Komjathy, 1997). Sometimes, small regions known as polar clefts or cusps, are also produced at geomagnetic latitudes from 78º to 80º around local noon time under a direct contact between the magnetosphere and the interplanetary magnetic field. It is characterised by increased electron densities at all altitudes (Davies, 1990).

- Mid latitudes, where the geomagnetic latitude is between 20º to 60º on either side of the geomagnetic equator and are characterized by the least variable and undisturbed ionosphere.
- Low latitudes, where the geomagnetic latitude is between 0º to 20º on either side of the geomagnetic equator. These are characterised with the highest values of the peak-electron density where strong scintillation effects are observed. Scintillation occurrence and its effects on GNSS signals are discussed in Section 2.2. The low latitudes region is further sub-divided into *equatorial* and *equatorial anomaly* regions. At geomagnetic equator, under the influence of the sun and the geomagnetic field, the resulting electric fields cause electrons to rise in altitude and drift away towards higher latitudes along the horizonal lines of the geomagnetic field. This phenomenon is often described as a fountain effect. The corresponding electron density is

minimum near the geomagnetic equator, whereas, it is maximum at geomagnetic latitudes of 15º to 20º on either side of the geomagnetic equator. The higher concentration of electrons in comparison to geomagnetic equator is frequently referred to as the Appleton anomaly or Equatorial Ionization Anomaly - EIA (Zolesi and Cander, 2014).

The geographic extent of each of these regions during an ionospheric quiet day is shown in Figure 2.4.

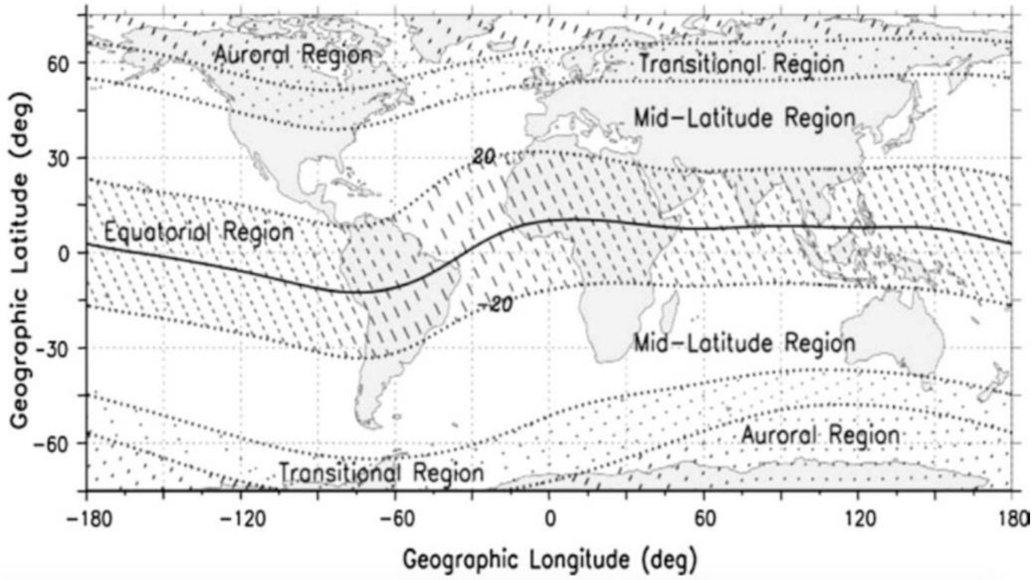

Fig. 2.4 The major geographic regions of the ionosphere (Zolesi and Cander, 2014)

2.1.8 **Refractive Index of the Ionosphere**

Due to interaction between the free electrons in the ionosphere and the geomagnetic field lines, the ionosphere tends to behave as an anisotropic as opposed to an isotropic medium, i.e. it becomes a directionally dependent medium in which the GNSS signals get doubly refracted and decompose into two propagation modes as per their polarization. Each of these modes has a different velocity and hence, it is not an easy task to trace GNSS signals in an anisotropic ionosphere and some approximation has to be made to reduce the computational load.

Since the refractive index depends on the wave normal of a particular signal, therefore, for a given direction of the wave normal, there exist two refractive indices in accordance with the two different polarizations of the wave (Ratcliffe, 1972). In such a case, where the ionospheric refractive index is no longer unity and it offers two different values for the two different modes of propagation, the Appleton-Hartree formula is a good way of describing the refractive index of the ionosphere, n_{ion} (Davies, 1990; Langley, 1996; Hunsucker, 1991):

$$n_{ion}^2 = 1 - \frac{X}{1 - iZ - \frac{Y_T^2}{2(1-X-iZ)} \pm \left[\frac{Y_T^4}{4(1-X-iZ)^2} + Y_L^2\right]^{1/2}} \quad (2.2)$$

with,

$$X = \frac{e^2 N_e}{\epsilon_o m_e \omega^2} = \frac{f_P^2}{f^2} \quad (2.3)$$

$$Y = \frac{eB_o}{m_e \omega} = \frac{e\mu_o H_o}{m_e \omega} = \frac{f_H}{f} \quad (2.4)$$

$$Y_L = Y\cos\theta \quad (2.5)$$

$$Y_T = Y\sin\theta \quad (2.6)$$

$$Z = {}^{v}/_{\omega} \quad (2.7)$$

$$\omega = 2\pi f \quad (2.8)$$

where,

f is the system operating frequency

N_e is the electron density

e is the charge of one electron

ϵ_o is the permittivity of free space

m_e	is the rest mass of an electron
B_o	is the geomagnetic field vector
μ_o	is the permeability in the vacuum
H_o	is the magnetic field strength
θ	is the angle of the ray with respect to the Earth's magnetic field
v	is the electron-neutral collision frequency
f_H	is the electron gyro frequency, $\approx$ 1.5MHz
f_P	is the plasma frequency (i.e. the minimum frequency for the GNSS signals to penetrate an ionospheric layer) and rarely exceeds 20 MHz
Z	is the ratio of the electron neutral frequency v and system operating angular frequency ω

In Equation (2.2), the '$\pm$' denotes the two different modes arising from the double refraction of the GNSS signals in the ionosphere – the ordinary mode (left hand circularly polarized signals denoted by '+' sign) and the extraordinary mode (right hand circularly polarized signals, including GNSS signals, denoted by '–' sign). The ordinary mode '+' is ignored in this research as only the GNSS signals have been considered.

Also, it should be kept in mind that with reference to the radio wave propagation at GNSS frequencies, the terms X, $Y$and Z are all much less than one.

2.1.9 **The Ionospheric Effects on the GNSS Signals**

As explained in Section 2.1.8, the GNSS signals experience double refraction while passing through the anisotropic ionosphere and propagate in two different modes. Each of these modes experiences a different ionospheric effect such that the velocity of one mode (which travels at group or code velocity) decreases while that of the other mode (which travels at phase velocity) increases. The decrease in the group velocity causes the GNSS pseudorange measurements to be greater than the true range, whereas, the increase in the phase velocity causes the GNSS phase measurements to be less than the true range (Bassiri and Hajj, 1993). These ionospheric effects on the group and phase velocity of the GNSS signals are termed as *group delay (*or *absolute range error)* and *phase advance (*or *relative range error)*, respectively (Klobuchar 1996). To account for the phase advance in the case of carrier phase observations, the ionospheric range correction is always *negative,* whereas to account for group delay in the case of pseudorange observations, the ionospheric range correction is always *positive*.

Starting from Appleton-Hartree formula as given in Equation (2.2), Brunner and Gu (1991) derived a relation for determining the phase refractive index, n_{φ}, at an accuracy level of 10^{-9} and it can be expressed as:

$$n_{\varphi} = 1 - \frac{X}{2} - \frac{X^2}{8} - \frac{XY_L}{2} \tag{2.9}$$

where,

X and Y_L are given in Equations (2.3) and (2.5). By using Equations (2.3), (2.4), (2.5) and (2.8), Equation 2.9 can be expanded as:

$$n_{\varphi} = 1 - \frac{1}{2}\left[\frac{e^2 N_e}{4\pi^2 \in_o m_e f^2}\right] - \frac{1}{8}\left[\frac{e^2 N_e}{4\pi^2 \in_o m_e f^2}\right]^2 - \frac{1}{2}\left[\left(\frac{e^2 N_e}{4\pi^2 \in_o m_e f^2} \cdot \frac{e\mu_o H_o cos\theta}{2\pi f m_e}\right)\right]$$

or more compactly as:

$$n_{\varphi} = 1 + \frac{a_1}{f^2} + \frac{a_2}{f^3} + \frac{a_3}{f^4} \tag{2.10}$$

where,

$$a_1 = -\frac{e^2 N_e}{8\pi^2 \in_o m_e} = -\frac{1}{2} f_p^2$$

$$a_2 = \frac{e^2 N_e}{8\pi^2 \in_o m_e} \cdot \frac{e\mu_o H_o cos\theta}{2\pi m_e} = -\frac{1}{2} f_p^2 f_H \; cos\theta$$

$$a_3 = \frac{e^4 N_e^2}{128\pi^4 \in_o^2 m_e^2} = -\frac{1}{8} f_p^4$$

From Equations (2.9) or (2.10), it is to be noted that $n_\varphi < 1$ i.e. for the GNSS signals, the phase velocity becomes greater than the speed of light while passing through the ionosphere and hence referred to as phase advance. A negative ionospheric range correction is therefore used to correct for it.

If n_g represents the group refractive index, then by using the relation $n_g = n_p + f \cdot dn_p/df$ (Leick, 2004), the relation for the group refractive index can be written as:

$$n_g = 1 - \frac{a_1}{f^2} - \frac{2a_2}{f^3} - \frac{3a_3}{f^4} \tag{2.11}$$

From Equations (2.24), it is to be noted that $n_g > 1$ i.e. for the GNSS signals, the group velocity becomes less than the speed of light while passing through the ionosphere and hence will give rise to a group delay. A positive ionospheric range correction is therefore used to correct for it.

The two different refractive indices cause range and phase errors in transmission paths of the GNSS signals as they travel through the ionosphere. The range error in the pseudorange measurements i.e. $(I)_g$ (see Section 3.2), can be determined by (Bassiri and Hajj, 1993):

$$(I)_g = \int (n_g - 1)\, dl \tag{2.12}$$

where dl is the length element along the signal propagation path and subscript 'g' refers to pseudorange measurements being used.

Substituting Equation (2.11) in (2.12) and then integrating:

$$(I)_g = \int \left(-\frac{a_1}{f^2} - \frac{2a_2}{f^3} - \frac{3a_3}{f^4}\right) dl$$

$$= \int \left(\frac{f_p^2}{2f^2} + \frac{f_p^2 f_H\, cos\theta}{f^3} + \frac{3f_p^4}{8f^4}\right) dl$$

$$= \frac{1}{2f^2} \int \frac{e^2 N_e}{4\pi^2 \in_o m_e} dl + \frac{1}{f^3} \int \frac{e^2 N_e}{4\pi^2 \in_o m_e} \cdot \frac{e\mu_o H_o cos\theta}{2\pi m_e} dl$$

$$+ \frac{3}{8f^4} \int \frac{e^4 N_e^2}{16\pi^4 \in_o^2 m_e^2} dl$$

$$= \frac{e^2}{8\pi^2 \in_o m_e f^2} \int N_e dl + \frac{e^3 B_o cos\theta}{8\pi^3 \in_o m_e^2 f^3} \int N_e dl + \frac{3e^4}{128\pi^4 \in_o^2 m_e^2 f^4} \int N_e^2\, dl$$

$$(I)_g = \frac{\kappa}{f^2} \int N_e dl + \frac{\kappa e B_o cos\theta}{\pi m_e f^3} \int N_e dl + \frac{3\kappa^2}{2f^4} \int N_e^2\, dl \qquad (2.13)$$

where,

$$\kappa = e^2/8\pi^2 \in_o m_e = 40.3 \text{ m}^3\text{s}^{-2} \qquad (2.14)$$

In Equation (2.13), the integral $\int N_e dl$ in the first and second terms is $STEC$ as defined in Section 2.1.2. The integral $\int N_e^2 dl$ in the last term is difficult to handle analytically; thus, a shape parameter 'η' is suggested by Hartmann and Leitinger (1984) to facilitate this integration:

$$\eta = \frac{\int N_e^2\, dl}{N_{MAX} \int N_e dl}$$

Equation (2.13) can now be written as:

$$(I)_g = \frac{\kappa}{f^2} STEC + \frac{\kappa e B_o cos\theta}{\pi m_e f^3} STEC + \frac{3\kappa^2}{2f^4} \eta N_{MAX} STEC \qquad (2.15)$$

The first, second and third terms on the RHS of equation 2.15 are the first (Iono1), second (Iono2) and third (Iono3) order ionospheric error terms, respectively. Equation (2.15) can be written more compactly as follows:

$$(I)_g = Iono1 + Iono2 \; + Iono3 \tag{2.16}$$

In the derivation of STEC equations, which are employed in ISMRs for STEC estimation and which will be presented in Section 3.2, only the first order term of Equation (2.16) is used and the higher order terms are neglected.

Similar to the range error in the pseudorange measurements, the range error in the phase measurements can be determined using:

$$(I)_\varphi = \int (n_\varphi - 1\,) dl \tag{2.17}$$

where the subscript 'φ' refers to the carrier phase measurements being used and putting the value of n_φ, the final equation takes the form:

$$(I)_\varphi = -\frac{\kappa}{f^2} STEC - \frac{\kappa e B_o cos\theta}{2\pi m_e f^3} STEC - \frac{\kappa^2}{2f^4} \eta N_{MAX} STEC \tag{2.18}$$

Similar to equation (2.16), equation (2.18) can be written as:

$$(I)_\varphi = -Iono1 - \frac{Iono2}{2} - \frac{Iono3}{3} \tag{2.19}$$

In ISMRs, after ignoring the higher order terms, the above equation is only used to derive the relation for determining the rate of change of TEC.

Neglecting the higher order terms in Equations (2.16) and (2.19), an ionospheric-free observable can also be derived by linearly combining the measurements on two frequencies, which eliminates the first order term, therefore accounting for about 99% of the total ionospheric delay/advance error (Hofmann-Wellenhof et al., 2013). In the case of single frequency GNSS receivers, the users can resort to the ionospheric correction data that is broadcast in the GNSS navigation message or, alternatively, benefit from the SBAS as another source of corrections. The correction data broadcast in the navigation message is based on ionospheric models such as Klobuchar and NeQuick, which are discussed in the next section. For precise GNSS applications requiring an accuracy of centimetre level and below, the higher order ionospheric effects need to be estimated and mitigated.

Considering the GPS L1 signal frequency at low elevation and at extremely high ionospheric activity, say for instance 250 TECU, first-order ionospheric range errors in the phase/code measurements can exceed 100 m. Under similar circumstances, second-order range errors in the phase measurements should be less than 12 cm for GPS L1 frequency, 25 cm for GPS L2 frequency and 29 cm for GPS L5 frequency, whereas, third-order range errors in the phase measurements are generally less than 6 mm for GPS L1 frequency, 16 mm for GPS L2 frequency and 19 mm for GPS L5 frequency (Teunissen and Montenbruck, 2017). The corresponding ionospheric range errors in the pseudoranges need to be multiplied by a factor of 2 for the second-order and by a factor of 3 for the third-order terms. So, for instance, the group delays at GPS L1 should be less than 24 cm and 18 mm for the second- and third-order effects (Teunissen and Montenbruck, 2017).

2.1.10 **Ionospheric Models**

Ionospheric models can be categorized into two major groups (Komjathy, 1997):

- Empirical climatological models: These are based on parameterization of a large amount of ionospheric data collected over a long period of time. Given the long time series of data, it is possible to perform the parameterization in terms of solar activity, seasonal variations, geographical latitude, longitude, and local time variation.

- Theoretical climatological models: In these models, a representative ionosphere or an ionospheric profile is constructed by using a specific set of geophysical conditions. The modelled ionospheric features will have locations, dimensions, similar to those that might be observed on any given day under the specified geophysical conditions

Klobuchar Model: It is an empirical based ionospheric model developed for single frequency GPS users. Eight correction parameters, with an update period of 6 days, are broadcast by each of the GPS satellites in the navigation message. These are used to compute vertical ionospheric delay which is then converted to slant ionospheric delay using an appropriate mapping function. The Klobuchar model is estimated to reduce about 50% RMS ionospheric range error worldwide (Klobuchar, 1987). Because of the relatively low update rate, it is not that effective to account for rapid changes in ionospheric electron content such as in the case of equatorial anomalies.

NeQuick Model: NeQuick is a three-dimensional and time dependent ionospheric electron density model developed for single frequency Galileo users and is based on an empirical climatological representation of the ionosphere. It predicts monthly mean electron density from analytical profiles, depending on sun spot number or solar flux, month, geographic latitude and longitude, height and UT. It approximates the ionosphere as a thin shell, unlike the Klobuchar model. Three correction parameters are broadcast to the users by the Galileo satellites in the navigation message. The study of Memarzadeh (2009) has shown that the NeQuick model can perform better than the Klobuchar model under different ionospheric conditions in the mid-latitude region.

2.2 **Ionospheric Scintillation**

Despite being well researched, the ionospheric scintillation is a hard to predict phenomenon in which the RF signals including GNSS signals, propagating through the ionosphere, experience diffraction which results in rapid fluctuations both in phase and amplitude of the signals (Wanninger, 1993). These fluctuations arise when the signals pass through time-varying small-scale irregularities in the electron density, which can be found within a disturbed ionosphere. The spatial extents of these irregularities can vary from few meters to a few kilometres. Wave front distortion, angle of arrival distortion and scattering are also associated with ionospheric scintillation.

Fluctuations in amplitude and phase of the received signal are more commonly referred to as *amplitude* and *phase* scintillation, respectively.

- Amplitude scintillation, observed as fluctuations and fading on the amplitude i.e. intensity of the received signals, primarily affects the signal-to-noise ratio resulting in something which is commonly referred to as fading in the signal. The S_4 index, which is the normalized standard deviation over 1 minute of detrended high frequency (50 Hz) signal intensity, is used to monitor amplitude scintillation (Van Dierendonck, 1999).
- Phase scintillation causes rapid changes in the phase of the received signal and this may prompt the Doppler shift on the received signal to exceed the bandwidth of the phase tracking loop, i.e. phase locked loop (PLL). It is quantified in terms of the SigmaPhi (σ_φ) index, which is the standard deviation over 1 minute of the detrended high frequency signal phase (Van Dierendonck, 1999).

An example of scintillation event is presented in Figure 2.5.

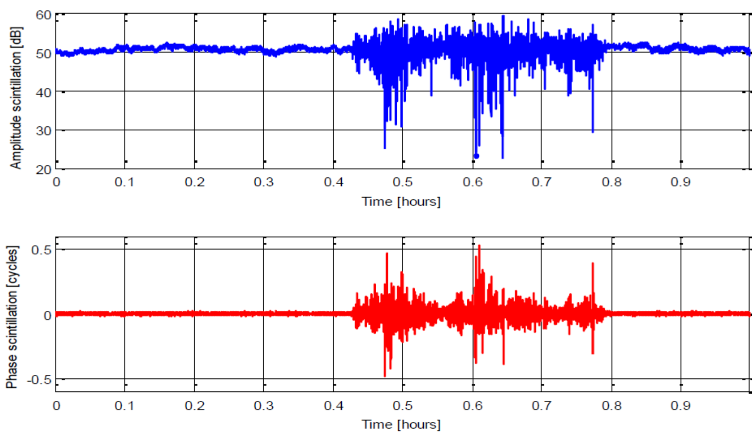

Fig. 2.5 Amplitude and Phase scintillation experienced by L1 C/A signal of GPS PRN (Pseudo Random Noise) 15 as observed at Presidente Prudente station, Brazil, Sep 25, 2011 (Sleewaegen, 2012)

2.2.1 **<u>Global Morphology of Ionospheric Scintillation</u>:**

The phenomenon of scintillation is one of the most predominant elements arising from an active ionosphere. Hence, the scintillation activity can be categorised into the same three regions which have already been described in Section 2.1.7 as part of geographic regions of the ionosphere. Based on actual ground-based scintillation measurements and in situ satellite data, Basu et al. (1988) showed that ionospheric irregularities are concentrated:

- Near the magnetic equator where they are observed in the post sunset period
- In the auroral zone during the night time period and
- In the polar cap region where they are observed at all local times

The global distribution of scintillation fades at L band is shown in Figure 2.6. The scintillation activity also appears to mild down in solar minimum period in comparison to solar maximum.

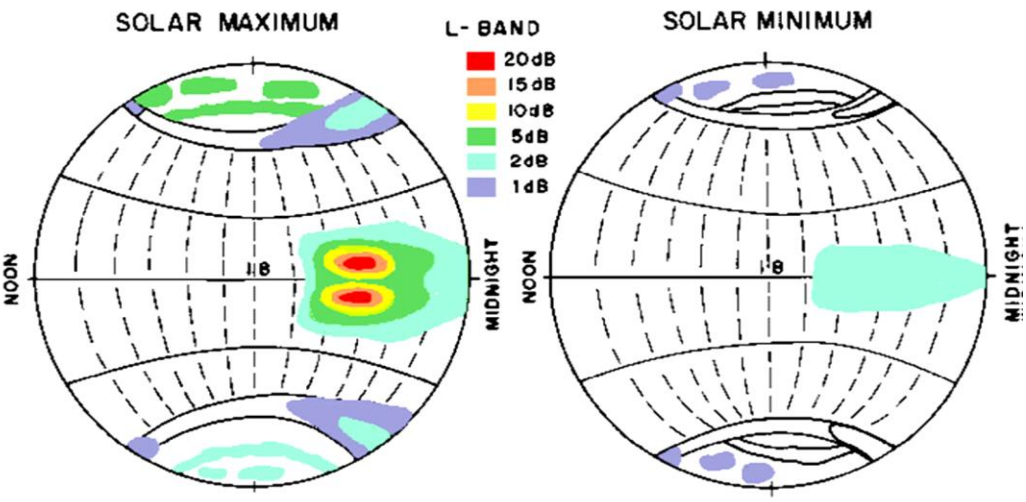

Fig. 2.6 Global variation of scintillation fades during solar maximum and solar minimum (Original black and white image in Basu et al., 1988; coloured image in Wernik et al., 2004)

The characteristics of the observed scintillation effects vary significantly between the low latitude region and the high latitude region. This relates to the fact that the processes which produce scintillation in these two regions are quite different. The auroral and polar cap scintillation is influenced by geomagnetic storms, whereas, the equatorial scintillation appears because of the different ongoing chemical processes within the ionosphere (Davies, 1990).

2.2.2 **Scintillation Effects on GNSS Signals:**

Ionospheric scintillation can result in considerable fading of the GNSS signals. Under such scenario, the poor quality of the received signals leads to the poor performance of the receiver's tracking loops, which in turn degrades the positional accuracy by reducing the precision of both pseudoranges and carrier phases. In the case of the PLL, severe scintillation can result in frequent cycle slips and in worse cases, even the complete loss of satellite lock.

The performance of space geodesy, navigation and communication systems can be seriously compromised under scintillation. According to Sleewaegen (2012), scintillations affecting multiple satellites at the same time can often lead to meter-level PPP errors. Therefore, there is a need to monitor and mitigate scintillation on regular basis. The aforementioned scintillation indices, S_4 and SigmaPhi (σ_φ), are frequently used to study and analyse the level of scintillation. Specialised receivers, i.e. ISMRs with robust tracking have been developed to generate and monitor these indices on a regular basis.

2.3 **Evolution of ISMRs**

For the last thirty years or so, the GNSS receivers are in frequent use to measure ionospheric scintillation effects on the electromagnetic signals passing through the ionosphere. In these receivers, the phase scintillation monitoring is achieved by observing the standard deviation, $\sigma_{\Delta\varphi}$, of detrended carrier phase from the received GNSS signals, whereas, the amplitude scintillation monitoring is done by computing the index S4 which is derived from de-trended signal intensity of the received GNSS signal (Van Dierendonck et al., 1993). It is important to remember that the TEC given by ionospheric scintillation monitors is the STEC and this can be converted to the VTEC using an appropriate mapping function.

According to Sleewaegen (2012), an ISMR is a GNSS receiver that essentially provides the following:

- High-rate unfiltered amplitude measurements
- High-rate carrier phase measurements with low clock jitter
- I and Q correlator values
- Scintillation indices (S4 and $\sigma_{\Delta\varphi}$)
- Enhanced tracking robustness to survive deep fades

So, in terms of manufacturing of ISMRs, the first significant development was made in the early 1990s, when under the Small Business Innovative Research (SBIR) contracts, a GPS based ISMR was developed by GPS Silicon Valley (GSV) in collaboration with NovAtel, Inc. for the US Air Force Research Laboratory (AFRL). It was made by carrying out modifications to a standard NovAtel GPS receiver known as the GPStation. Fitted with a low phase noise OCXO, it was deployed at diverse locations to collect scintillation measurement data from the GPS L1 signal only (Van Dierendonck et al., 1993). Later, the GSV4000 ISMR was developed by GSV that used a slightly better OCXO coupled with a frequency converter card. Around the year 2000, the original scintillation monitors evolved to the GSV4004X series (the GSV4004, GSV4004A and GSV4004B) with a dual frequency receiver capability in its measurement engine. The receiver, the GSV4004, was perhaps the first true commercial GPS based ISMR. It is a hardware/firmware enhanced NovAtel OEM4 dual frequency receiver and has been developed with the same form factor as the original AFRL SBIR version. The GSV4004 entered development during the year 2000 with first deliveries early 2001. In addition to phase and amplitude scintillation monitoring, the TEC in TECU was computed from differences of smoothed GPS L1 and L2 pseudoranges and the rate of TEC was computed from GPS L1 and L2 carrier phases (Van Dierendonck and Hua, 2001). The capability to measure scintillation effects on SBAS signals was added to it in the year 2004 (Van Dierendonck and Arbesser-Rastburg, 2004).

By the end of year 2000, the Space Physics group at Cornell University, Ithace, NewYork, also developed a modified specialized receiver from the commercial GPS development system, the Plessey GPS Builder-2, termed as the Cornell scintillation monitor – SCINTMON (https://gps.ece.cornell.edu/realtime.php). Unlike the GSV series of ISMRs which was primarily designed with a commercial interest, the SCINTMON was designed as an academic tool. As per Beach and Kintner (2000), the main difference between the GPStation and the Cornell scintillation monitor was that the GPStation was normally intended to operate as part of a remote, self-contained scintillation alert system with raw data optionally available for a limited number of channels, whereas, the Cornell scintillation monitor makes detailed recordings of all available data (up to 12 channels) for high time resolution studies of amplitude scintillations only. Also, the GPStation was more expensive because of the higher quality oscillator than the Cornell scintillation monitor.

In the year 2010 and 2011, the more sophisticated ultra-low noise multi-frequency multi-constellation receivers, the Septentrio PolaRxS Pro and the NovAtel GPStation-6, respectively, hit the commercial market as the top of the line ISMRs.

The Septentrio PolaRxS Pro was developed and validated as a modern ISMR, capable of measuring scintillation indices on all civilian signals, in the framework of the CIGALA (Concept for Ionospheric-Scintillation Mitigation for Professional GNSS in

Latin America) project. The CIGALA project, co-funded by the European Commission 7th Framework Program, was coordinated by Septentrio within a consortium of recognised ionosphere physicists and GNSS experts in Europe and Brazil (Bougard et al., 2011). An upgraded version of PolaRxS Pro i.e. PolaRx5S has been launched by Septentrio in the year 2016 to replace the ageing PolaRxS Pro.

More recently, the BG2 GNSS ionospheric monitor was developed by the Institute of Geology and Geophysics, Chinese Academy of Sciences (IGGCAS), for the use in space weather monitoring. It is composed of a NovAtel GPS-703-GGG GNSS receiving antenna and a modified all-in-one GNSS unit which integrates the NovAtel OEM628 receiver board, the interface board, and the embedded industrial computer board inside a mini case (Hu et al., 2017).

CHAPTER 3

DIFFERENTIAL CODE BIASES IN TEC ESTIMATION AND PPP PROCESSING

This chapter starts off by discussing the role of GPS/GLONASS legacy signals and the impact of modernised GNSS signals in TEC estimation. Based on the capability of the NGI's hardware signal simulator, only GPS and Galileo constellations have been considered here. The equation used in ISMRs for TEC estimation has been derived in Section 3.2 using the standard pseudorange observation equation for a GPS L1 and L2 signal pair. This can then be used to obtain modified equations for estimating TEC for any other possible signal pair such as GPS L1/L5, Galileo E1/E5a, etc. For clarification, it should be kept in mind that the term TEC from here after refers to STEC only and unless and until it is clearly stated, it should not be confused with VTEC. Later in the chapter, the M_DCB software (Jin et al., 2012), which has been extensively used in this research, is described in detail. The chapter also highlights the importance of accounting for the antenna and the cable DCBs in the estimation of the DCB of the overall receiver system. The chapter concludes by briefly discussing the impact of DCBs in PPP processing.

3.1 Legacy and Modernised Signals in the context of STEC estimation

For the last two decades or so, the limited number of GPS and GLONASS legacy signals has allowed the generation of a relatively small number of DCB products, such as the GPS based DCB P1/P2 and DCB P1/C1. These have been established as the de-facto standard within the GNSS community for carrying out TEC estimation. However, with the emergence of modernised and newer signals, the users of multi-frequency, multi-constellation observations can get improved TEC estimation using signal frequencies as distinct as possible. Elmas (2013) showed, using the error propagation law, that the GPS L1/L5 combination can yield about 36% better precision than the L1/L2 combination. The L5 signal is also considered to be less noisy with better multipath performance. This means that the current practice of TEC estimation with the L1/L2 pair can well be replaced with the L1/L5 pair in near future. The availability of civil signals can also eliminate the degradation caused by the semi-codeless (or codeless) tracking of the encrypted P2 signal on the L2.

Another important aspect to consider is that most of the modernised GNSS signals offer distinct data-less (or pilot) signal components in parallel to those modulated with navigation data. These pilot signals are considered to facilitate a robust signal tracking under adverse conditions (Montenbrunck et al., 2014), but this can be a nuisance in DCB estimation as these DCBs are not always the same for the pilot and the data signals. So, a receiver generating pilot observables will not 'experience' the same satellite DCB as a receiver tracking the data signal. Receivers tracking a mix of pilot and data signals will experience yet another DCB i.e. the combination of pilot and data. The situation becomes even more complicated when some receivers (Septentrio, NovAtel, Leica) provide observations based on pilot-only tracking technique, whereas others (Javad, Trimble) provide observations based on a combined pilot+data tracking technique (Montenbrunck et al., 2014). This could be a concern when doing global ionospheric analysis as this means that additional DCB terms need to be 'included' depending on the type of receivers being used in the analysis. In practice, the difference between pilot and data is not significant (maybe one or two TECUs), and not all satellites and signals have differences. For example, the Pilot/Data alignment in Galileo satellites seems to be better than on the GPS satellites (Sleewaegen, 2017). In this research, a consistent set of receivers with a similar tracking technique were used while carrying out the global ionospheric analysis while working with the newer GNSS signals. The poor spread of these stations was another problem that was faced while estimating the satellite and receiver DCBs from real data.

3.2 Differential Code Biases (DCBs):

The elementary GNSS observation equations for the code pseudorange observable (P_r^s) and the carrier phase observable (L_r^s) between receiver r and satellite s in units of length can be expressed as follows:

$$P_r^s = \rho_r^s + c(\delta t_r - \delta t^s) + T + I + c(b^s + b^r) + \varepsilon_P \tag{3.1}$$

where,

ρ_r^s	is the true geometric range
δt_r, δt^s	are the receiver and satellite clock offsets, respectively
c	is the speed of light in vacuum
T	is the tropospheric range delay
I	is the ionospheric range delay

b^s, b^r are the satellite and receiver hardware group delay biases, respectively and

ε_P indicates non-modelled residual errors such as those due to multipath or thermal noise for code-delay observations

and

$$L_r^s = \rho_r^s + c(\delta t_r - \delta t^s) + T - I + \lambda N_r^s + \lambda B^s + \lambda B_r + \varepsilon_L \quad (3.2)$$

where,

λ is the carrier wavelength

N_r^s is the carrier phase ambiguity

$\lambda B^s, \lambda B_r$ are the satellite and receiver hardware phase delay biases, respectively and

ε_L indicates non-modelled residuals errors such as those due to multipath or thermal noise for carrier phase observations and can be considered approximately 100 times smaller than ε_P (Ciraolo et al., 2007)

Equations (3.1) and (3.2) are the fundamental GNSS observation equations. In this research, the accurate but ambiguous carrier phase observables are used only to smooth out the absolute but noisy pseudorange measurements. Hence, the carrier phase observation equation is not discussed any further in this thesis.

Taking the example of GPS legacy signals such as L1-C/A (C1), L1-P (P1) and L2-P (P2), equation (2.4) can be written as follows:

$$C_{1,r}^{s} = \rho_r^s + c(\rho t_r - \rho t^s) + T + I_1 + c(b_{C1}^s + b_{C1}^r) + \varepsilon(C_1) \tag{3.3}$$

$$P_{1,r}^{s} = \rho_r^s + c(\delta t_r - \delta t^s) + T + I_1 + c(b_{P1}^s + b_{P1}^r) + \varepsilon(P_1) \tag{3.4}$$

$$P_{2,r}^{s} = \rho_r^s + c(\delta t_r - \delta t^s) + T + I_2 + c(b_{P2}^s + b_{P2}^r) + \varepsilon(P_2) \tag{3.5}$$

where,

$C_{1,r}^{s}$	is the code pseudorange observation equation for C_1 on L1
$P_{1,r}^{s}$	is the code observation equation for P1 on L1
$P_{2,r}^{s}$	is the code observation equation for P2 on L2
I_1	is the delay of the L1 signal due to the ionosphere
I_2	is the delay of the L2 signal due to the ionosphere and is related to I_1 as:

$$I_2 = \frac{{f_{L1}}^2}{{f_{L2}}^2} \times I_1 \tag{3.6}$$

(f_{L1} and f_{L2} refer to the frequencies of GPS L1 and L2 signals, respectively)

From equations (3.3), (3.4) and (3.5), $(b_{C1}^s, b_{C1}^r), (b_{P1}^s, b_{P1}^r)$ and (b_{P2}^s, b_{P2}^r) are the satellite and receiver hardware group delays on C_1, P_1 and P_2 respectively. It is to be noted these biases are not accessible in the absolute sense and the following differences of code biases are commonly considered (Dach et al., 2007):

- $b_{P1} - b_{P2} = b_{P1-P2}$ (3.7)
- $b_{P1} - b_{C1} = b_{P1-C1}$ (3.8)

- $b_{C1} - b_{P2} = b_{C1-P2}$ (3.9)

b_{P1-P2}, b_{P1-C1} and b_{C1-P2} are the so called differential code biases and will be referred to as DCB_{P1-P2}, DCB_{P1-C1} and DCB_{C1-P2} hereafter. Note that these differences of code biases or DCBs for all the other available signals, whether from GPS or any other constellation, can be formed in a similar manner. Here, just for the sake of simplicity and convenience, those are not presented.

In IS-GPS-200H (2014), the correction parameter for the satellite DCB^{s}_{P1-P2} is referred to as the *estimated group delay differential* or T_{GD} and this is provided to the GPS users through the broadcast message. Matsakis (2007) has referred to this as *timing group delay*. The relation between the satellite DCB^{s}_{P1-P2} and T_{GD} is given as:

$$T_{GD} = \frac{1}{1-\gamma} DCB^{s}_{P1-P2} \tag{3.10}$$

where,

$$\gamma = \frac{{f_{L1}}^2}{{f_{L2}}^2} \tag{3.11}$$

Using the definition of the '*Geometry Free or Ionospheric*' linear combination and the code observables from equations (3.3), (3.4) and (3.5), the following observation equations (ignoring the multipath errors and thermal noise) can be formed:

$$P_1 - P_2 = (I_1 - I_2) + c(DCB^{s}_{P1-P2}) + c(DCB^{r}_{P1-P2}) \tag{3.12}$$

$$P_1 - C_1 = c(DCB^{s}_{P1-C1}) + c(DCB^{r}_{P1-C1}) \tag{3.13}$$

$$C_1 - P_2 = (I_1 - I_2) + c(DCB^{s}_{C1-P2}) + c(DCB^{r}_{C1-P2}) \tag{3.14}$$

Here, the superscripts 's' and 'r' are used to categorise the DCBs between satellite and receiver, respectively.

So, for a specific GNSS constellation, the difference of two pseudorange measurements obtained from two different signals equals the sum of the differential ionospheric path delays and the respective satellite and receiver DCBs. If both signals share the same frequency (as in the case of C1 and P1, the combined satellite and receiver DCB equals the average difference of the respective code measurements (Montenbruck et al., 2013).

Using equations (2.14), (2.15), (3.6), (3.10) and (3.11), equation (3.15) can be written as:

$$P_1 - P_2 = \left(1 - \frac{{f_{L1}}^2}{{f_{L2}}^2}\right)\left(\frac{40.3}{f_{L1}^2} STEC\right) + c\left(1 - \frac{{f_{L1}}^2}{{f_{L2}}^2}\right) T_{GD} + c(DCB^r_{P1-P2}) \qquad (3.15)$$

As: 1 TECU = 10^{16} electrons/m^2 and

$$\left(1 - \frac{{f_{L1}}^2}{{f_{L2}}^2}\right) = -0.647$$

So,

$$\boldsymbol{STEC = 9.5238 \times \left[(P_2 - P_1) - \mathrm{c}\big(0.647 T_{GD}\big) + \mathrm{c}(DCB^r_{P1-P2})\right]} \qquad (3.16)$$

Equation (3.16) is the basic equation used in dual frequency receivers (such as the Septentrio PolaRxS Pro) generating C1, P1 and P2 to calculate STEC in TECU. In these receivers, C1 is normally discarded and only P1 and P2 are used in the $STEC$ computation.

Analogously, for the Galileo E1 and E5a code observables, the STEC equation takes the following form:

$$\boldsymbol{TEC = 7.764 \times \left[(E_{5a} - E_1) - c\left(0.7933B_{GD}\right) + c(DCB^{r}_{E1-E5a})\right]} \tag{3.17}$$

where

DCB_{E1-E5a} is the differential code bias between the Galileo E1 and E5a signals and B_{GD} i.e. the *broadcast group delay* is the correction parameter for DCB^{s}_{E1-E5a}.

Considering equations (3.16) and (3.17), if the terms T_{GD} and B_{GD} are 'known' and there are no additional biases, the DCBs alone will be the only contributors to the computation of STEC. So, based on this principle, the research involves using a hardware signal simulator to set T_{GD} and B_{GD} to zero and to determine the physical receiver DCBs by analysing and eliminating the biases coming from the simulator, connecting cable and other miscellaneous hardware.

3.3 Calibrated STEC

Considering equations (3.16) and (3.17), if the satellite and receiver DCB terms are not accounted for, the resulting STEC will be termed as 'Uncalibrated'. This statement is also valid for all the other STEC equations that can be formulated for all those signal pairs that have not been discussed here. Normally, the uncalibrated STEC recorded by the receivers are not used in precise work and people rely on GIMs to derive absolute STEC. Figure 3.1 shows one such instance of uncalibrated STEC for PRN 29 using GPS C1 and P2 signal pair as demonstrated by Shanmugam et al. 2012.

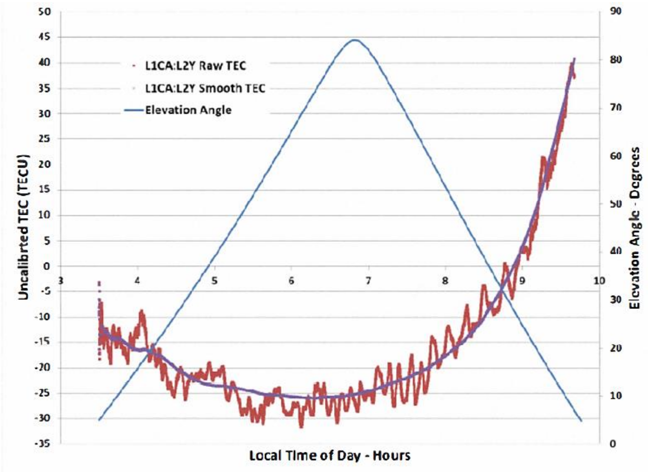

Fig. 3.1 Measured Uncalibrated STEC for PRN 29 between GPS C1 and P2 signal pair (Shanmugam et al., 2012)

If the DCB terms are not ignored and are properly accounted for, then the estimated STEC will be referred to as ‘Calibrated’ STEC. This can be further categorised on the basis of the external constraint that has been used during the global ionospheric analysis to separate the satellite DCBs from the receiver DCBs.

3.4 Code Smoothing

Although the carrier phase measurements are accurate, yet these are ambiguous at the same time and hence, cannot be used for absolute STEC calculations. On the other hand, the pseudorange measurements are noisy but are absolute at the same time and hence, give better approximation of STEC. This can be improved further by adopting the phase smoothed code measurements as suggested by Hatch (1982). The code smoothing using carrier phase, also referred to as carrier phase smoothing, is defined as a process within a GNSS receiver that combines the absolute but noisy code pseudorange measurements with the precise but ambiguous carrier phase measurements to obtain an improved solution, without the noise inherent to the pseudorange tracking (NovAtel, 1997).

A standard definition for smoothed code, known as the Hatch Filter, can take the following form (*where all the terms are in unit of meter*) (Hatch, 1982):

$$(\rho_s)_i = w\rho_i + (1 - w)[(\rho_s)_{i-1} + L_i - L_{i-1}] \tag{3.18}$$

where,

- $(\rho_s)_i$ is the smoothed pseudorange at time step i
- ρ is the raw pseudorange
- L is the carrier phase
- w is the weight factor between '0' and '1' that controls the effective length of the smoothing filter in time. Generally, values of w are much less than 1 (normally 0.01 – 0.001), which involves smoothing times ranging from 100 to 1000 seconds.

It should be noted here that in ISMRs, the weight factor w is controlled by using an appropriate smoothing interval. Note that the code smoothing has nothing to do with the form of the equations (3.16) or (3.17). By applying a suitable smoothing interval, the smoothed pseudoranges are used to compute STEC instead of raw pseudoranges. A conventional smoothing interval of 100 seconds was employed while performing the code smoothing in this research to avoid the problem of code carrier divergence.

3.5 M_DCB Software:

Jin et al. (2012) developed the open source M_DCB software package in MATLAB to estimate the global or regional receivers and GPS satellites DCBs. This is based on the CODE's global ionospheric analysis strategy, in which the VTEC is expressed as a Spherical Harmonics (SH) expansion of degree and order 15. Differences of less than 0.7 ns and an RMS of less than 0.4 ns were found to exist between the products generated by the M_DCB software and those by the IGS ACs (e.g., JPL, CODE and IGS Combined).

The GPS Receiver Independent Exchange Format (RINEX) files (containing P1 and P2 only) and the precise ephemerides (generally the IGS final SP3 products) are the input to the M_DCB software, whereas, the DCB estimates of the satellites and receivers and the VTEC ionospheric coefficients for the defined region are the output. IONEX files are used to compare the estimated DCBs with the IGS generated daily DCB estimates. A flow chart of the software is given in Figure 3.2.

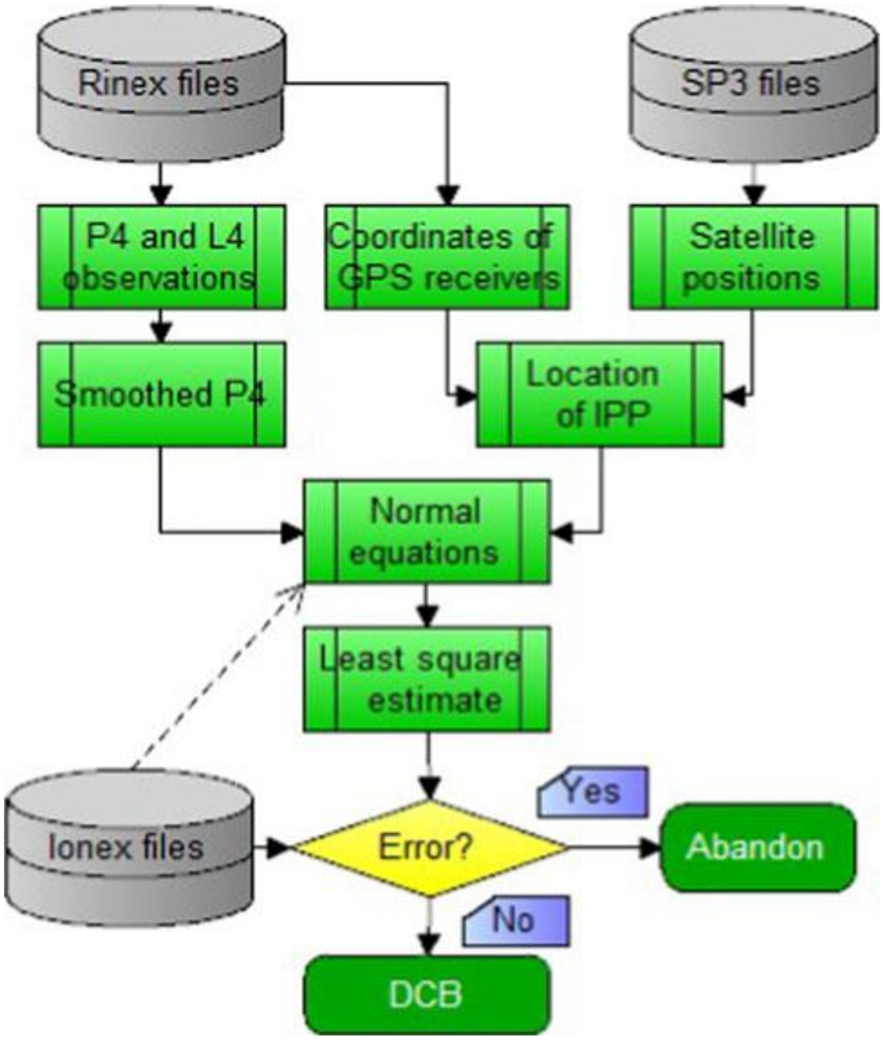

Fig. 3.2 Flowchart of M_DCB Software (Jin et al., 2012)

3.5.1 **CODE Global Ionospheric Analysis**:

Taking into account the translation from line-of-sight STEC into VTEC using a mapping function (MF), equation (3.16) can be written as follows:

$$\text{VTEC} \times \text{MF} = \left[9.5238 \times \left\{(P_2\text{-}P_1) + \text{DCB}^{s}_{P1\text{-}P2} + \text{DCB}_{r,\ P1-P2}\right\}\right] \tag{3.19}$$

In CODE's global ionospheric analysis, a modified single-layer model (MSLM) mapping function approximating the JPL extended slab model is adopted (CODE, 2015). This MSLM can be written as follows:

$$MF = \frac{1}{cos\left(arcsin\left(\frac{R}{R+H} sin(\alpha z)\right)\right)} \tag{3.20}$$

where:

z	is the satellite elevation angle,
R	is the earth's radius (= 6,371 km), and
H	is the altitude of the ionosphere thin shell (= 506.7 km) and
α	= 0.9782.

Following on Schaer (1999), the VTEC can be expressed in terms of a SH expansion as follows:

$$VTEC = \sum_{n=0}^{n_{max}} \sum_{m=0}^{n} \tilde{P}_{nm} (\sin\beta)(a_{nm} cos\ ms + b_{nm} \sin ms) \tag{3.21}$$

where:

β	is the geocentric latitude of the ionosphere pierce point (IPP),
$s = \lambda - \lambda_0$	is the sun-fixed longitude of the IPP,

λ, λ_0 are the longitude of the IPP and the apparent solar time, respectively,

$\tilde{P}_{nm}$ is the normalized Legendre function of degree *n* and order *m* and is equal to $'N_{nm}P_{nm}'$. Here N_{nm} denotes the normalization function and P_{nm} is the classical unnormalized Legendre function, with:

$$N_{nm} = \sqrt{\frac{(n-m)!\,(2n+1)\,(2-\ \delta_{0m})}{(n+m)!}}$$

and δ being the Kronecker delta,

a_{nm}, b_{nm} are the unknown SH coefficients and global or regional ionosphere map parameters, respectively.

The MF and the VTEC in terms of SH expansion, consistent with the IGS CODE analysis centre, have been adopted in the M_DCB software (Jin et al., 2012). Based on equations (3.20) and (3.21), equation (3.19) can be re-written to shape the observable which forms the basis of the design matrix in the LSQ estimation of satellite and receiver DCBs in the M_DCB software:

$$\frac{\sum_{n=0}^{n_{max}}\sum_{m=0}^{n}\tilde{P}_{nm}\,(sin\,\beta)(a_{nm}\,cos\,ms + b_{nm}\,sin\,ms)}{cos\left(arcsin\left(\frac{R}{R+H}sin(\propto z)\right)\right)}$$

$$= \left[9.5238 \times \left\{(\mathrm{P_2\text{-}P_1}) + \mathrm{c}\left(\mathrm{DCB^{r}_{P1\text{-}P2}}\right) + \mathrm{c}\left(\mathrm{DCB^{s}_{P1\text{-}P2}}\right)\right\}\right]$$

OR

$$P2 - P1 = \left[\left\{\frac{\sum_{n=0}^{n_{max}}\sum_{m=0}^{n}\tilde{P}_{nm}(sin\,\beta)(a_{nm}\,cos\,ms+b_{nm}\,sin\,ms)}{9.5238\times cos\left(arcsin\left(\frac{R}{R+H}sin(\propto z)\right)\right)}\right\} - \mathrm{c}(\mathrm{DCB^{r}_{P1-P2}}) - \mathrm{c}(\mathrm{DCB^{s}_{P1-P2}})\right] \qquad (3.22)$$

The above equation is singular and rank deficient. So, an external constraint is needed to separate the satellite DCBs from the receiver DCBs. This can either be in the shape of known receiver DCB of one station or the ZM constraint on the satellite DCBs.

Additionally, code smoothing using the carrier phase can also be applied using a suitable smoothing interval.

3.5.2 **DCB_FIX and DCB_ZM Softwares**:

The original M_DCB software can only handle GPS L1 and L2 signals and works under the external constraint of the zero-mean constraint. As part of this research, this software has been modified to not only handle the newer GPS L5 and Galileo E1 and E5a signals but also to work under either the external constraint of a known receiver DCB or the ZM constraint. The revised version of the M_DCB software that can work with the ZM constraint on the satellites DCBs is referred to as the 'DCB_ZM', whereas the version with the external constraint of known receiver DCB is referred to as the 'DCB_FIX'. Both versions can work with the newer GPS L5 signal and the Galileo E1 and E5a signals. Therefore, in chapter 7, it should be kept in mind that the DCB_ZM labelled results are with reference to the zero-mean condition, whereas, the DCB_FIX labelled results are with reference to known receiver DCB.

3.6 DCB of a Receiver System:

The receiver DCB is often mistaken to be the hardware delays experienced by the GNSS signals while propagating through the RF circuitry within the receiver itself. This is in fact not true because in an open sky situation, similar sort of delays can be experienced by the propagating signals through the antenna, the link cable, the splitter, etc. So, essentially the DCB of the receiver or even satellite should be considered as the cumulative delay contributed by individual components and not as the DCB of the receiver alone. In this research, this has been accounted for by referring to it as the DCB of the entire system. Note that the DCBs estimated by the IGS/MGEX are like so, i.e. they represent the DCB of the entire receiver system.

3.6.1 **Cable DCB:**

The antenna or link cable is commonly considered a non-dispersive medium (Defraigne et al., 2014). However, Dyrud et al. (2008) showed that the variation in L2 – L1 between different lengths of the same cable was found to be within 0.004 meters or approximately 13 ps (picosecond) and this was later validated using the same cable lengths with a network analyser. Working on a similar strategy with lengths of the RG213 coaxial cables ranging from 1 meter to 30 meters, Ammar (2011) also showed variations of up to 35 ps in the estimated DCB between P1 and P2 pseudoranges using simulated data. These small variations in the absolute DCB of the receiver system with varying cable lengths can be explained on the basis of the additional noise that the longer cables introduce in the pseudorange measurements in comparison to the shorter ones. In addition to this, there are several variables in an antenna cable that are frequency dependent, including propagation, skin-effect losses, dielectric losses, etc. Due to the ‘relative’ proximity between GNSS frequencies, those effects are not so visible **in the primary cable type i.e. RG213 coaxial cable that has been used** for data collection in this research. However, this is not true for all possible types of antenna cable, as their dielectric characteristics can vary depending upon the frequency. The reflection of signals within a cable is another phenomenon that can lead to DCBs up to an order of magnitude of few nanoseconds (Sleewaegen, 2015). Hence, to rule out any possible delay occurring within the cable, the cable DCB has been considered at all the stages of this research.

3.6.2 **Antenna DCB**:

The antenna DCB (also referred to as the differential group delay) should be given due importance in the DCB estimation process because in an open sky situation it obviously forms part of the overall DCB of the data recording system comprising the antenna, the cable and the receiver itself. Although antenna's on-site calibration is possible, it can introduce significant difficulty in site deployment. Also, the absolute calibration of the antenna requires a special anechoic chamber and calibrated signals to measure the DCB, which is rather difficult to achieve on site. In this research, the effect of the antenna DCBs has been accounted for by obtaining these from the respective manufacturers. These measured values are made by the manufacturers at a certain temperature. An assumption has been made that the variations in the antenna DCB is small with temperature variations and hence, for the purpose of this research it has been ignored.

3.7 Brief Discussion on the Possible Impact of DCBs on PPP Processing:

According to Zumberge et al. (1997), PPP is a carrier phase based positioning technique which allows achieving centimeter-level accuracy in the static mode to decimeter-level accuracy in the kinematic mode. Unlike Real Time Kinematic (RTK) techniques, there is no need for local reference stations. Teunissen and Montenbruck (2017) have described it as an improved version of the classic pseudorange based positioning, in which broadcast orbits and clocks are replaced with precise orbits and clocks as estimated by different ACs of the IGS/MGEX in a global or regional network solution. The carrier phase ambiguities are also estimated by resolving them to fixed integer values or by keeping them as float. The residual propagation delay due to the troposphere is also estimated after applying an a-priori model. Further modelling is also required to account for other subtle effects such as Earth tides, ocean tide loading, satellite and receiver antenna offsets and carrier phase windup. Accuracy, precision, convergence time (i.e. the time required for a positioning solution to converge below a certain accuracy threshold), availability and integrity are some of the key aspects which are frequently used by researchers to gauge the performance of PPP (Teunissen and Montenbruck, 2017). One of the major drawbacks that limits the applicability of PPP is perhaps the long convergence time that ranges from almost 15 to 60 minutes. The applications of PPP are continuously on the rise and can be found in crustal deformation monitoring, precision agriculture, seafloor mapping, marine construction, airborne mapping, precise orbit determination of low flying satellites, tsunami detection, precise time transfer, and land surveying/construction, just to name a few.

As per Schaer (1999), if the precise clocks are to be used, the basic observables for pseudoranges P1 and P2 as given in Equations (3.4) and (3.5) need to be modified as follows:

$$P_{1,r}^{s} = \rho_r^s + c(\delta t_r - \delta t^{s*}) + T + I_1 + b_{r,P1} - \left[c \times \frac{f_2^2}{f_1^2 - f_2^2} \times \left(DCB_{P1-P2}^{s}\right)\right] \tag{3.23}$$

$$P_{2,r}^{s} = \rho_r^s + c(\delta t_r - \delta t^{s*}) + T + I_2 + b_{r,P2} - \left[c \times \frac{f_1^2}{f_1^2 - f_2^2} \times \left(DCB_{P1-P2}^{s}\right)\right] \tag{3.24}$$

where,

$P_{1,r}^{s}$	is the code observation equation for P1 on L1
$P_{2,r}^{s}$	is the code observation equation for P2 on L2
ρ_r^s	is the true geometric range
δt_r	is the receiver clock offsets
δt^{s*}	is the iono free precise satellite clock offset
c	is the speed of light in vacuum
T	is the tropospheric range delay
I	is the ionospheric range delay
$b_{r,P1}$	is the code delay on P1
$b_{r,P2}$	is the code delay on P2
f_1	is the frequency of GPS L1

f_2 is the frequency of GPS L2

DCB^{s}_{P1-P2} is the satellite DCB between P1 and P2 signal pair.

This is because the precise clocks are in fact estimated by using an ionospheric free linear combination of satellite DCBs between the P1 and P2 signal pair and to account for this, the corresponding DCB terms need to be added to the basic pseudorange observation equations (see Appendix B for the full derivation). The purpose of presenting equations (3.23) and (3.24) is to highlight the important aspect that the DCB corrections can be of two types. In the case of a different receiver type (such as C1/P2 receiver), a DCB correction in the form of P1-C1 is applied to the C1 pseudoranges to make them compatible and consistent with the precise clocks that are originally derived from the P1/P2 signal pair only. This is referred to as '*Type I*' DCB correction in this research. The other DCB correction (i.e. '*Type II*') is needed once uncombined raw GNSS observations are to be used in PPP. This is to account for the additional DCB terms appearing in equations (3.23) and (3.24). However, an important point to highlight is the fact that the IF combination is frequently employed while carrying out the PPP processing, in which case, the additional DCB terms cancel out and the second type of DCB correction is not needed. This second type of DCB correction is analogous to the T_{GD}/B_{GD} correction that the users need to apply while working with only single frequency uncombined observables and broadcast clocks. As a consequence, until and unless, uncombined raw GNSS observations are used, the effect of the above mentioned additional DCB terms won't appear in the PPP solution. These additional DCBs are the ones that have been used to compute the precise clocks in the first place and for the sake of compatibility and consistency, they need to originate from the AC whose precise products have been used in the PPP solution.

Basile et al. (2017) demonstrated that the convergence time in PPP would reduce if less noisy pseudoranges are used. One of the ways to do this is to avoid using the IF combination which despite the fact that it is well accepted to mitigate the first order ionospheric effects but at the same time, it limits the potential performance of PPP by amplifying the noise in the measurements by up to 3 times. With regards to the above discussion, only the PPP approach based on uncombined raw GNSS observations has been followed in this research.

CHAPTER 4

INSTRUMENTATION

This chapter presents and describes in detail the instrumentation that has been used in this PhD research work. The primary instrumentation comprises of hardware signal simulators and multi-frequency, multi-constellation geodetic/scintillation receivers. The supporting equipment such as antennas and cables used in this research has been tabulated at the end of this chapter.

4.1 Spirent GSS8000 Multi-GNSS Constellation Simulator:

A RF Constellation Simulator reproduces the environment of a GNSS receiver on a dynamic platform by modelling vehicle and satellite motion, signal characteristics, atmospheric and other effects, causing the receiver to actually navigate according to the parameters of the test scenario. It allows the users to emulate multi GNSS signals with relatively high accuracy, repeatability, controllability and reliability. These Multi-GNSS Constellation Simulators have been specifically developed to meet the ever-growing demands of all the designers, developers, integrators and testers of GNSS receivers or systems (Spirent, 2009a).

The Spirent GSS8000 system consists of two major components, i.e. the RF signal generator and the scenario definition and simulation control software SimGEN™ on the host PC as shown in Figure 4.1.

At the NGI, the available RF signal generator part further comprises of two different signal generator chassis. One is dedicated for GPS signals generation and the other is dedicated for Galileo signals generation. The signals from both the GPS and the Galileo generators can be combined into a single RF output by using a Spirent Multi-box Combiner Unit (MCU). In this research, the combined GPS and Galileo simulated signals through the MCU were not collected to eliminate the potential delay coming out from the MCU except the calibration case of the Spirent GSS9000 simulator where it was unavoidable.

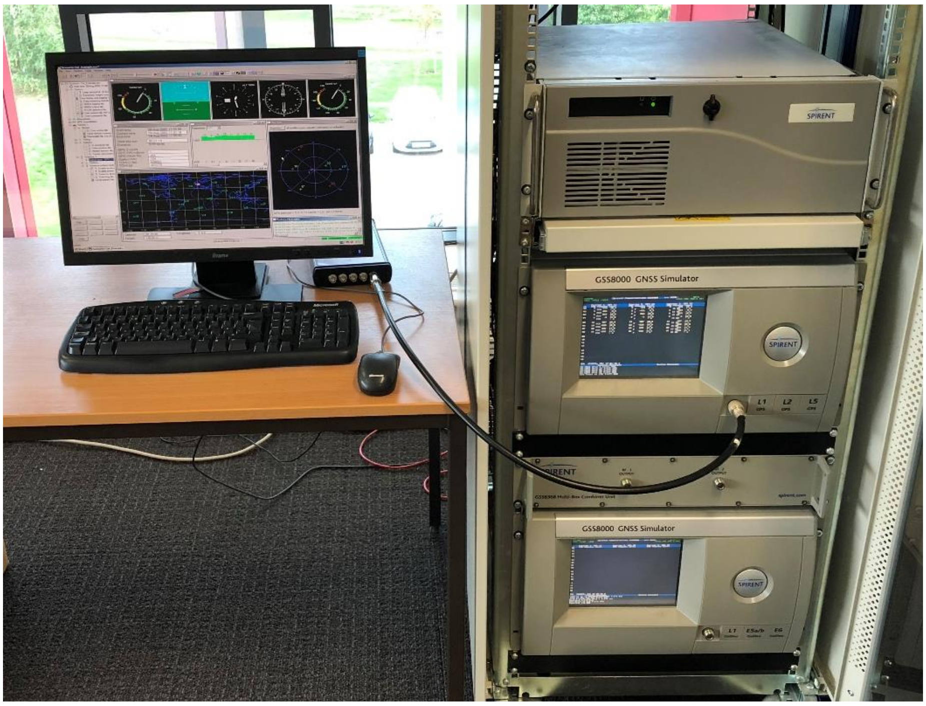

Fig. 4.1 Spirent GSS8000 Signal Generator with PC Controller

4.1.1 **<u>Signal generator</u>:**

The simulated signals are generated within the signal generator and are then transferred to a test receiver either through the RF output port provided at the front of the individual signal generator or through the one available at the front of the MCU. In terms of hardware, the main feature of the Spirent GSS8000 signal generator (whether GPS or Galileo) is that it consists of 3 banks comprising of 4 channel cards each. Each channel card in turn has 4 channels. So, each bank has in fact 16 channels in total and is dedicated for emulating one carrier frequency only (Refer to Figure 6.2 for clarification). For a combination of three GPS signals i.e. L1, L2 and L5, each simulator bank will generate one signal frequency. By default, the simulator automatically allocates the channels to different visible satellites in ascending order of the elevation angles. It is important to clarify here that once a satellite transmitting GPS L1, L2 and L5 signals is assigned to one particular 'Channel' using the SimGEN™ software, then this essentially means that a particular channel on each of the three banks is used for simulating that satellite's L1, L2 and L5 signals. So, the signals coming from that satellite and associated with one channel, are in fact a combination of three hardware outputs (or channels) on three different banks of the signal generator.

4.1.2 **SimGEN™:**

SimGEN™ is Spirent's GNSS simulator software suite, which runs on a Windows PC and helps the user to specify and develop scenarios to run various simulations according to their own specific requirements. A screenshot of the SimGEN™ scenario definition and simulation control software is shown in Figure 4.2.

4.1.3 **Modes of Operation:**

The Spirent GSS8000 hardware simulator can be run in two modes of operation: 'Modelled' signal strength mode and 'Fixed' signal strength mode. In the 'Modelled' mode of operation, the satellite signal levels are modified as a function of the satellite to receiver antenna distance in proportion to $1/(\text{distance})^2$, whereas in the 'Fixed' mode of operation, the satellite signal levels are not at all modified as a function of satellite to receiver antenna distance (Spirent, 2009b).

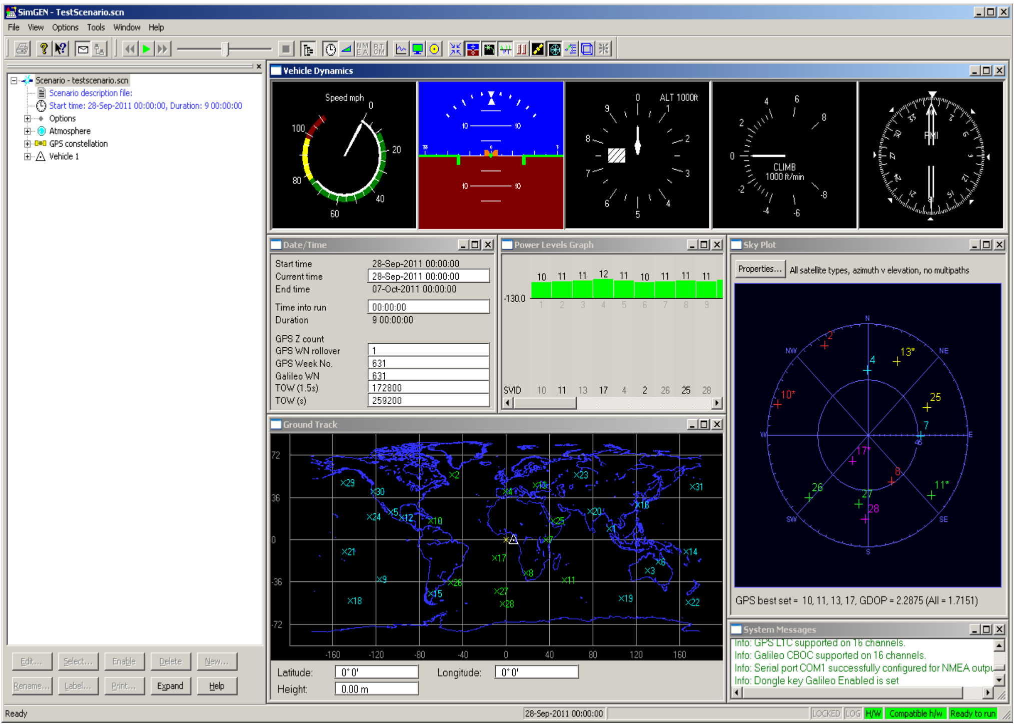

Fig. 4.2 screenshot of the SimGEN^{TM} software Scenario Definition and Simulation Control interface

4.1.4 __Cooling Fan__:

The cooling fan is provided to blow air into the signal generator, which vents through a side panel. Spirent strongly recommends not to cover or restrict the inlet or outlets as overheating may result in severe and permanent damage. They also recommend to periodically remove the filter fitted to the inlet and wash it in clean water (Spirent, 2009a).

4.2 __Spirent GSS9000 Multi GNSS Constellation Simulator__:

The Spirent GSS9000, shown in Figure 4.3, is a hardware signal simulator that can also be used to emulate multi-frequency multi-constellation GNSS signals. It is an upgraded and improved version of the Spirent GSS8000 simulator. It consists of a Signal Generator Chassis (SGC) and a dedicated C50r Host Unit running Spirent's SimGEN^{TM} software. The SimGEN^{TM} has already been introduced in Section 4.1.2.

Unlike multiple signal generators of GSS8000, the SGC consists of one or more RF channel banks and each one of them, at any one time, is capable of supporting any particular GNSS constellation and frequency. So, in simple words, the same generator can be used to generate multi frequency signals from a single constellation or multi frequency signals from multi constellations (Spirent, 2017b).

Fig. 4.3 Spirent GSS9000 System (Spirent, 2017b)

4.2.1 **<u>Calibration Procedure</u>:**

The signal delay calibration is an important aspect of any hardware signal simulator and as per the manufacturer, a periodic calibration is highly recommended to ensure high quality performance, specified accuracy and reliability.

For all the Spirent simulators, the in-house calibration is done at the manufacturing facility before supply to the customers. Before GSS9000, the in-house calibration involves measuring manually the 1PPS (Pulse Per Second) to RF delay of all the available RF channel banks using external hardware such as oscilloscope and/or network analyser. Once measured, these are then mitigated in the firmware. In recent Spirent simulators such as GSS9000, the 1PPS to RF delay is manually measured for only one of the available RF channel banks. The Auto Calibration Utility (ACU) is later used to calibrate the delays of all the remaining RF channel banks relative to first manual delay measurements to within ~100 ps of each other. Thus, the overall alignment of the signals at the RF output depends mainly on the accuracy of the initial manual delay measurements. The absence of the ACU hardware facility in GSS8000 is another key difference between the GSS9000 and GSS8000 simulators and that is the reason, this calibration procedure was not described in the previous section. Having said that, the rest of the calibration procedure excluding the ACU part is equally valid to calibrate the GSS8000 simulator but instead of just one RF channel bank, it needs to be done for all the RF channel banks.

The calibration procedure for the manual delay measurements for the first RF channel bank is as follows (Spirent, 2017a):

- A simple scenario is run, with a single GEO satellite located above the receiver producing a single signal, say for instance, GPS L1.

- At the same time, the 1PPS is also fed into the oscilloscope which is then used to measure the delay between the simulator's 1PPS output and a code transition in the GNSS signal. In Figure 4.4, the yellow trace is the simulator's 1PPS signal and the blue trace is the L1 C/A signal. The two cursors 'a' and 'b' show where the delay measurement is taken. It can be difficult to determine exactly where the code transition occurs, so repeat-and-average will be useful. Additionally, choosing a suitable PRN code can help determine the point, where there will be a code transition aligned with the 1PPS and it is strongly recommended to choose a PRN that switches value at this transition.
- By repeating the same procedure with other GNSS signals and comparing it with the individual delay measurement of other signal, the DCB between all the available signal pairs can be estimated.
- Rather than using the low power front RF port of the simulator, the signals from the rear high-power calibration output with additional amplification are fed into an oscilloscope. This amplification will have a frequency-dependent delay of ~1 ns across the frequency band in the setup but this can ideally be measured through the Network Analyser and calibrated in the final calculations.

According to Spirent, they calibrate each RF path in the simulator (e.g. L1, L2 and L5) at the time of manufacturing so that the 1PPS–to–RF difference is better than 500 ps.

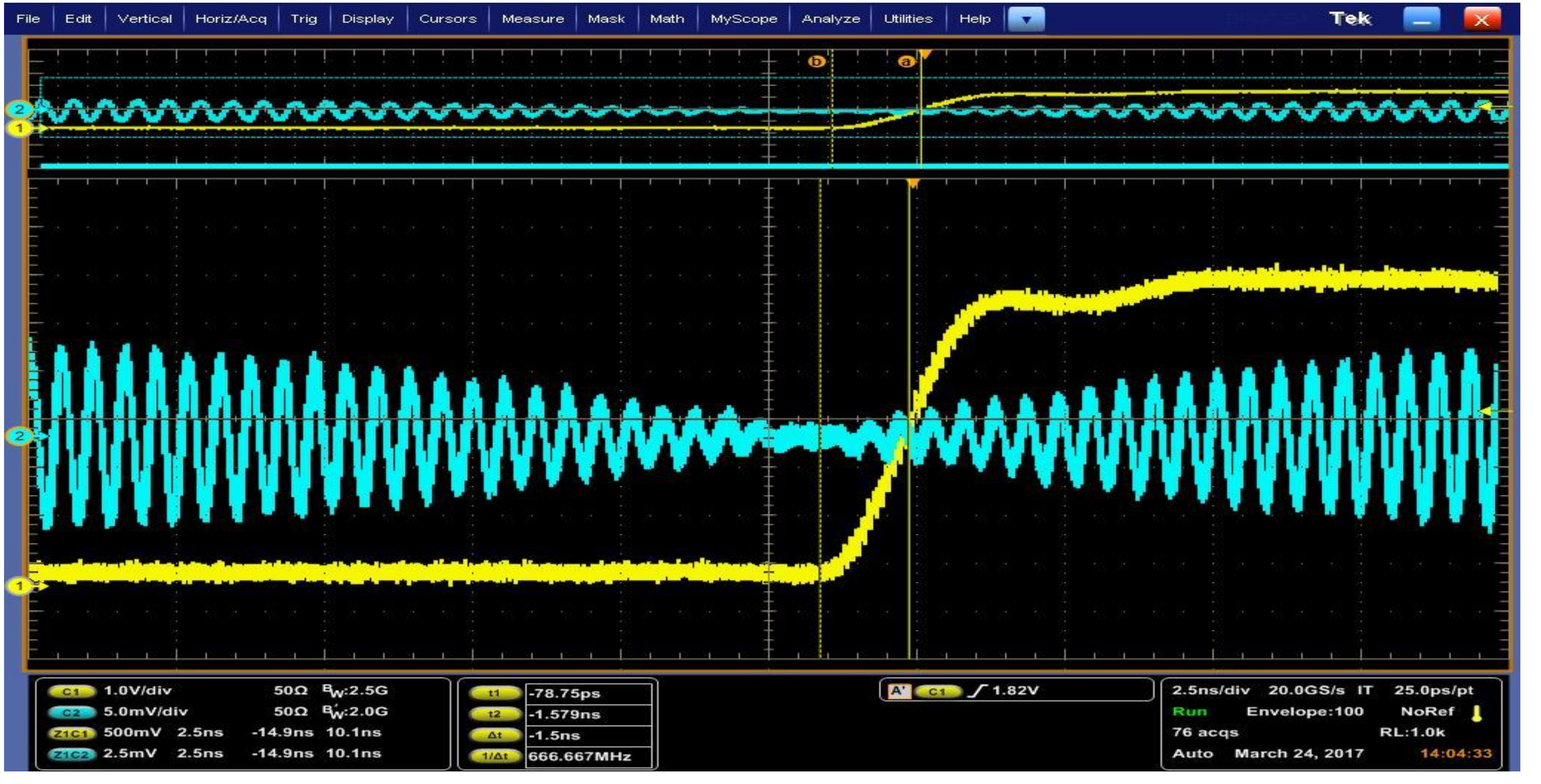

Fig. 4.4 Screenshot of an oscilloscope showing the delay measurement which is taken between point 'a' of 1 PPS and point 'b' of the code transition on the L1 C/A signal (Spirent, 2017a).

Before going any further, there is a need to revisit some key aspects that can still add uncertainties to the calibration procedure. These are as follows:

- The ability to exactly locate the code transition point – From the author's personal experience, it is generally done by trial and error. To mitigate its effect, a repeat and measure rule is generally followed but this might contribute to some uncertainty in the overall procedure.
- The use of the rear high-power port of the simulator rather than the front low-power port – The front RF ports on the simulator are frequently used by the GNSS users for collecting simulated signals. According to Spirent, the individual RF delays to the front port are measured and minimised through the firmware at the time of manufacture. But if these delays are ignored and not minimised while the simulator is in use, this can bring in some additional uncertainty with reference to hardware delays even if the simulator is calibrated using the rear port.

4.3 Septentrio PolaRxS Pro Receiver:

The Septentrio PolaRxS Pro receiver, shown in Figure 4.5, is a multi-frequency multi-constellation ISMR with a state-of-the-art triple frequency engine and an ultra-low noise OCXO. It has been specifically designed to perform ionospheric monitoring and can therefore also be used in support of space weather applications (Septentrio, 2015a).

Fig. 4.5 Septentrio PolaRxS Pro Receiver (Sleewaegen, 2012)

4.3.1. **RxControl:**

The RxControl program is an intuitive Graphical User Interface (GUI) which is used to control the operations of the PolaRxS Pro receiver, to perform data logging and to monitor the navigation solution (Septentrio, 2015b).

4.3.2. **Measurement of STEC:**

In the PolaRxS Pro, the STEC is computed from GPS and Galileo signals using equations 3.16 and 3.17, respectively, and these can be directly obtained from the ISMR log files (Septentrio, 2015a). In the case of GPS, STEC is based on P1 and P2 pseudoranges, whereas in the case of Galileo, on E1 and E5a pseudoranges. These can also be compensated by default for their respective group delay differential, but these can be left as uncompensated through the RxControl software (Septentrio, 2015a). Another way of computing STEC through this receiver is to use the raw pseudoranges as recorded in the RINEX observation files using again equations 3.16 and 3.17. The latter approach is useful in that the STEC information can be computed from all the available/simulated signal pairs.

4.3.3 **STEC Calibration**:

In the Septentrio PolaRxS Pro receiver, there is a provision for compensating the satellite and receiver DCBs during the data collection. This is done for the satellite DCBs by using the broadcast group delays, whereas in the case of the receiver DCB, this is done by comparing the measured TEC values (after correction for the satellite DCBs) with reference TEC values. The TEC reference can either be extracted from the SBAS ionospheric corrections, or estimated using the Klobuchar ionospheric model, in line with the research work carried out by Van Dierendonck (2001) and Dodson et al. (2001). The bias between the measured and the reference TEC values is averaged over several passes for each satellite individually, or for a whole constellation in case satellite biases are corrected. A fixed elevation mask of 15 degrees is applied (Septentrio, 2015a). This approach is however inadequate because of the limited accuracy of the ionospheric corrections used.

4.3.4 **Code smoothing filter**:

The standard Hatch Filter, as defined in Section 3.3, is used to smooth code measurements using the carrier phase (Ammar, 2011). By default, the PolaRxS Pro receiver does not apply any code smoothing. The RxControl is used to apply any suitable smoothing interval ranging from 1 to 1000 seconds on any of the tracked carrier signals.

4.4 **Javad Triumph–I Receiver**:

The Javad Triumph–I, shown in Figure 4.6, is a multi-frequency, multi-constellation geodetic grade receiver that has been specifically designed to carry out precise GNSS surveys. It does not output any ionospheric related information such as TEC and scintillation parameters as in the case of ISMRs.

Fig. 4.6 Javad Triumph–I Receiver (Geo-matching, 2017)

4.4.1 **<u>NetView</u>:**

NetView is a Windows based GUI, which is used to control the operations of all navigation equipment developed and manufactured by Javad.

4.4.2 **<u>Measurement of STEC</u>:**

In the Javad Triumph–I receiver, STEC cannot be computed by default using the NetView software. However, this can be done for both GPS and Galileo signals using equations 3.16 and 3.17, respectively, from the pseudoranges recorded in the RINEX observation files. This is in line with the approach described in Section 4.3.2.

4.4.3 **<u>Code smoothing filter</u>:**

There is no information available for Javad receivers on the filter type that is used to smooth code measurements using carrier phases. However, by default, the Javad Triumph–I receiver does apply a smoothing of 100 seconds on all the raw observables.

4.5 Miscellaneous Equipment:

A variety of equipment such as antennas and cables was used in the estimation of the receiver/satellite DCBs using simulated and open sky signals. Different lengths of the cables were also involved to assess the impact of varying cable lengths on DCB estimation. The details of these antennas and cables are presented in Table 4.1 and Table 4.2, respectively.

Table 4.1 Description of antennas used in DCB estimation

<table>
<tr><th>Antenna</th><th>Description</th></tr>
<tr><td>Leica AR10</td><td>It is a high performance GNSS reference station antenna. It is a multi-frequency, multi constellation antenna and can track almost all the legacy and modernised signals (Figure 4.7).


Fig. 4.7 Leica AR10 multi-purpose GNSS antenna with integrated radome (SCCS, 2018)</td></tr>
<tr><td>NovAtel GPS 702GG</td><td>It is an L1/L2 GNSS antenna, offering combined GPS + GLONASS signal reception (Figure 4.8).</td></tr>
</table>

	 **Fig. 4.8** GPS 702 GG Dual Frequency GPS + GLONASS Pinwheel® Antenna (NovAtel, 2018a)
NovAtel GPS 703GGG	It is a triple frequency GNSS antenna. It receives L1, L2 and L5 GNSS frequencies and offers combined GPS + GLONASS + Galileo + Beidou signal reception (Figure 4.9).  **Fig. 4.9** GPS 703 GGG Triple Frequency Pinwheel® Antenna (NovAtel, 2018b)
Septentrio PolaNT Choke Ring	It is a high precision multi-frequency antenna for GNSS reference stations. It also receives L1, L2 and L5 GNSS frequencies and offers combined GPS + GLONASS + Galileo signal reception (Figure 4.10).

	 **Fig. 4.10** Septentrio PolaNt Choke Ring B3/E6 Antenna (Septentrio, 2018b)

Table 4.2 Description of cables used in DCB estimation

Cable	Description
RG213	It is a high quality coaxial cable. Lengths varying from 1 m to 30 m are available at NGI's GNSS Lab.
RG58AU	It is a relatively lower quality coaxial cable in comparison to RG213 cable. The length available at NGI is of 3 meter and has been supplied by Javad with its Triumph-I receiver.
Huber-Suhner	It is also a coaxial cable. A length of 1 m is available in NGI's GNSS Lab.
Note: RF cables, carrying high frequency (HF) band signals or above, are mostly coaxial cables. A coaxial cable is an electrical cable in which a core wire is surrounded by a non-conductive material, which is referred to as dielectric or insulation. The dielectric is then surrounded by an	

encompassing shielding which is often made of braided wires. The purpose of dielectric is to keep apart the core and the shielding. A final outer jacket of some PVC material is provided to protect all the inner components. The inner conductor carries the RF signal and the outer shield keeps the RF signal from radiating to the atmosphere and also stops the outside signals from interfering with the signal carried by the core. The larger the central conductor, the better the signal will flow through it (Zennaro and Fonda, 2004). Figure 4.11 shows a typical cross-section of a coaxial RF cable.

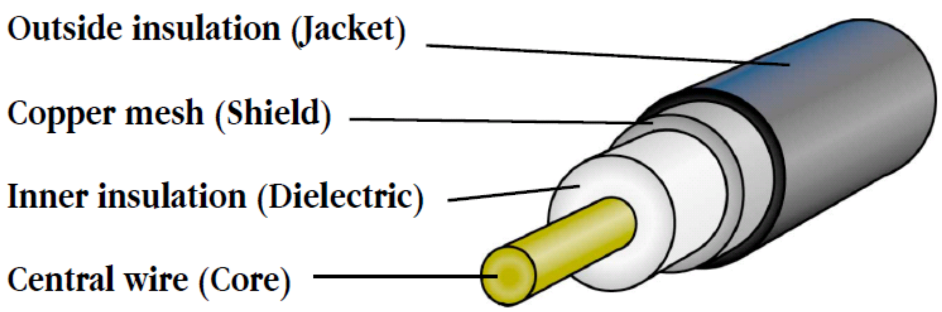

Fig. 4.11 A typical cross-section of an RF coaxial cable (Zennaro and Fonda, 2004)

CHAPTER 5

METHODOLOGY

Before describing the methodology followed, it is important to remember that the receiver DCB estimation carried out in this research was mostly based on the NGI's Spirent GSS8000 hardware signal simulator and some of the limitations of using this simulator were as follows:

- It comprises of only GPS and Galileo generators. So, it was not possible to incorporate other constellations in this research.
- It came calibrated at the time of its purchase in the year 2009 but since then, it has never been recalibrated.
- Based on the calibration procedure as stated in Section 4.2.1, the 1PPS-to-RF values measured for the NGI's GSS8000 simulator at the time of purchase are as follows (Spirent, 2017):
  - ✓ L1: -200 ps
  - ✓ L2: +200 ps
  - ✓ L5: -200 ps
  - ✓ E1: -50 ps
  - ✓ E5: -50 ps

  Here, positive values mean that the code transition occurs *after* the 1PPS rising edge. Negative values imply that the code transition occurs *before* the rising edge of the 1PPS. Because of the time constraint, these values were measured in dual-box configuration. That is, they include the delays due to the MCU. Also, as these values are only for one code so any difference between, for example, L1 C/A (or C1) and L1 P-code (or P1) is not accounted for. However, as these different codes are produced on the same Field-Programmable Gate Array (FPGA), the corresponding biases are expected to be negligible. Using the above 1PPS-to-RF values, Table 5.1 gives the DCB estimates of the NGI's Spirent GSS8000 simulator.

Table 5.1 DCB estimates of the NGI's GSS8000 hardware signal simulator based on original calibration at the time of purchase

Signal Combination	Mean DCB (ns)	Standard Deviation (ns)	Remarks
L1 – L2	+ 0.40	± 0.2	*The standard deviation of 0.2ns is an assumed value as specified by the manufacturer.*
L1 – L5	0	± 0.2	
L2 – L5	+ 0.40	± 0.2	
E1 – E5	0	± 0.2	

As these calibration values are quite old, they have not been used directly in this research.

To overcome the calibration issue and to validate the estimation results, a Spirent GSS9000 constellation simulator was involved in the research at two different occasions. Once it was loaned to NGI by Spirent for undertaking some miscellaneous research work and the other time when it was used during an agreed short trip to the Spirent facility in Paignton, UK. Note that even during the loan time, the GSS9000 simulator was uncalibrated and also had some clock degradation issues that were later acknowledged by the manufacturer, whereas in the second instance, it was calibrated at the start of the short trip before running any simulations and was without any clock degradation issues. The general methodology carried out to estimate the receiver DCBs using simulation with both uncalibrated and calibrated simulators is described in Section 5.1 and the methodology that is followed to estimate the satellite and receiver DCBs using the 'known' receiver DCB in a terrestrial global network is explained in Section 5.2.

5.1 Receiver DCB Estimation using Simulation:

The approach that was followed to estimate the receiver DCB was to use the available hardware signal simulator i.e. GSS8000 or GSS9000 to generate all possible GNSS signals without ionospheric and tropospheric delays, as well as eliminating simulated satellite signal delays such as T_{GD} and B_{GD} by setting them to 0. The Septentrio PolaRxS Pro (SEPT) receiver was set to track these simulated signals under default tracking loop parameters with no multipath mitigation as presented in Table 1. Initially, the STEC computed by the receiver on the basis of P1 and P2 pseudoranges and as given in the ISMR logs was taken as the representation of the DCB estimate of the receiver. Later on, to include the newer GPS L5 and the Galileo signals and to maintain consistent approach between different signal combinations, the STEC was always computed from the recorded RINEX observations on the basis of equation (3.16) for GPS and (3.17) for Galileo depending upon the signal combination and using all the available satellites. In either case, the mean of the computed STEC for all the satellites essentially gave the DCB of the receiver for a particular signal combination. The same methodology was followed for the DCB estimation of SEP2 and JAVD receivers and the different tracking parameters applied to these receivers are also presented in Table 5.2.

Table 5.2 Default tracking parameters (unless stated otherwise) that are kept during simulations and real data collection for the different receiver systems

Receiver System	Delay Locked Loop (DLL) Tracking Loop		Smoothing Interval (seconds)	Multipath Mitigation
	Bandwidth (Hz)	Order		
SEPT	0.25	2	Not Applied	Off
SEP2	0.25	2	Not Applied	Off
JAVD	3	1	100 (default)	Off

It is worth mentioning that in all the plots based on ISMR logs, the computed TEC is positive and is in TECU and for the sake of simplicity, it has been plotted as such instead of the receiver DCB which will come out with the opposite sign. But to maintain consistency with the receiver DCB estimates computed and plotted from the RINEX observation data, the receiver DCB terms in equations (3.16) and (3.17) have been rearranged to take into account that the STEC was always set to zero in all the simulations and to bring in the correct sign which is negative in this case. To make the estimated receiver DCB compatible with the published DCB products, the receiver DCB estimated from the RINEX observation data has always been presented in nanoseconds in the rest of the thesis.

5.1.1 **Defined scenario for the simulations**:

The scenario, as used by Ammar (2011), was set out in all the starting simulations. However, instead of generating only GPS signals, all the available signals for both GPS and Galileo were simulated (Table 5.3). Later, when the calibration procedure for DCB estimation was streamlined, the scenario was set to a more recent start date and start time in line with the simulator's updated orbit files and the duration of the simulation was set to 26 hours. The station's location in the scenario was also updated to NGI's geographical location (Table 5.4).

Table 5.3 SimGEN^{TM} Scenario Parameters

Start Date	31 June, 2011
Start Time	12:00:00
Location	S 22° 7.19424´, W 51° 24.5118´, 433.641 (geoid)
Duration	No fixed duration (varies from 30 minutes to 24 hours)
Simulated Signals	GPS L1-C/A, GPS L1-P, GPS L2-P, GPS L5, Galileo E1, Galileo E5a
Signal Strength	Modelled or Fixed
Estimated Group Delay Differential - T_{GD} and B_{GD}	0
Tropospheric Delay	Disabled
Ionospheric Delay	Off (TEC = 0)

Table 5.4 Updated SimGEN^{TM} Scenario Parameters

Start Date	31 Jan, 2016
Start Time	22:00:00
Location	N 22° 7.19424´, W 51° 24.5118´, 433.641 (geoid)
Duration	No fixed duration (varies from 30 minutes to 26 hours)
Simulated Signals	GPS L1-C/A, GPS L1-P, GPS L2-P, GPS L5, Galileo E1, Galileo E5a

Signal Strength	Modelled or Fixed
Estimated Group Delay Differential - T_{GD} and B_{GD}	0
Tropospheric Delay	Disabled
Ionospheric Delay	Off (TEC = 0)

5.1.2 **Configuration of Septentrio PolaRxS Pro Receiver:**

In all the simulations and in the open sky real data collection, the configuration of PolaRxS Pro receiver was kept constant such that:

- The receiver is set to track all available signals of both GPS and Galileo constellations.
- The multipath mitigation is kept off.
- Both ionospheric and tropospheric models are disabled.
- The frontend automatic gain control (AGC) is kept off.
- The adaptive tracking loop parameters are turned off.

5.1.3 **Configuration of Javad Triumph–I Receiver:**

In all the simulations and in the open sky real data collection, the configuration of Triumph–I receiver was kept constant such that:

- The receiver was set to track all available signals of both GPS and Galileo constellations.
- The multipath mitigation was kept off.
- The anti-interference was turned off.

5.1.4 **Cable DCB**:

To rule out any minor effect coming from the cable, the same antenna cable of 20 meters RG213 length was used with the SEPT receiver both to connect it with the simulator and to connect it with the antenna for open sky data collection. On the other hand, the same was not possible for the other two receivers, SEP2 and JAVD, because of the difficulty in taking existing routed cables out of the building fixtures between the roof and the NGI's GNSS lab. Therefore, to keep the noise level to a minimum, the shortest available 1-meter cable was used to connect them to the simulator during the estimation of their respective DCBs.

5.1.5 **Antenna DCB**:

For the specific NovAtel GPS 702GG antenna that was used initially with the SEPT receiver, the DCB of -2.7 ns was provided by the manufacturer between L1 and L2. It was measured at 23°C and with 4.53V power supply (Andreotti, 2016).

For the Leica AR10 antennas that were used initially with the SEP2 and JAVD receivers, the DCB value of 3 ns between L1 and L2 was provided (Leica, 2016). This is not antenna specific and is just the maximum DCB value as estimated by the manufacturer at 22°C for all the Leica AR10 antennas. More recently, to accommodate the newer GPS L5 and Galileo signals, the antenna used with the SEPT receiver has been upgraded to the NovAtel GPS 703GGG. For this particular antenna, the DCBs between L1 and L2 and between L1 and L5 (or E1 and E5), as computed by the manufacturer at 25°C and with 4.5V power supply, are 2.2 ns and 1.3 ns, respectively (Andreotti, 2016). SEP2 antenna has also been upgraded to Septentrio choke ring antenna but no differential group delay value has been provided by the manufacturer.

5.2 Satellites and Receivers DCBs Estimation from Real Data:

Initially 'Network A' of 96 stations, comprising of 93 IGS stations and 3 additional stations, namely SEPT, SEP2 and JAVD that were set up at the NGI, was chosen to be part of the global ionospheric analysis using the DCB_FIX software. These stations are represented by red dots in Figure 5.1.

For consistency and compatibility with the original M_DCB software, these stations were specifically selected to consist of GPS P1, P2 receiver types only. The estimated DCBs from the DCB_FIX software are later compared with the IGS published daily DCB estimates given in IONEX format. The estimated ionospheric coefficients as part of the LSQ processing are not analysed in any way for the generation of global ionospheric maps (GIMs).

To incorporate the modernized GPS L5 signal and the newer Galileo E1 and E5a signals, a new network of 41 stations comprising of 39 IGS or MGEX stations and 2 NGI stations i.e. SEPT and SEP2, was chosen to be part of the DCB estimation using the DCB_FIX software. This network is referred to as 'Network B' and the corresponding stations are represented by green dots in Figure 5.1. Also, this network selection was dictated by the fact that the SEPT receiver incorporates a pilot only tracking technique and limited receivers in the IGS or MGEX network are currently available with the same tracking technique.

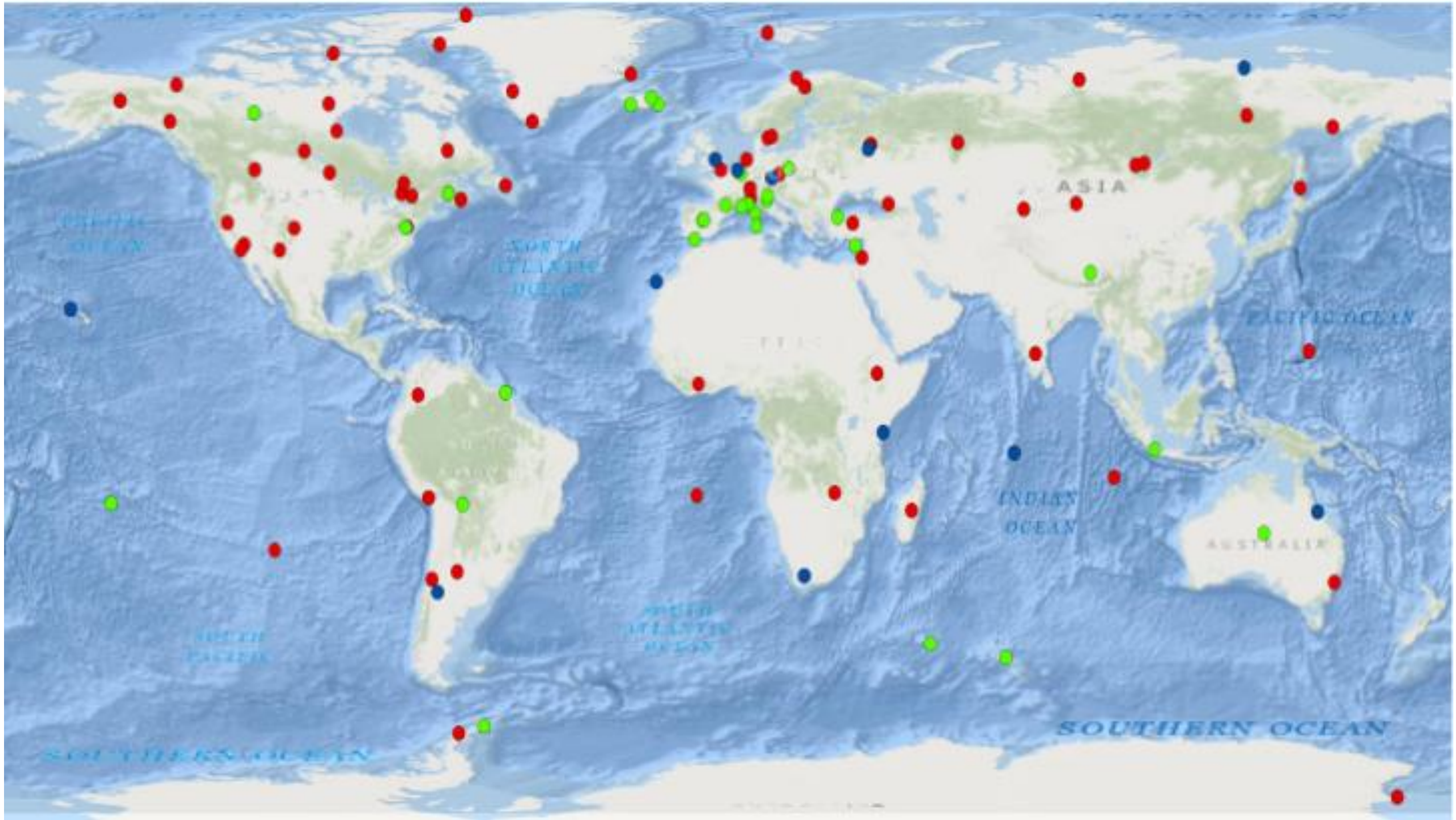

Fig. 5.1 Red – Network A; Green – Network B; Blue – Common stations in both the networks.

While Li et al. (2016) were able to use a network of 100 plus stations tracking Galileo based on their localized ionospheric modelling, it can still be a problem for the research groups working with a global ionospheric model to obtain a good spread of stations worldwide. Finally, the blue dots in Figure 5.1 are the stations that are common in both the networks.

CHAPTER 6

RESULTS AND DISCUSSION – Estimated Receiver DCBs using Simulator

The estimated receiver DCBs using simulated signals from Spirent hardware simulators have been presented and discussed in this chapter. The major part of the work carried out in this research is primarily based on the NGI's Spirent GSS8000 simulator. The opening Sections 6.1 and 6.2 of this chapter present the results from the simulations that were run on the GSS8000 simulator to assess the impact of simulator channels and different lengths of the antenna cable on the DCB estimation. A smoothing interval of 500 seconds was applied in the SEPT receiver on all signals during these simulations. This is done to reduce the overall noise of the TEC measurements. Section 6.3 has been added to describe a procedure that has been set out to estimate the DCB of any GNSS receiver through simulation. As mentioned earlier, in Chapter 5, the NGI's GSS8000 simulator has never been recalibrated since its purchase. So, to investigate the impact of uncalibrated and calibrated simulators, Sections 6.4 to 6.6 present the estimated DCBs between uncalibrated and calibrated Spirent simulators.

6.1 Effect of Simulator Channels on Receiver DCB Estimation (Based on Uncalibrated GSS8000 Simulator):

The experimentation phase started off by running numerous simulations with the aim to assess the magnitude of any systematic biases existing between the different channels of the simulator and thereby influencing the estimation of the receiver DCB. This was achieved by fixing the simulated satellites onto different channels of the simulator using the SimGen™ software and then tracking the simulated signals through the SEPT receiver using an RG213 coaxial cable of 1-meter length. In these initial simulations, neither the simulator nor the receiver were pre-warmed. It is important to highlight here that the resulting TEC computed by the PolaRxS receiver is an indication of the receiver DCB existing between the two signals used in the corresponding geometry free linear combination. Note that, in all the figures (excluding the one-way analysis of variance – ANOVA-I notched box plots) presented in this section, the colour dots are simply TEC measurements from different simulations, with dots of the same colour representing TEC measurements from one particular simulation, with its respective mean represented by a horizontal straight line of that same colour.

Figures 6.1 shows the TEC computed by the PolaRxS receiver using the L1 and L2 signals of four GPS satellites from a set of four 1-hour simulations against the GPS Time of Week (TOW). In these simulations, each satellite has been moved around the four channels of a particular channel card of the simulator. To make it easier to understand, Figure 6.2 shows a pictorial sketch of the internal configuration of the two RF banks within a GSS8000 simulator. So, if PRN '1' is taken as example, it has been moved during these four simulations from Channel '1' to Channel '4' of the channel card '1'. Similarly, PRN '3', PRN '6' and PRN '11' have been moved between channels of the channel card '2', channel card '3' and channel card '4', respectively. Figure 6.2 also shows the scenario that was set in the first simulation. On the other hand, Figure 6.3 shows the TEC computed by the PolaRxS receiver using the same signals as above but

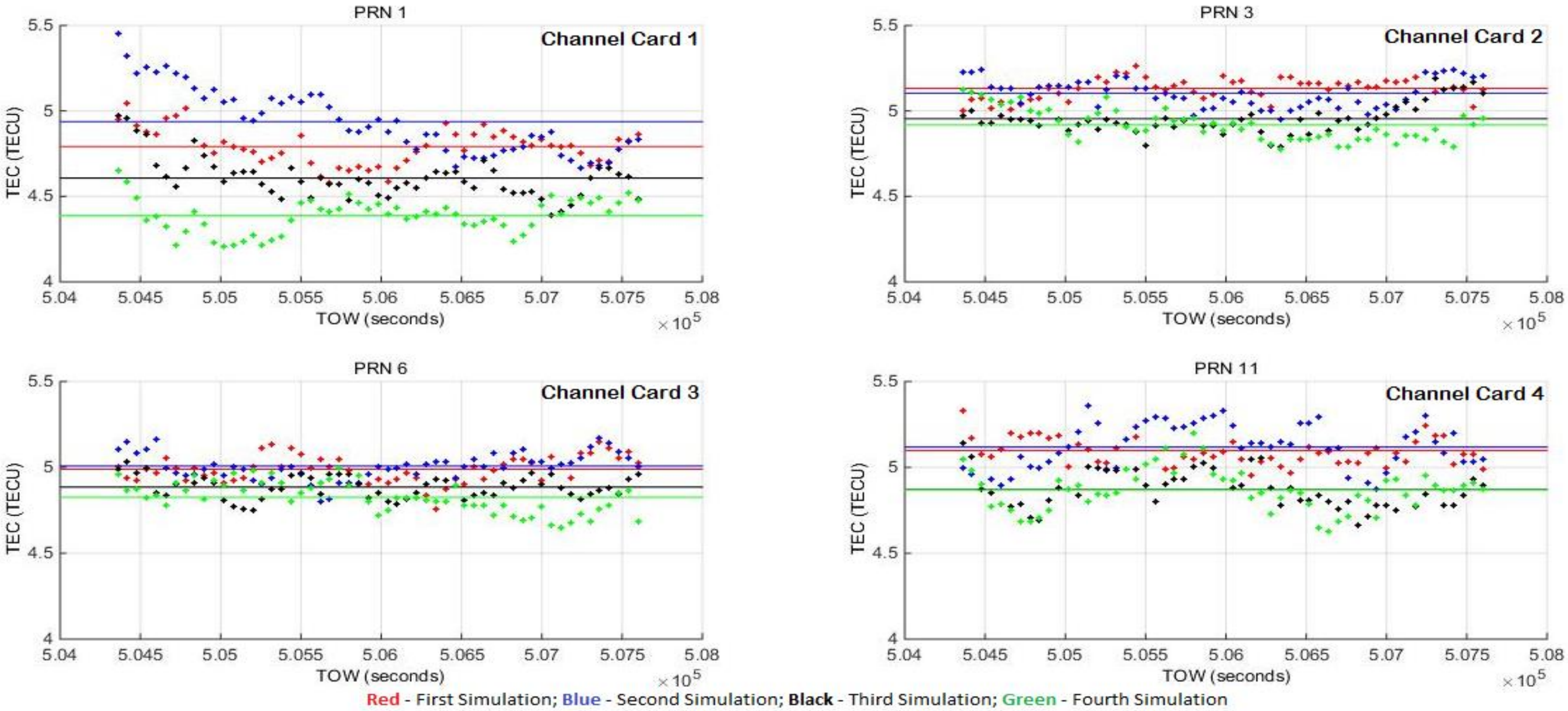

Fig. 6.1 Plots showing variations in TEC (in TECU) with respect to GPS TOW (in Seconds) for PRN 1. PRN 3, PRN 6 and PRN 11 across different channel cards of the simulator (PolaRxS – Smoothing Interval: 500 seconds on L1, 500 seconds on L2).

SIMULATION 1

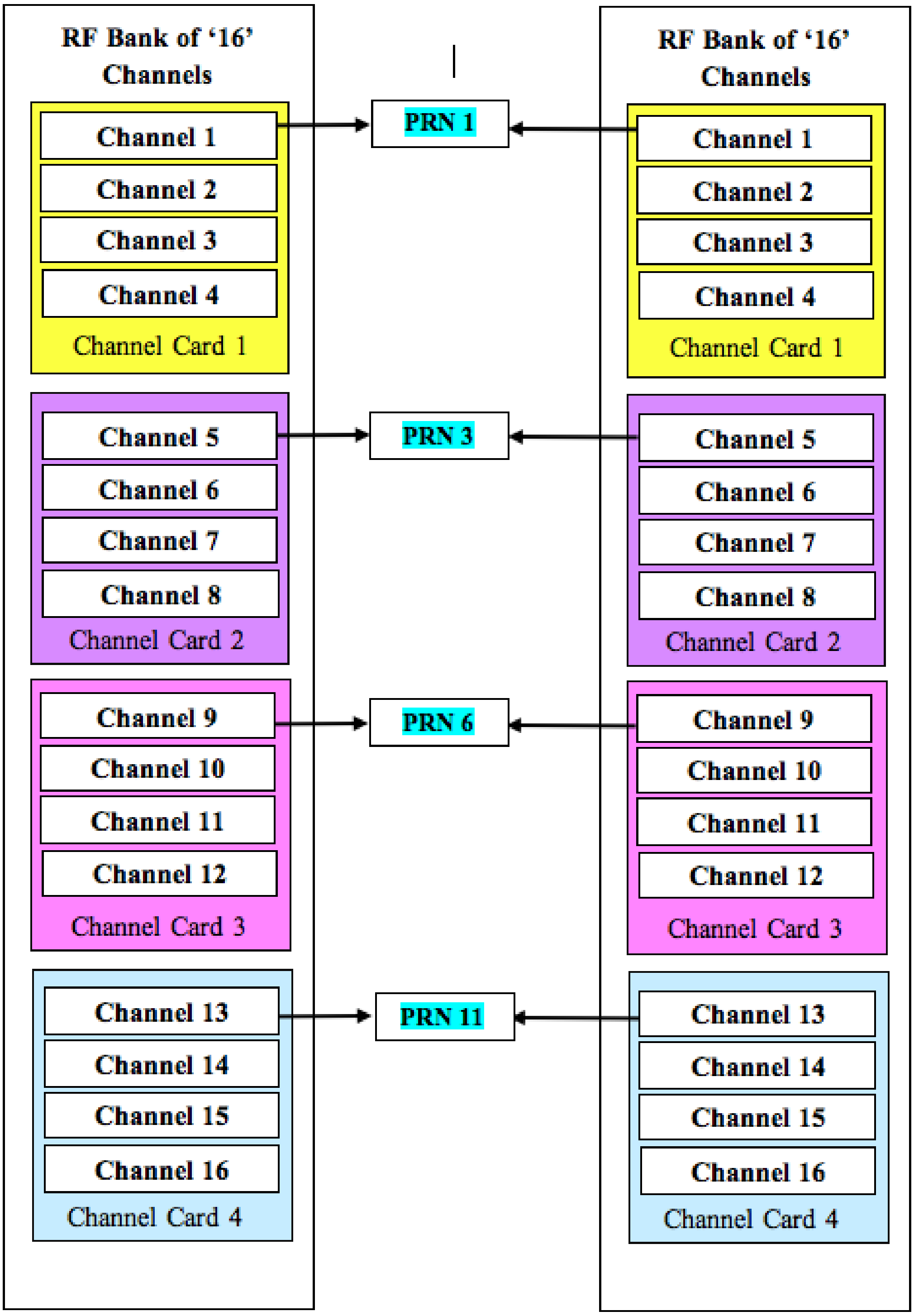

Fig. 6.2 Approximate pictorial sketch of the internal configuration of L1 and L2 RF banks of the GSS8000 simulator. Each RF bank comprises of 4 different channel cards and each channel card further comprises of 4 channels.

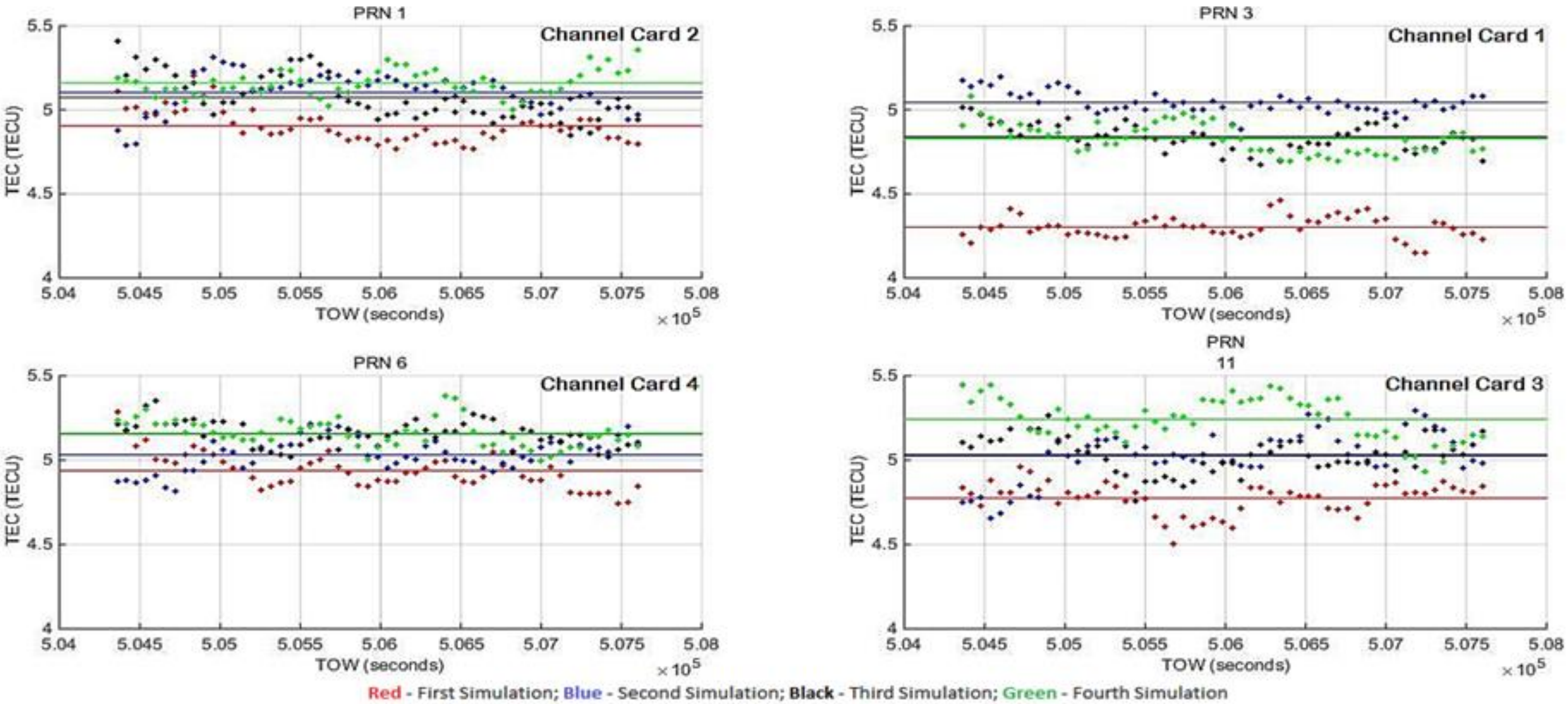

Fig. 6.3 Plots showing variations in TEC (in TECU) with respect to GPS TOW (in Seconds) for PRN 1. PRN 3, PRN 6 and PRN 11 across different channel cards of the simulator (PolaRxS – Smoothing Interval: 500 seconds on L1, 500 seconds on L2).

from another set of four 1-hour simulations in which PRN ‘1’ and PRN ‘6’ have been swapped over with PRN ‘3’ and PRN ‘11’, respectively, on their respective channel cards. By carefully analysing and comparing the responses coming from the different channel cards of the simulator using Figures 6.1 and 6.3, it was however not possible to establish any correlation between the different channel cards of the simulator.

While trying to assess the channel response from the Galileo signal generator using the above principle, it has been observed, as shown in Figure 6.4, that the TEC from the first of the four 1-hour simulations needs some time to become stable. This clearly shows the importance of pre-warming the simulator as well as the receiver, to not only allow the respective internal oscillators to stabilise but also to allow the internal operating temperatures to get steady. So, based on this, different levels of pre-warming in the order of 30 minutes to 2 hours were incorporated at the start of all the subsequent simulations. From the analysis of results, it has been observed that it takes almost two hours of simulation for the combination of receiver and simulator to produce stable TEC measurements. Hence it has been decided to run all the subsequent simulations for at least three hours. The first two hours of data are discarded straight away to allow the initial TEC measurements to stabilise and the TEC computed thereafter is used in the subsequent DCB analysis. Working on this approach, several simulations were run, and the results were analysed. To check whether the TEC measurements from the different simulator channels were statistically similar or not, an ANOVA-I test was run using MATLAB between the TEC measurements from the simulated satellites and the corresponding simulator channels on which these satellites are kept fixed (ANOVAI, 2015). The description of ANOVA-I test as implemented in the MATLAB software is given in Appendix C.

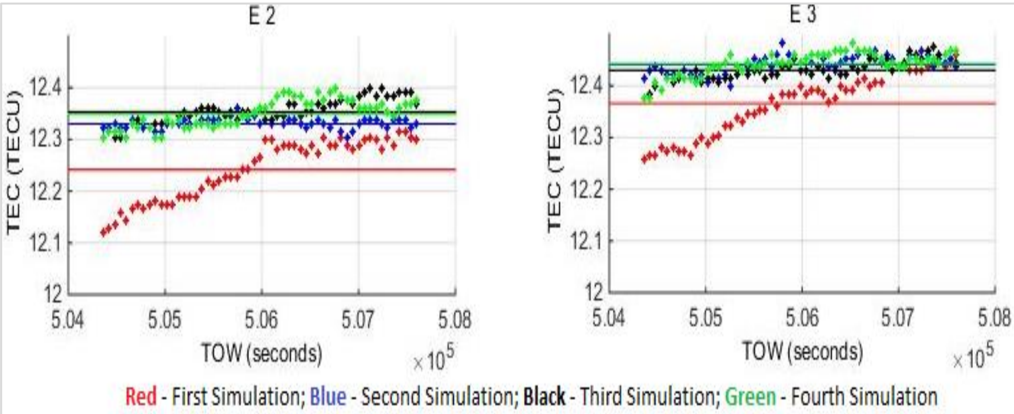

Fig. 6.4 Plots showing variations in TEC (in TECU) with respect to Galileo TOW (in Seconds) for E-2 and E-3 satellites over 4 different simulations (PolaRxS – Smoothing Interval: 500 seconds on E1, 500 seconds on E5a).

Figure 6.5 shows the result of one such ANOVA-I test while using one set of 4 different simulations. It has been ensured that during these simulations, the simulated satellites have occupied all the channels of the simulator. It can be seen that with a few exceptions, the TEC measurements contributed by the 4 channels within a channel card of the Galileo signal generator are statistically similar. On the whole, however, there are clear variations in the computed TEC across the 16 channels spread over four different channel cards. Some outliers in the form of + signs can also be observed in the figure. This can be explained on the basis that there are certain satellites appearing during the simulation on cold channels and they start producing stable TEC only after some time once the operating temperature for that particular channel becomes stable. The best way to deal with these satellites is to either discard their initial TEC measurements or to reject their entire data set so that they do not influence the final DCB analysis.

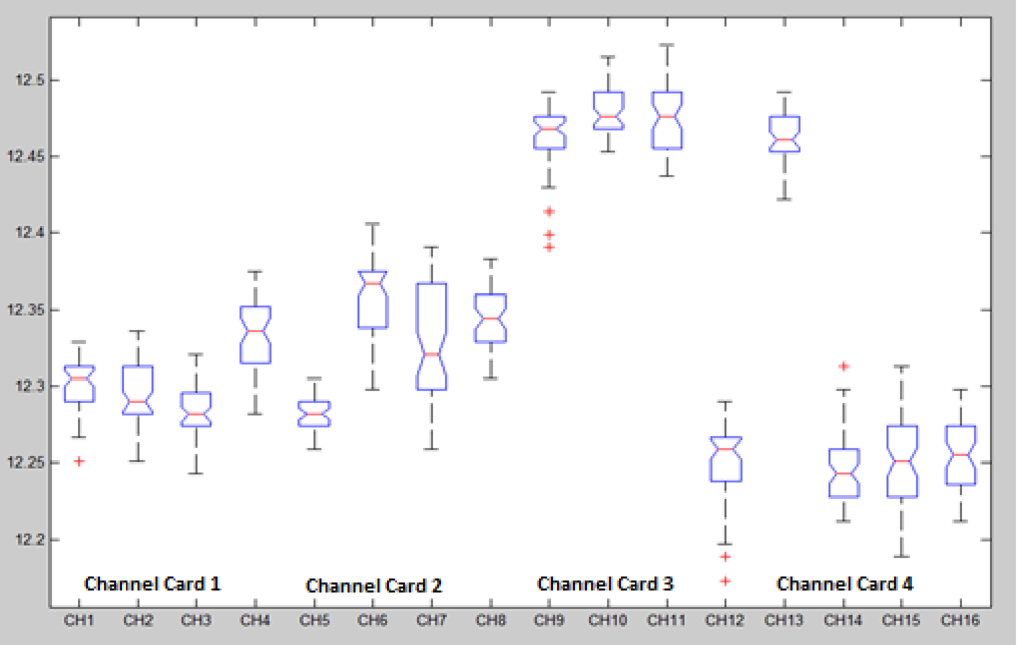

Fig. 6.5 Notched Box Plot between TEC measurements (y-axis) from simulated Galileo satellites and corresponding simulator channels (x-axis) on which these satellites are kept fixed (ANOVA-I, MATLAB).

There is a provision in the SimGEN™ software that allows the alignment of the code and carrier phases of each signal generator channel. This was not working well for the GPS signal generator, but it worked quite well for the Galileo signal generator. So, to benefit from the channel alignment utility, it was decided to generate only Galileo signals in all subsequent simulations. After running the channel alignment, Figure 6.6 shows the results of the ANOVA-I test from one simulation in which eight satellites are simulated on the first two channel cards of the Galileo signal generator. It can be observed that the channel alignment utility has worked well within a channel card but there is a distinct bias still existing between the two channel cards. The same effect has been observed in the results of the other two channel cards.

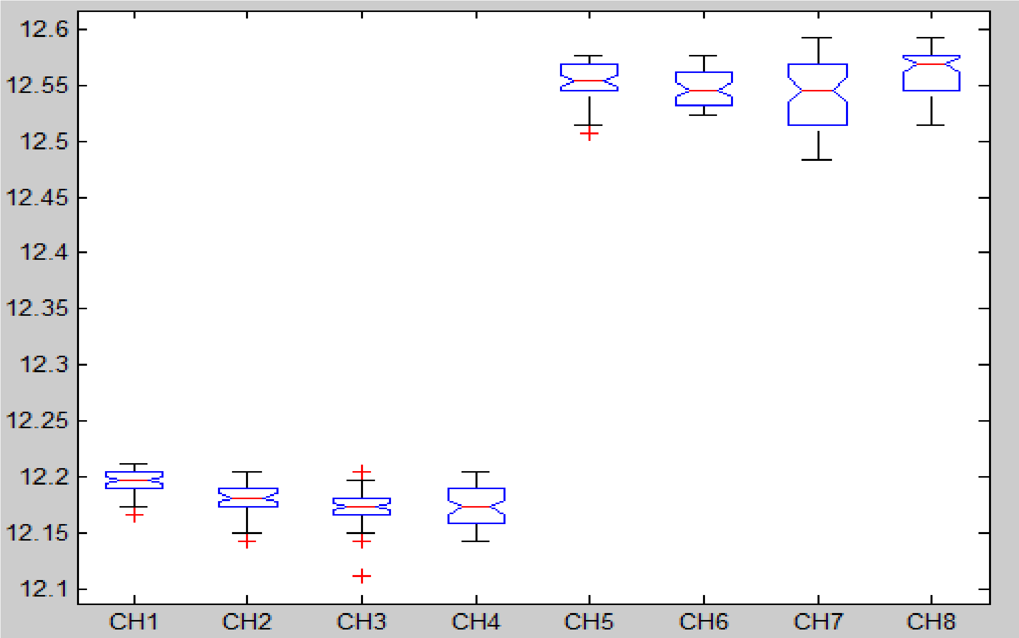

Fig. 6.6 Notched Box Plot between TEC measurements (y-axis) from simulated Galileo satellites and corresponding simulator channels (x-axis) on which these satellites are kept fixed. CH1 – CH4 are on the first channel card and CH5 – Ch8 are on the second channel card (ANOVA-I, MATLAB) – After Running the channel alignment utility.

At this stage, it was accidentally discovered that the inlet air filters of the signal generators were clogged up with dust. Once these were washed and reinstalled, the internal operating temperatures of both the GPS and Galileo signal generators (as reflected on their front display panels) immediately became lower. At relatively lower temperatures, the channel alignment was carried out again for the two generators. It still did not work well for the GPS signal generator but in the case of the Galileo signal generator, it started producing considerably smooth and precise results.

Figure 6.7 shows the ANOVA-I results from a rather long simulation run in which four of the simulated satellites are fixed on the fourth channel card, whereas the remaining satellites are randomly placed on the first three channel cards. This is done to ensure participation from all the simulator channel cards because otherwise the simulator generally places the satellites on the first available channels and normally the last channels remain free during the entire simulation run.

From Figure 6.7, it can be observed that the mean TEC for all the channels are very similar with very small scatter. Some outliers can still be seen, the reason for which has already been explained earlier. After looking at these results, it was concluded that because of the high operating temperatures in the earlier tests, the heat was not dissipating from the simulator and, consequently, systematic biases were being observed across the different channel cards. Also, it has been concluded that the results from all the simulator channels were very similar and hence thereafter no attempt was made to fix any satellite on any specific channel in the future simulations.

Overall, a variation of 0.1 to 0.2 TECU with a 1σ standard deviation of 0.02 to 0.03 TECU has been observed in the receiver DCB due to differential delays existing within the different channels of the Galileo signal generator. In the case of the GPS signal generator, even without the proper alignment of channels, a variation of 0.7 to 0.8 TECU with a 1σ standard deviation of 0.08 to 0.12 TECU has been observed in the receiver DCB due to differential delays existing between its channels.

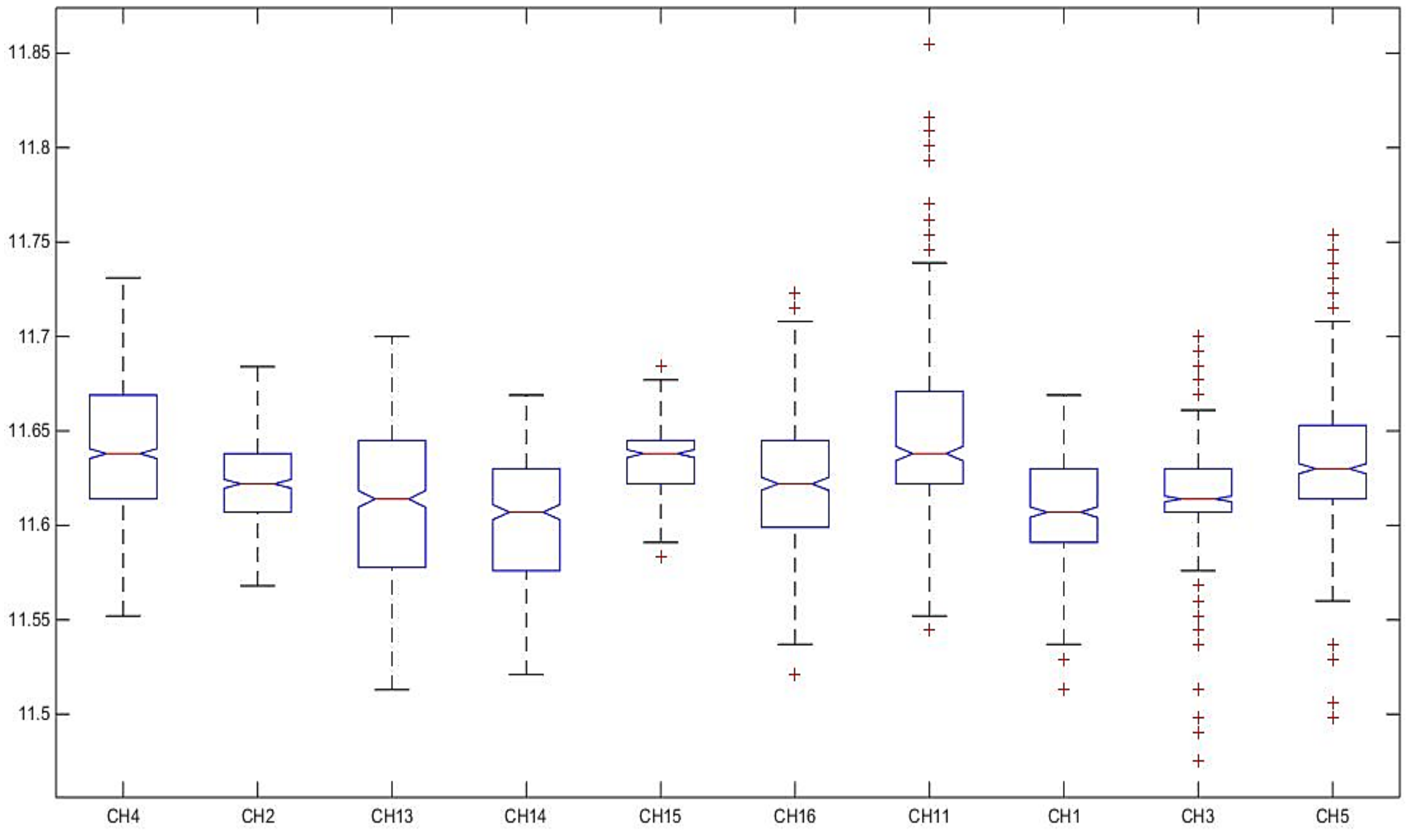

Fig. 6.7 Notched Box Plot between TEC measurements (y-axis) from simulated Galileo satellites and corresponding simulator channels (x-axis) on which these satellites are kept fixed (ANOVA-I, MATLAB) – After cleaning and reinstalling inlet air filters and re-running of channel alignment utility.

6.2 <u>Effect of the Length of the Cable on Receiver DCB estimation (Based on Uncalibrated GSS8000 Simulator)</u>:

Since the start of the research, many simulations were run to study the effect of the varying cable length on the receiver DCB. As the initial results were corrupted by both the lack of channel alignment as well as the high internal operating temperatures because of blocked inlet air filters, it would be quite misleading to present them herein and hence they were discarded. Once the inlet air filters were washed and reinstalled and the channel alignment was redone at a fairly stable operating temperature, the earlier simulations were repeated and from the results, it has been observed that with the increasing cable length, there is an increase in the electrical resistance and hence the increased thermal noise which is reflected in the noisier TEC measurements. This has also been validated by the corresponding decrease in signal to noise ratio (C/N0) with the increasing cable length, on both the signals used in computing TEC.

Figure 6.8 shows the overlapping results of the two simulations; one of which is run with a 1-meter cable and the other which is run with a 30-meter cable. The duration of each simulation is three hours. To account for the time required for the internal operating temperature to become stable, the first two hours are discarded in both the simulations. It can be seen that with the 30-meter cable, the TEC measurements are much noisier and slightly smaller as opposed to the fairly stable 1-meter cable results. Working with different lengths of the RG213 cable, the variation in the receiver DCB was found to be of the order of 0.1 TECU to 0.2 TECU with a 1σ standard deviation of 0.025 to 0.045 TECU. It must be noted here that the RG213 cable is a high-quality antenna cable and these relatively lower variations are somewhat expected.

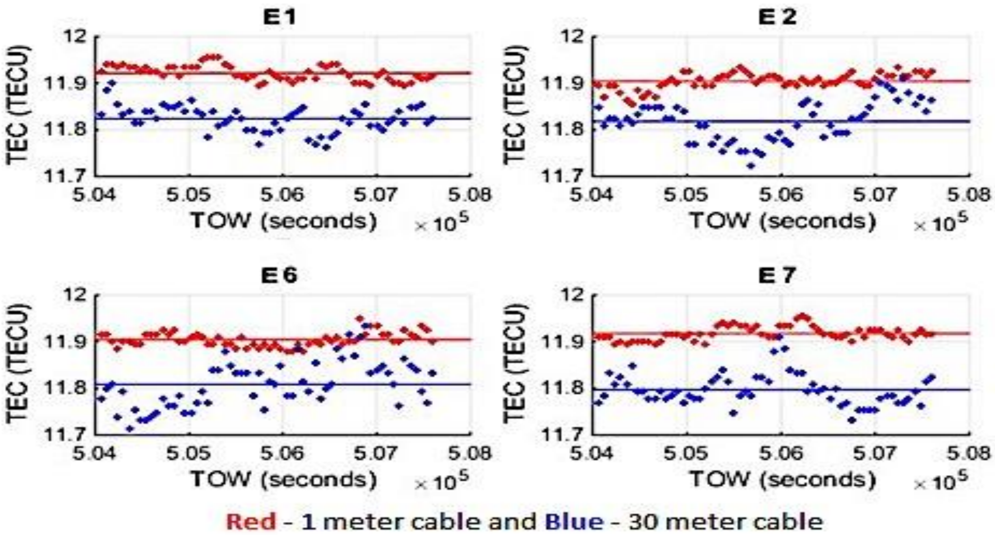

Fig. 6.8 Plots showing variations in TEC (in TECU) with respect to Galileo TOW (in Seconds) for four Galileo satellites (PolaRxS – Smoothing Interval: 500 seconds on E1, 500 seconds on E5a).

Figure 6.9 shows the variations in the L2 C/N0 during seven separate simulations and each of these two-hour simulations was run with a different cable length. The sort of decreasing trend in the L2 C/N0 can be picked up straightaway with the increasing length of the cable, although this is not as prominent in the smaller 2-meter to 5-meter cable lengths. The other important observation that can be seen here is the ability of the SEPT, i.e. the PolaRxS receiver, to track the L2 signal at such a low C/N0 ratio of approximately 15 dB-Hz, which is quite remarkable.

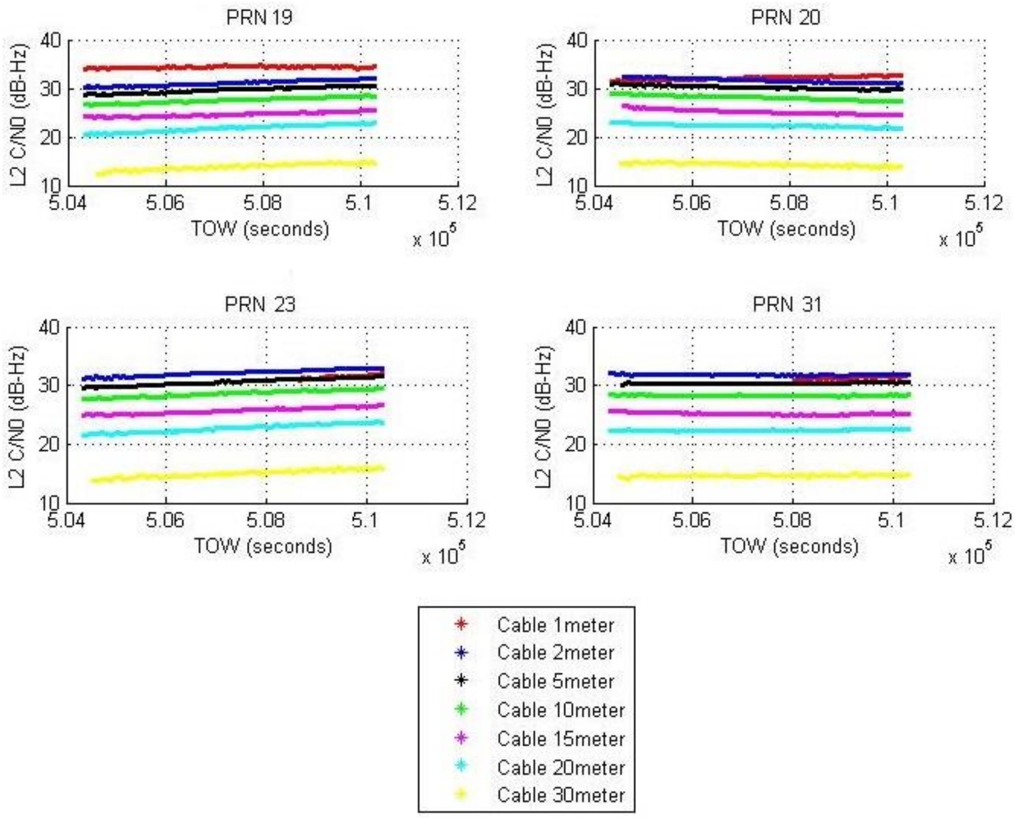

Fig. 6.9 Plots showing variations in L2 C/N0 (in dB-Hz) with respect to TOW (in Seconds) for four GPS satellites under varying lengths of the connecting cable (PolaRxS – 500 seconds on L2).

6.3 <u>Stepwise Procedure for the Estimation of Receiver DCB using a Hardware Signal Simulator</u>:

From the experimental analysis conducted in sections 6.1 and 6.2, the following procedure was devised to estimate the receiver DCB of any multi-frequency, multi-constellation GNSS receiver:

- As the simulator is the most important aspect of this research, it should be well maintained and calibrated.

- In the case of the Spirent GSS8000 simulator, the channel alignment should ideally be done before starting the calibration procedure through the channel alignment utility available in the SimGen^{TM} software.

- Define a suitable location on the globe in the scenario through SimGEN^{TM}. Any suitable location can be set up with good satellite visibility as all the location defined features were kept disabled in the set scenario. Three different simulations (26 hours each) should be run using the defined scenario. The RINEX or ISMR logs (in case of PolaRxS Pro) can be generated on a 24 hours basis and the start time can be set for 2 hours prior to midnight. This allows the user to easily discard the first two hours of the simulation and an undisturbed single 24 hours RINEX file or ISMR can be obtained for convenient data processing. The choice of running 26 hours of a simulation run was made to allow for the maximum participation from all the simulator channels. The choice of running 3 different simulation runs was made to carry out reasonable statistical analysis later. As an ISMR file is based on GPS P1 and P2 pseudoranges only, it is suggested to compute the DCB directly from the RINEX observations so that all the other signals can also be included in the calibration. Additionally, if ISMR logs are used and considering they provide the TEC values, then the sign of the measurements must be changed to get the correct receiver DCB estimate.

- The DCB is a systematic bias inherent to the satellite or receiver hardware. So, whether the code smoothing is applied or not, it won't affect the receiver DCB. In the absence of smoothing, the increased noise in the DCB observable based on equations (3.16) and (3.17) can be mitigated by taking the mean of all the measurements.

- Compute the separate means of the receiver DCB estimate for each of the three simulations and verify that these are statistically similar.
- Calculate the overall mean of the three receiver DCB estimates in order to obtain the receiver DCB of any required signal combination.

6.4 Estimated Receivers DCBs using Simulation (Based on Uncalibrated GSS8000 Simulator):

To estimate the DCB of the SEPT receiver, data from three 26 hours simulations was captured, where the ionosphere, troposphere and the group delays are set to 0. The simulated signals are recorded by the SEPT receiver using a 20 meters RG213 coaxial cable. The first two hours of the simulations were always discarded to allow for the simulator and the receiver hardware to reach stable operating temperatures. The DCBs for the desired signal combinations were computed independently from the pseudoranges as recorded in the RINEX observation files and not the ISMR logs.

Figures 6.10 and 6.11 show the estimated DCBs for the SEPT receiver between GPS P1/P2, C1/P1, C1/P2, C1/C5 and Galileo E1/E5a. The mean and 1σ standard deviation of these DCBs (in ns) across the three simulations were found to be – 1.70 ± 0.53, 0.03 ± 0.09, – 1.67 ± 0.52, – 4.97 ± 0.44 and – 5.21 ± 0.26, respectively. The consistency between these estimates was confirmed by verifying the following relation:

$$DCB\ (C1 - P1) + DCB\ (P1 - P2) = DCB\ (C1 - P2)$$

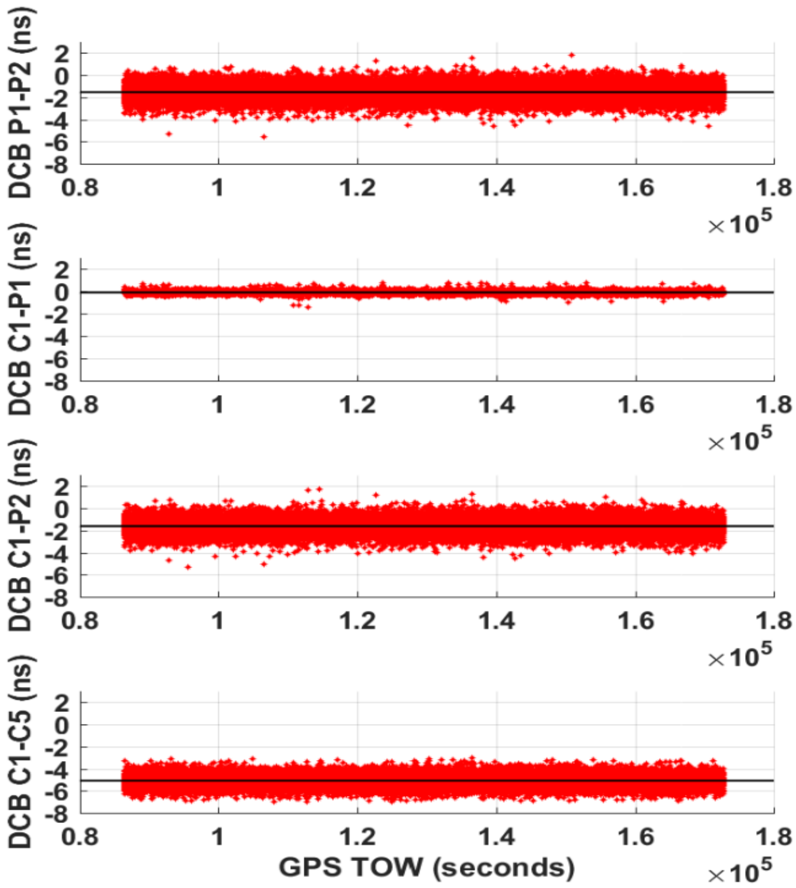

Fig. 6.10 Plots showing DCBs between different GPS signal combinations (in ns) vs. GPS TOW (in Seconds) as observed by all the satellites in one simulation run (SEPT Receiver)

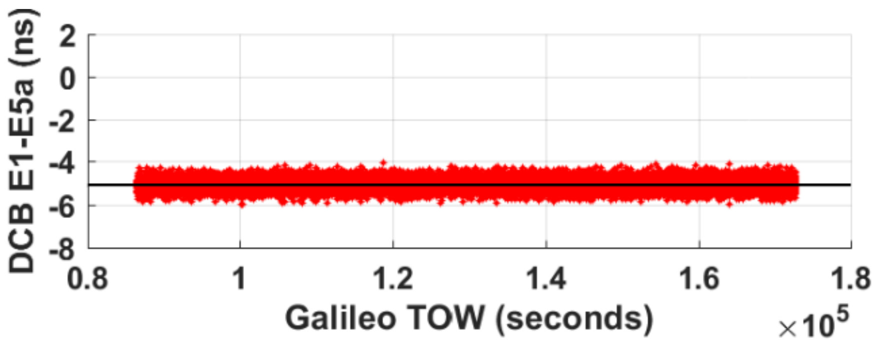

Fig. 6.11 Plot showing DCB between Galileo E1 and E5a (in ns) vs. Galileo TOW (in seconds) as observed by all the satellites in one simulation run (SEPT receiver).

From the relatively lower DCB (C1-P1), it appears that C1 code measurements are smoothed by default. However, this is due to the tracking technique that is employed by Septentrio to track the GPS ‘P’ code, which results in the noise on the P1 code measurements being strongly correlated with the noise on the C1 code measurements (Sleewaegen, 2015). When one is subtracted from other, the resulting noise is very small. The C1 code measurement itself is not smoothed (Septentrio, 2016).

Following the same methodology, Figures 6.12 and 6.13 show the DCB estimates for SEP2 and JAVD receivers, respectively, for only the GPS P1/P2 code combination. The mean and 1σ standard deviation of these DCBs (in ns) across the three simulations were found to be -1.90 ± 0.31 and 6.83 ± 1.35, respectively.

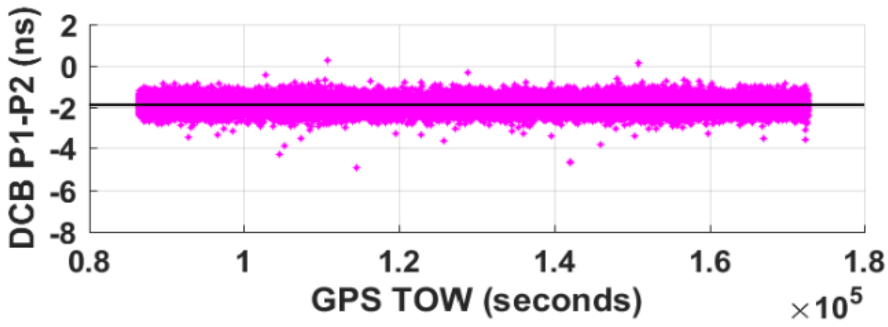

Fig. 6.12 Plot showing DCB between GPS P1 and P2 (in ns) vs. GPS TOW (in Seconds) as observed by all the satellites in one simulation run (SEP2 receiver).

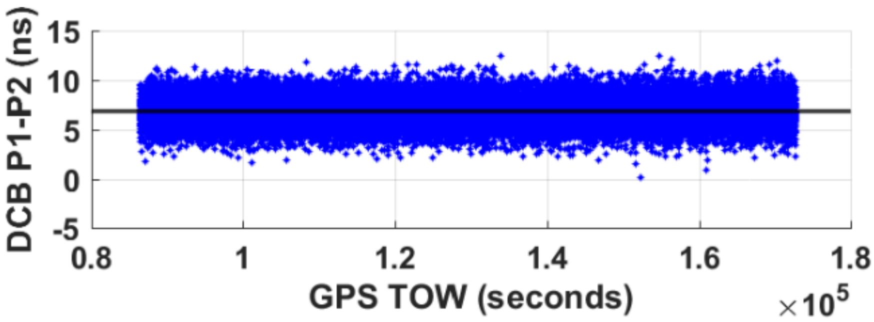

Fig. 6.13 Plot showing DCB between GPS P1 and P2 (in ns) vs. GPS TOW (in Seconds) as observed by all the satellites in one simulation run (JAVD receiver).

From Figures 6.10 to 6.13, it can be seen that the ISMRs present a lower noise level than the JAVD receiver even without the application of carrier phase smoothing. However, keeping in mind that the ISMRs are working under the default tracking parameters as reflected in Table 5.2, a fair comparison would only be possible by using a consistent set of tracking parameters for all the three receivers.

To study the impact of consistent tracking parameters between the SEPT and JAVD receivers, some additional simulations were run towards the end of the research while using consistent tracking loop parameters between the two receivers and by keeping all the other variables fixed. In the PolaRxS receivers, the order of the DLL is set by default to '2' and there is no provision to change it in any way. On the other hand, where one can change the order of the DLL in the case of Javad receiver, the bandwidth can only be set to one decimal figure i.e. instead of 0.25 Hz, the user can only set either 0.2 Hz or 0.3 Hz. Keeping these restrictions in mind, Table 6.1 gives a comparison between the results previously presented in this section and the results based on additional simula-

Table 6.1 Comparison of DCB estimates of the SEPT and the JAVD receivers based on the varying tracking loops parameters. (RG213 1-meter Cable)

Receiver System	Signal* Combination	DLL Bandwidth (Hz)	DLL Order	PLL Bandwidth (Hz)	Smoothing (seconds)	Mean DCB (ns)	Standard Deviation (ns)	Remarks
SEPT *(Old)*	P1 – P2	0.25	2	15	0	– 1.70	± 0.53	*Based on the simulated data of 2016 that was collected under the default tracking loop parameters of the PolaRxS receiver.*
	C1 – P1					– 0.03	± 0.09	
	C1 – P2					– 1.67	± 0.52	
SEPT *(Recent)*	P1 – P2	3	2	25	100	– 1.74	± 0.10	*Based on the simulated data of 2017 that was collected under the default tracking loop parameters of the Javad receiver.*
	C1 – P1					0.01	± 0.06	
	C1 – P2					– 1.73	± 0.10	

JAVD *(Old)*	P1 – P2	3	1	25	100	6.83	± 1.35	*Based on the simulated data of 2016 that was collected under the default tracking loop parameters of the Javad receiver.*
	C1 – P1					– 1.41	± 2.92	
	C1 – P2					5.42	± 2.92	
JAVD *(Recent)*	P1 – P2	0.2	2	15	0	8.13	± 0.84	*Based on the simulated data of 2017 that was collected under the default tracking loop parameters of the PolaRxS receiver.*
	C1 – P1					0.46	± 0.77	
	C1 – P2					8.60	± 0.56	

Note:

* *The DCB estimates for L5 and E5 signals are not presented because for some reasons, the Javad receiver does not track those signals in the recent simulations.*

tions with consistent tracking loop parameters. In Table 6.1, the highlighted part in blue gives the latest results (2017) and the non-highlighted part gives the previous (2016) results. By looking at the SEPT results, it can be seen that almost similar results have been yielded under the varying tracking loop parameters. By replicating the JAVD's tracking loop parameters, the standard deviations of the DCB estimates have in fact become lower but this can be attributed to the fact that it is being done with a 100 seconds smoothing. In the presence of smoothing, the default tracking loop parameters would have yielded the same sort of results. By looking at the JAVD results, an improvement in the standard deviations can be readily observed but relatively higher DCB estimates are observed in comparison to the previous estimates. To investigate this variation, the simulations from the past, that were used to estimate the DCBs of the two receivers i.e. SEPT and JAVD at the first instant, were re-run. Table 6.2 gives the results from these newer simulations. Again, in the case of SEPT receiver, almost similar DCB estimates have been generated, whereas in the case of JAVD receiver, the DCB estimates for different signal combinations have increased by approximately 1 – 2 ns. Here, it is pertinent to mention that the SEPT receiver was never allowed to leave the NGI's GNSS Lab environment. On the other hand, the JAVD receiver is frequently used in the practical field surveys in addition to the lab testing. So, the regular wear and tear over the service life of the receivers could be responsible for altering these DCBs. Another factor could have been the temperature variations but considering that both the receivers have been exposed to almost similar conditions, it is safe to rule out this hypothesis.

In addition to the simulations whose results are presented in Table 6.2, some additional simulations were also run with the JAVD receiver but using the RG-

Table 6.2 Comparison of older (2016) and recent (2017) DCB estimates of the SEPT and JAVD receivers under the default tracking loop parameters. (RG213 1-meter Cable)

Receiver System	Signal* Combination	DLL		PLL Bandwidth (Hz)	Smoothing (seconds)	Mean DCB (ns)	Standard Deviation (ns)	Difference from the past results (ns)	Remarks
		Bandwidth (Hz)	Order						
SEPT *(Recent)*	P1 – P2	0.25	2	15	0	– 1.77	± 0.40	– 0.07	*Based on the simulated data of 2017 that was collected under the default tracking loop parameters of the PolaRxS receiver to replicate 2016 results.*
	C1 – P1					0.02	± 0.07	– 0.01	
	C1 – P2					– 1.75	± 0.40	– 0.08	
JAVD *(Recent)*	P1 – P2	3	2	25	100	7.62	± 0.83	0.80	*Based on the simulated data of 2017 that was collected under the default tracking loop parameters of the Javad receiver to replicate 2016 results.*
	C1 – P1					0.40	± 1.40	1.81	
	C1 – P2					8.03	± 1.40	2.61	

Note:

* *The DCB estimates for L5 and E5 signals are not presented because for some reasons, the Javad receiver does not track those signals in the recent simulations.*

58AU 3-meter cable. Table 6.3 presents the results of these simulations. The change in the DCB estimates with respect to Table 6.2 can be attributed to a longer cable length. However, it can be established that there is no improvement in the DCB estimates under varying tracking loop parameters and the smoothing does not affect the DCB estimates but only improves their standard deviations.

From the discussion presented so far, a word of caution can be made to use the receivers with care and to follow the handling instructions as specified by the manufacturers under all circumstances, especially if such receivers are involved in ionospheric monitoring.

6.5 Estimated Receivers DCBs using Simulation (Based on Uncalibrated GSS9000 Simulator):

An uncalibrated Spirent GSS9000 simulator was loaned to NGI by Spirent for carrying out some miscellaneous research tasks. Taking advantage of this opportunity, some simulations were run based on the defined scenario given in Table 5.4.

Figure 6.14 shows the estimated DCB for the SEPT receiver between Galileo E1/E5a signals. The different colours indicate the 3 different one-hour sessions of the 3 hour simulation. The increasing trend of the measured TEC can be readily picked up from the plots. This was discussed with Spirent and it was found that the simulator clocks had been intentionally degraded in a previous experiment, before the loan to NGI, and never reset. Based on this finding, no further attempts were made to work with this uncalibrated GSS9000 simulator.

Table 6.3 Comparison of recent (2017) DCB estimates of the JAVD receiver under varying tracking loop parameters (RG58AU 3-meter Cable).

Receiver System	**Signal* Combination**	**DLL**		**PLL Bandwidth (Hz)**	**Smoothing (seconds)**	**Mean DCB (ns)**	**Standard Deviation (ns)**	**Remarks**
		Bandwidth (Hz)	**Order**					
JAVD	P1 – P2	3	1	25	0	8.70	± 1.21	*Based on the simulated data of 2017 that was collected under the default tracking loop parameters of the PolaRxS receiver to replicate 2016 results.*
	C1 – P1					0.40	± 2.00	
	C1 – P2					9.07	± 2.03	
	P1 – P2	3	1	25	100	8.70	± 0.84	*Based on the simulated data of 2017 that was collected under the default tracking loop parameters of the Javad receiver to replicate 2016 results.*
	C1 – P1					0.40	± 0.77	
	C1 – P2					9.10	± 0.78	
	P1 – P2	0.2	2	15	0	8.67	± 1.17	*Based on the simulated data of 2017 that was collected under the default tracking loop parameters of the PolaRxS receiver.*
	C1 – P1					0.42	± 1.14	
	C1 – P2					9.09	± 1.16	

Note: * *The DCB estimates for L5 and E5 signals are not presented because for some reasons, the Javad receiver does not track those signals in the recent simulations.*

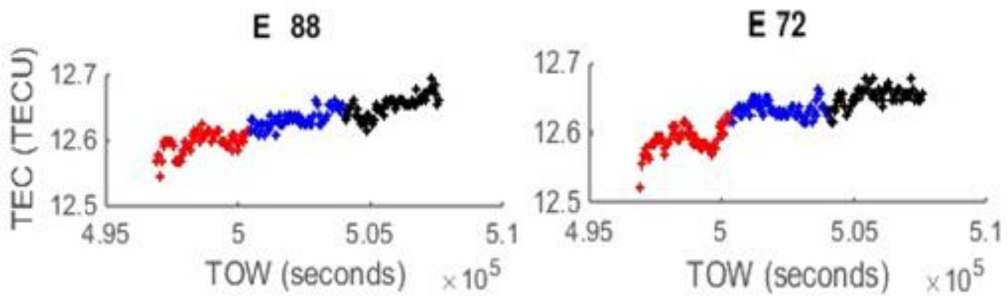

Fig. 6.14 Plot showing DCB between Galileo E1 and E2 (in TECU) vs. Galileo TOW (in Seconds) as observed by all the satellites in one simulation run (SEPT receiver).

6.6 Estimated Receivers DCBs using Simulation (Based on Calibrated GSS9000 Simulator):

During the visit to the Spirent facility in Paington, UK, the first accomplished task was the calibration of the Spirent GSS9000 hardware signal simulator that was scheduled to be used during the visit. The calibration procedure has already been described in Section 4.2.1. Once the calibration was completed, the following 1PPS-to-RF values were recorded:

- L1/E1: + 22 ps
- L2: – 281 ps
- L5/E5a: – 296 ps

As already stated, the positive values mean that the code transition occurs after the 1PPS rising edge, whereas, the negative values imply that the code transition occurs before the rising edge of the 1PPS. For Galileo signals, the actual 1PPS-to-RF values were not measured, as these were assumed to be similar to the GPS signals because if generated, they could have followed the same RF path in the GSS9000 hardware configuration. Again, as these signals were generated on the same FPGA along with their respective codes, for example, C1 and P1 codes, the differential code bias was assumed to be negligible. Using the above 1PPS-to-RF values, Table 6.4 gives the DCB estimates of the Spirent GSS9000 simulator that was used during the visit.

Table 6.4 DCB estimates of the GSS9000 hardware signal simulator

Signal Combination	Mean DCB (ns)	Standard Deviation (ns)	Remarks
L1 – L2	– 0.30	± 0.2	*The standard deviation of 0.2ns is an assumed value as specified by the manufacturer.*
L1 – L5	– 0.32	± 0.2	
L2 – L5	– 0.015	± 0.2	

Working on a similar strategy as described in Section 6.4 but with the RG213 1-meter cable instead of the 20-meter cable, Figures 6.15 and 6.16 show the estimated DCBs for the SEPT receiver between GPS P1/P2, C1/P1, C1/P2, C1/C5 and Galileo E1/E5a using the Spirent GSS9000 simulator. These DCB estimates are relatively close to the ones estimated from the Spirent GSS8000 simulator.

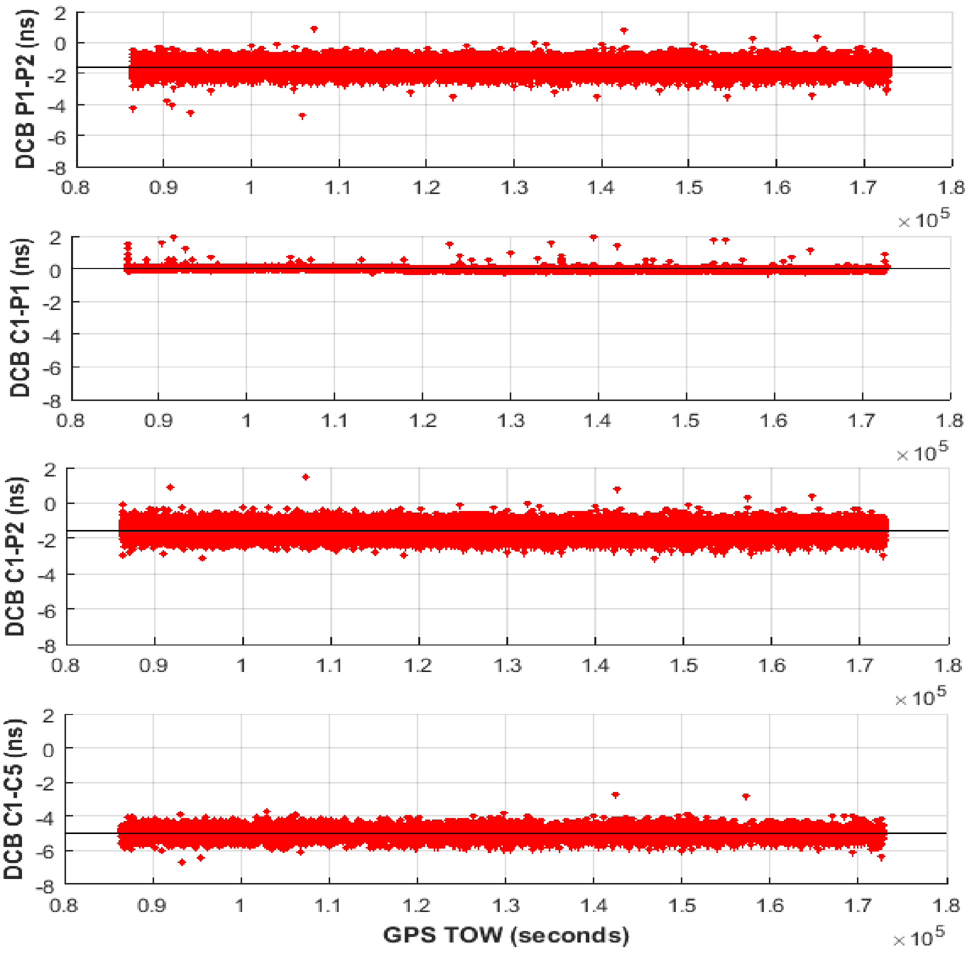

Fig. 6.15 Plots showing DCBs between different GPS signal pairs (in ns) vs. GPS TOW (in Seconds) as observed by all the satellites in one simulation run (SEPT Receiver)

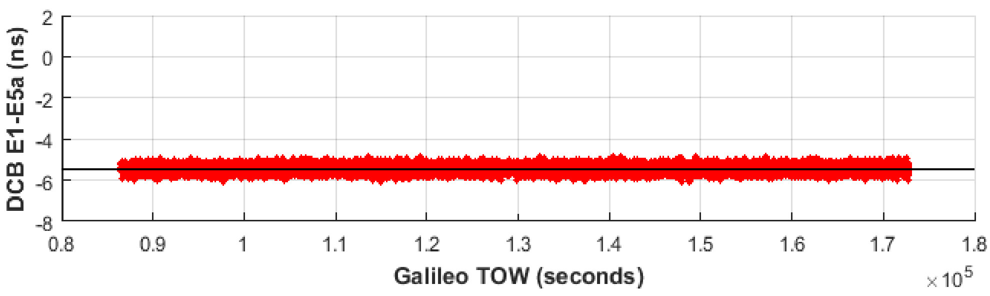

Fig. 6.16 Plot showing DCB between Galileo E1 and E5a (in ns) vs. Galileo TOW (in seconds) as observed by all the satellites in one simulation run (SEPT receiver).

Table 6.5 gives the mean and 1σ standard deviation of these estimated DCBs (in ns) across the three simulations. It also includes the adjusted DCBs after applying the necessary corrections from Table 7.3.

Table 6.5 Estimated and corrected DCBs for the SEPT receiver using the GSS9000 hardware signal simulator

Signal Combination	**Mean DCB (ns)**	**Standard Deviation (ns)**	**Corrected DCB (ns)**
P1 – P2	– 1.58	± 0.35	– 1.28
C1 – P1	0.02	± 0.07	0.02*
C1 – P2	– 1.56	± 0.34	– 1.26
C1 – C5	– 4.97	± 0.33	– 4.65
E1 – E5a	– 5.45	± 0.20	– 5.13
Note: * The DCB for two codes generated on the same FPGA is considered negligible.			

Apart from running simulations with the RG213 1-meter cable, some additional simulations were also run with the RG213 30-meter cable and the HUBER+SUHNER 1-meter cable. The results are tabulated in Table 6.6 and for comparison purposes, the results from the RG213 1-meter cable are also included. As the effect of simulator DCBs is constant for all these types, these DCBs are not the corrected ones. Table 6.6 confirms the earlier statement that noise is increased with a longer cable length and shows a variation of about 0.15 ns between the RG213 1-meter cable and the HUBER+SUHNER 1-meter cable. This variation is likely to increase between different cable types and needs more investigation.

Table 6.6 Estimated DCBs for the SEPT receiver using the GSS9000 hardware signal simulator and different cables

Cable Type and Length	Signal Combination	Mean DCB (ns)	Standard Deviation (ns)
RG213 (1-meter)	P1 – P2	– 1.58	± 0.35
	C1 – P1	0.02	± 0.07
	C1 – P2	– 1.56	± 0.34
	C1 – C5	– 4.97	± 0.33
	E1 – E5a	– 5.45	± 0.20
RG213 (30-meter)	P1 – P2	– 1.63	± 1.07
	C1 – P1	0.11	± 0.30
	C1 – P2	– 1.51	± 1.02
	C1 – C5	– 4.82	± 0.33
	E1 – E5a	– 5.31	± 0.43
HUBER+ SUHNER (1-meter)	P1 – P2	– 1.42	± 0.37
	C1 – P1	0.005	± 0.06
	C1 – P2	– 1.41	± 0.37
	C1 – C5	– 4.84	± 0.33
	E1 – E5a	– 5.31	± 0.18

Overall, the measurements recorded by the SEPT receiver using the GSS9000 simulator, were found to be highly repeatable, unlike the GSS8000 simulator. This again emphasises the importance of having a well-maintained hardware signal simulator, especially in the context of this type of research.

6.7 Manufacturer Supplied PolaRxS Pro DCBs (or Inter-frequency biases):

Figure 6.17 shows the nominal pseudorange inter-frequency bias (IFB) or DCB as a function of the carrier frequency as supplied by Septentrio for the PolaRxS receiver family (Septentrio, 2015). The IFB is plotted relative to the GPS L1 carrier frequency. The red dots mark the frequency of common GNSS carriers.

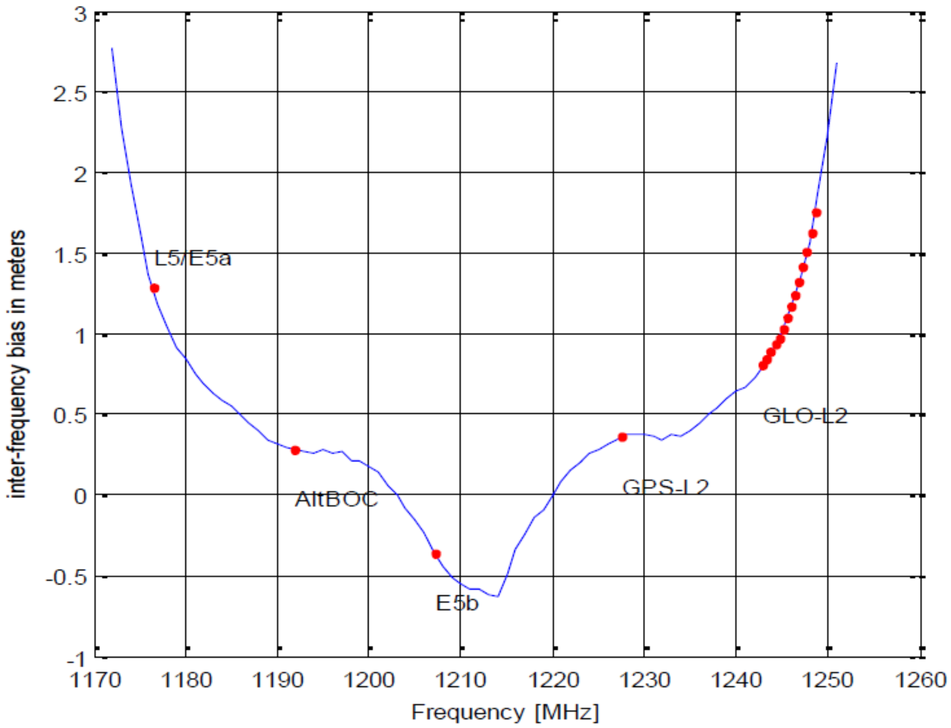

Fig. 6.17 Pseudorange IFB or DCB in the L2/L5 band relative to GPS L1.

In the above figure, an important aspect is that a positive IFB value at frequency *F* means that the pseudorange at that frequency is larger than the pseudorange at GPS L1. This is opposite to the sign of convention that has been adopted in this research and that is if the pseudorange at a certain frequency is larger than the pseudorange at GPS L1 or Galileo E1, then it is taken as a negative DCB. In accordance with this, the following DCBs (in ns) can be inferred from Figure 6.17 for the PolaRxS receiver family:

- L1 – L2: **-1.16** (or 0.35 m)
- L1 – L5/E1 – E5: **-4.34** (or 1.3 m)
- L2 – L5: **-3.17** (or 0.95 m)

Table 6.7 gives the estimated DCBs for the Septentrio receivers corrected for the simulator DCB. Considering that a ± 0.5 m (or ± 1.67 ns) unit to unit variation is expected by the manufacturer, the estimated DCBs for both the SEPT and SEP2 receivers have been found to be in good agreement to the above mentioned nominal DCBs as supplied by the manufacturer. Hence, it can be concluded that the proposed technique of estimating receiver DCBs using simulated signals is quite an effective way for estimating the receiver DCBs closer to their true physical values.

Table 6.7 Estimated DCBs for the Septentrio Receivers Only Excluding the Simulator DCB

Receiver	Signal Combination	Mean DCB (ns)
SEPT	P1 – P2	– 1.28
	C1 – C5	– 4.65
	E1 – E5a	– 5.13
SEP2	P1 – P2	– 1.48

CHAPTER 7

RESULTS AND DISCUSSION – Estimated Satellite and Receiver DCBs using Real Data

This chapter has been written to present and discuss the satellite and receiver DCBs that were estimated as part of global ionospheric analysis by adopting the CODE (IGS) strategy and by using a global network of IGS/MGEX stations. Based on the 'known' DCB estimate of SEPT receiver between different signal pairs using the uncalibrated GSS8000 simulator, the estimated satellite and receiver DCBs from a global network of stations are presented and discussed in Sections 7.1 to 7.2. Based on the same network DCBs, the estimated STEC using different calibration strategies are presented and discussed in Sections 7.3 and 7.4. Considering the importance of the simulator DCB in this research, a network-based calibration approach and a relative-calibration approach are described in Sections 7.5 and 7.6, respectively. Section 7.7 discusses the important conclusions that were drawn from a calibrated simulator in terms of DCB estimation of a network. Section 7.8 presents the DCB anomalies of SANT and VALD stations that were observed during the research. Section 7.9 presents the impact of a quiet and an active ionosphere on DCB estimation by analysing historical data of an IGS network under the ZM constraint experiencing the famous Halloween Storm of 2003.

Note that only selected results have been included in this chapter to avoid making the reading cumbersome.

7.1 Estimated Satellites and Receivers DCBs using Network A of GPS P1/P2 Only Stations (Based on Uncalibrated GSS8000 Simulator):

Using the DCB_FIX software with the archived RINEX data of 96 stations (Network A) from Mar 17 to Apr 7, 2016 (22 days) and the SH expansion of degree and order 15, the processing was run on a day to day basis with the solution constrained to the known DCB value of the SEPT receiver system. A known DCB value of -4.41 ns was used for the SEPT receiver system which is the sum of the antenna DCB (see Section 5.1.5) and the mean receiver DCB as computed in Section 6.4. Also, the selection of these 22 days was made on the basis that two additional receivers, i.e. SEP2 and JAVD, were available during that time to validate the results along with their antenna DCBs.

In Figures 7.1 and 7.2, the red curves show the mean DCBs as estimated by the IGS, whereas, the blue curves show the mean DCBs as estimated by the DCB_FIX software. Note that the mean DCB for both the satellites and receivers is computed over a period of 22 days. Also, in Figure 7.1, the GPS satellites are grouped together as per the different family blocks to which they belong. It can be observed that a similar pattern exists between the IGS computed DCBs and the DCBs estimated through the DCB_FIX software. However, stable mean offsets of -3.47 ns for satellites and +3.54 ns for receivers were found to exist between the estimated DCBs and the IGS published DCBs. An obvious explanation is that the zero mean constraint applied by the IGS to the satellites DCBs, although effective to break the rank deficiency, imposes an artificial bias in the estimated DCBs. By using a more realistic constraint in the form of a properly estimated receiver DCB, the resulting DCBs are shifted closer to their

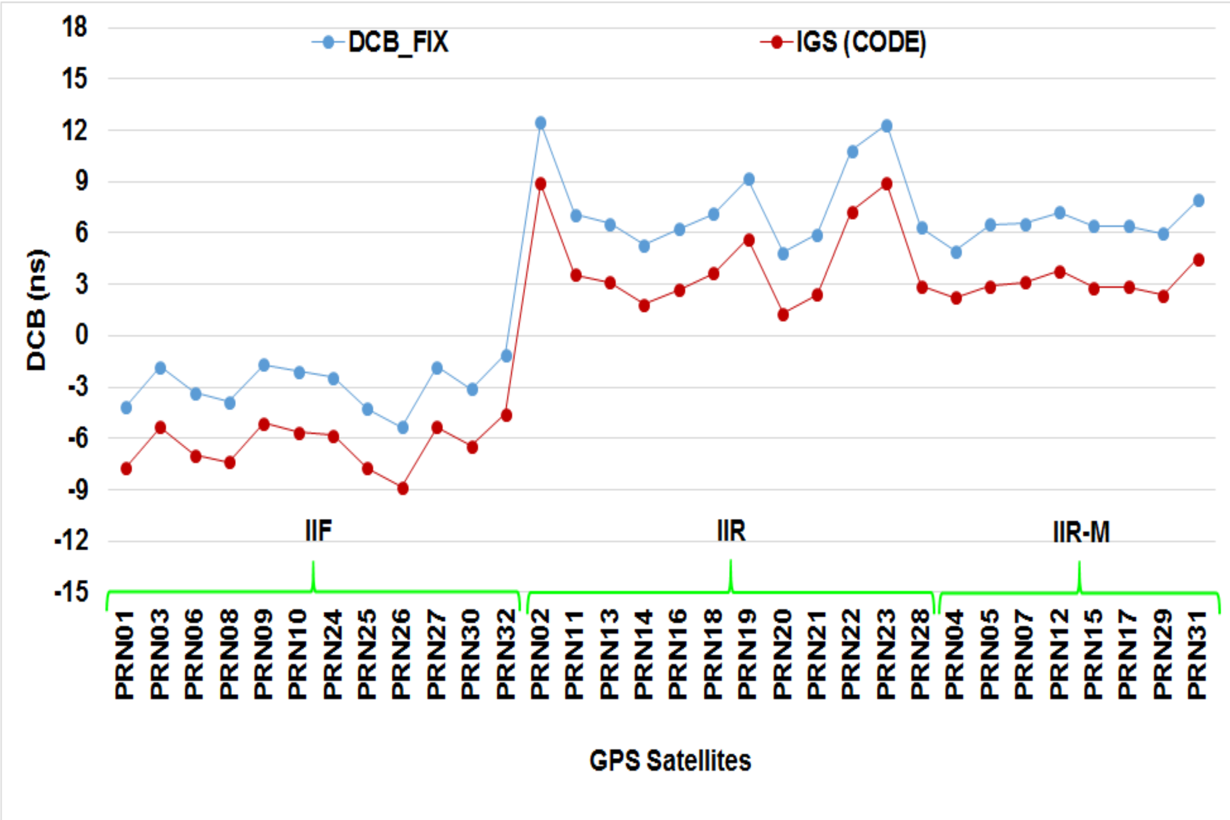

Fig. 7.1 Plot showing the average GPS satellite DCBs between P1 and P2 estimated by the DCB_FIX software (SEPT = – 4.41 ns) and IGS (CODE) over a period of 22 days (Mar 17 to Apr 7, 2016).

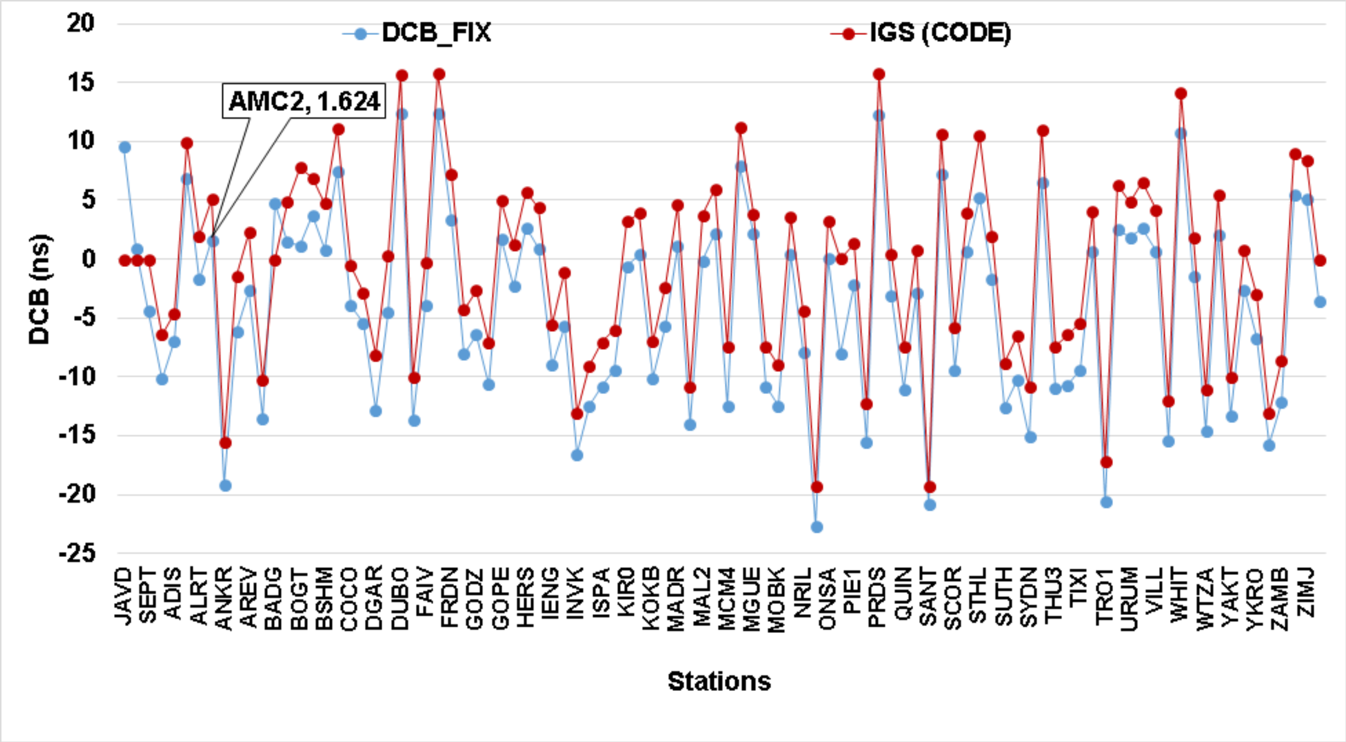

Fig. 7.2 Plot showing the average receiver DCBs between P1 and P2 estimated by the DCB_FIX software (SEPT = – 4.41 ns) and IGS (CODE) over a period of 22 days (Mar 17 to Apr 7, 2016).

true physical values. The more accurate the known DCB used to constrain the solution, the more accurate the estimated DCBs for the other receivers and satellites.

The DCB estimates for SEP2 and JAVD receiver systems from the DCB_FIX software and the DCB_ZM software are investigated in Table 7.1.

Table 7.1 DCB estimates of SEP2 and JAVD receiver systems from the simulator/antenna combination, DCB_FIX software and DCB_ZM Software (IGS)

Receiver System	**DCB P1-P2 Estimates (in ns)**		
	Receiver/Cable (GSS8000) + Antenna (Manufacturer)	**DCB_FIX**	**DCB_ZM**
SEP2	– 1.90 + 3 = **1.10**	**0.92** ± 0.27	4.40 ± 0.22
JAVD	6.83 + 3 = **9.83**	**9.60** ± 0.53	13.05 ± 0.6

Since the maximum DCB value of 3 ns for the Leica AR10 antenna has been used to compute the overall known DCB of the two receiver systems as discussed in Section 5.1.5 on antenna DCB, it is quite remarkable that the DCB_FIX software has been able to estimate the DCBs for the two receiver systems within few tenths of a nanosecond. The accuracy of the DCB estimated by the DCB_FIX is also independent of the fact that the SEP2 receiver is of a relatively higher quality in comparison to the geodetic grade JAVD receiver. When constrained by the zero-mean satellite DCB condition, the DCB_ZM software produces DCB estimates comparable to the IGS DCB solution and it can be seen from Table 7.1 that the latter are over estimated by about 3.5 ns. On the other hand, the satellite DCBs estimated by the IGS are underestimated by approximately the same amount when compared to those estimated by the DCB_FIX software.

It can also be seen from Figure 7.1 that the satellite DCBs for the newer generation of GPS block IIF satellites are lower than the previous generation of satellites. One possible explanation can be that with the advancement in technology, the newer satellites are better equipped in terms of quality of hardware to handle in-orbit temperatures and hence keep their DCBs to a minimum. The temperature sensitivity for signals transmitted by satellites in orbit is discussed in Coco et al. (1991).

7.1.1 **Stability of Estimated DCBs (GPS P1/P2 Only)**:

The LSQ processing was run on a daily basis and the unknowns that were estimated, comprises of ionospheric coefficients, one receiver DCB per station and one DCB per satellite. Using a 24-hour batch averaging, the average and standard deviation of the estimated DCBs was computed over a specified number of days. To investigate the stability of the estimated DCBs using the DCB_FIX software, the standard deviations of both the satellites and the receivers DCBs are plotted in Figures 7.3 and 7.4 respectively. The estimated DCBs are generally stable over time for both the satellites and the receivers. The average standard deviations of the estimated satellite and receiver DCBs are found to be 0.15 ns and 0.45 ns, respectively. Sudden jumps in standard deviations may indicate a possible replacement of the satellite or receiver or any part of the receiver system, such as antennas and cables. In some cases, it can also indicate potential hardware issues within the receiver or receiver architecture and this is revisited later in Section 7.8. These are however difficult to investigate because of the independent working of the IGS and MGEX stations. In Figure 7.4, a peak can be observed in the standard deviation of 'PALV' receiver system DCB – this is because the receiver was changed on the 30 March 2016 as published in the station log file (https://igscb.jpl.nasa.gov/igscb/station/log/palv20160329.log) and the replacement receiver has a significantly different DCB. As receivers from the same brand have relatively similar DCBs, it can be difficult to identify their replacement based on the standard deviations alone.

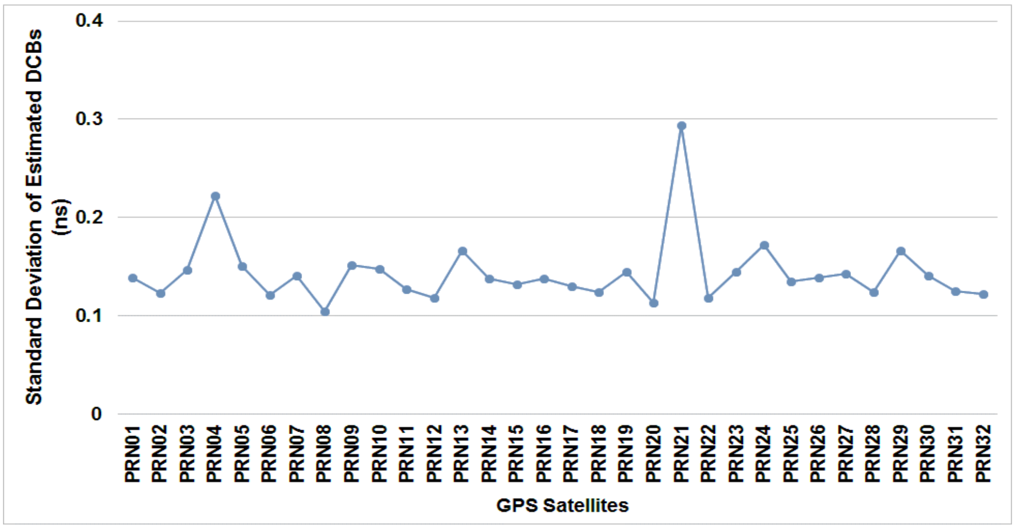

Fig. 7.3 Plot showing the standard deviations of the GPS satellites DCBs between P1 and P2 estimated by the DCB_FIX software over a period of 22 days (Network A – Mar 17 to Apr 7, 2016).

From the data processing with DCB_FIX or DCB_ZM software, the quality of the LSQ solution is analysed based on the a-posteriori unit variance, which is generally found to be independent of the external constraints, whether artificial or real. This indicates the constraints are so-called 'minimum' constraints, whose

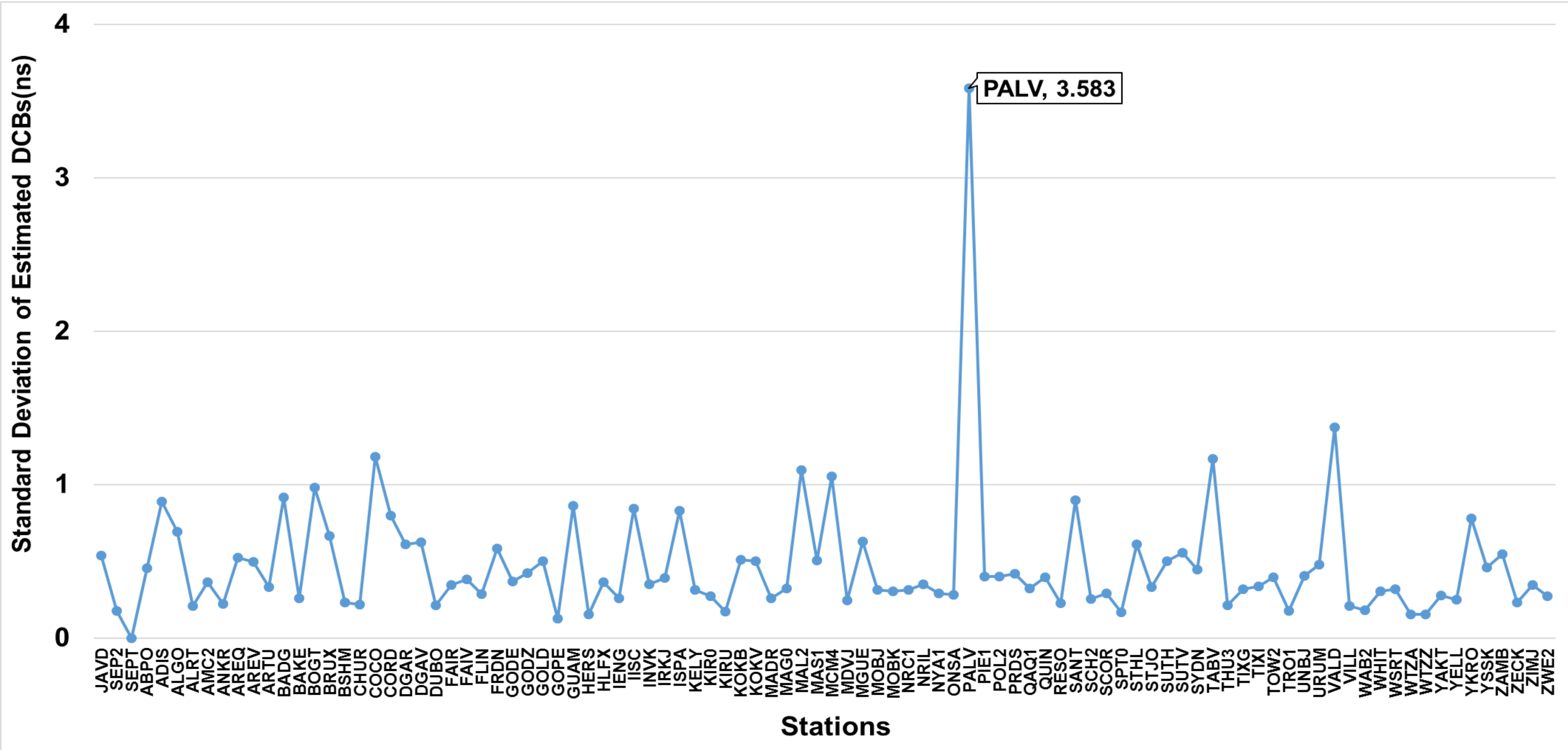

Fig. 7.4 Plot showing the standard deviations of the receivers DCBs between P1 and P2 as estimated by the DCB_FIX software over a period of 22 days (Network A – Mar 17 to Apr 7, 2016).

purpose is to resolve the rank deficiency only. The quality of the LSQ can be further analysed as part of future work by working with different ionospheric models and their impact on the estimated DCBs.

7.2 Estimated Satellites and Receivers DCBs using Network B of GPS L1/L2/L5 and Galileo E1/E5a Stations (Based on Uncalibrated GSS8000 Simulator):

Using the DCB_FIX software with the archived RINEX data of 39 and 41 stations (Network B) in the case of C1/P2, C1/C5 and E1/E5a (or C1C/C5Q) signal pairs, respectively, from 4 October 2016 up to 15 November 2016 (43 days) and a degree and order of 15 for the SH expansion, the processing was run on a day to day basis, constrained by the known DCB value of the respective signal combination for the SEPT receiver system. These values were estimated in simulation using the previously explained strategy as follows:

- C1 – P2 = 0.53 ns (i.e. – 1.67 – 2.7)
- C1 – C5 = – 3.67 ns (i.e. – 4.97 + 1.3)
- E1 – E5a = – 3.91 ns (i.e. – 5.21 + 1.3)

In terms of the estimated satellite and receiver DCBs, very similar results like the ones presented in Section 6.6 were found and for the sake of conciseness, these are not presented in full.

Table 7.2 compares, for 3 Galileo IOV (In Orbit Validation) satellites, the DCBs estimated using the DCB_FIX software with the manufacturer measured DCBs that have recently been published by ESA on its website (Galileo, 2016). The published values for IOVs are based on absolute calibration carried out on the ground against a payload verification system. Note that the DCBs derived from

B_{GD} for the three IOVs are included as a reference only against the ZM constraint.

Table 7.2 Comparison of Galileo IOV Satellite DCBs as estimated from the DCB_FIX Software with the ESA published manufacturer measured on the ground DCBs.

Galileo PRN	DCB E1-E5a Estimates (in ns)			
	ESA Published DCBs (I)	**DCB_FIX Software (II)**	**DCB derived from B_{GD}**	**Difference between (II) and (I)**
E11	9.71 ± 0.38	11.07 ± 0.52	16.62	1.36
E12	6.97 ± 0.41	8.80 ± 0.37	14.77	1.83
E19	2.15 ± 0.48	3.06 ± 0.29	8.12	0.91

It can be seen from Table 7.2 that the DCB estimates from the DCB_FIX software agree with the manufacturer measured on ground DCBs at the level of 1 to 2 ns. The results obtained by the DCB_FIX software are expected to improve further once the simulator DCB is accounted for in this processing strategy.

7.2.1 **Stability of Estimated DCBs**:

Similar to Section 7.1.1, the plots in Figures 7.5 to 7.10 are analysed to investigate the stability of the estimated satellite and receiver DCBs for C1/P2, C1/C5 and E1/E5a signal pairs. It can be seen from Figure 7.5 that the estimated satellite DCBs between C1 and P2 are fairly stable although the standard deviations are somewhat higher than the P1/P2 DCB estimates. This can however be explained by the codeless and semi-codeless tracking techniques that are frequently employed to derive P1 and P2 observations from the encrypted L1 and L2 signals, respectively. Because of the possible high correlation between P1 and P2, the resulting standard deviations can be lower in the P1/P2 combination than in any other combination involving the unencrypted signals. The standard deviations for the GPS C1 and C5 and the Galileo E1 and E5a are the highest out of all the combinations investigated but again these are found to be stable as shown in Figures 7.6 and 7.7. The worst case is the Galileo E24 satellite whose average DCB estimate for the E1 and E5a combination, over a period of 43 days, was found out to be –35.38 ns. Surprisingly, on DOY 291, the DCB estimate for this satellite between the same signal combination was found to be -1.78 ns. This DCB anomaly clearly indicates some possible problem with the on-board clocks or other hardware malfunction.

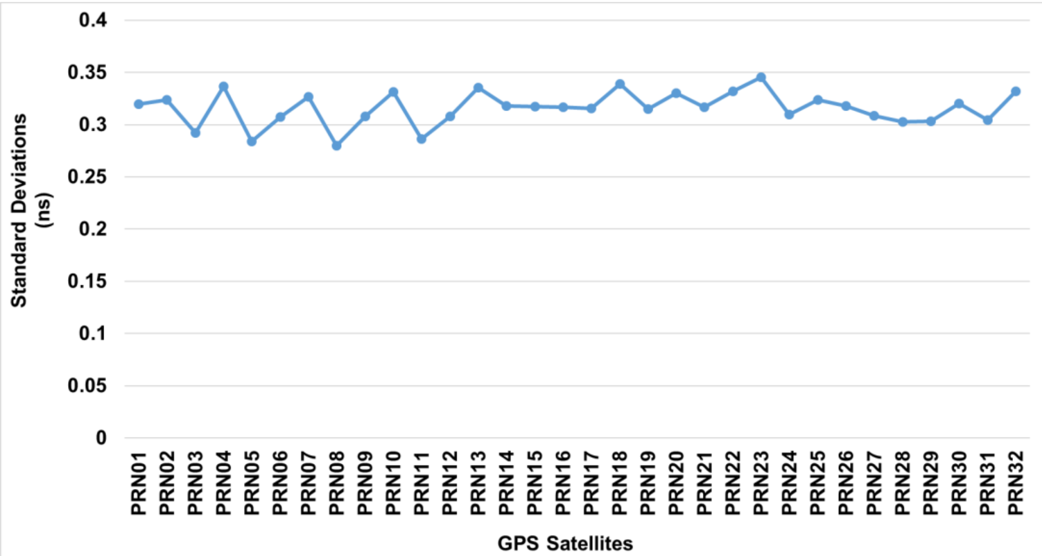

Fig. 7.5 Plot showing the standard deviations of the GPS satellites DCBs between C1 and P2 estimated by the DCB_FIX software over a period of 43 days (Network B – Oct 4 to Nov 15, 2016).

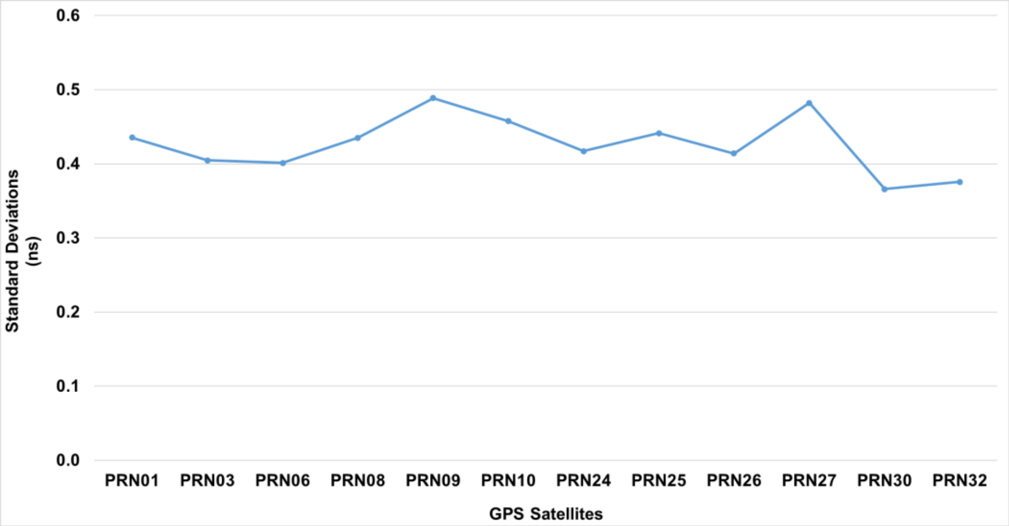

Fig. 7.6 Plot showing the standard deviations of the GPS satellites DCBs between C1 and C5 estimated by the DCB_FIX software over a period of 43 days (Network B – Oct 4 to Nov 15, 2016).

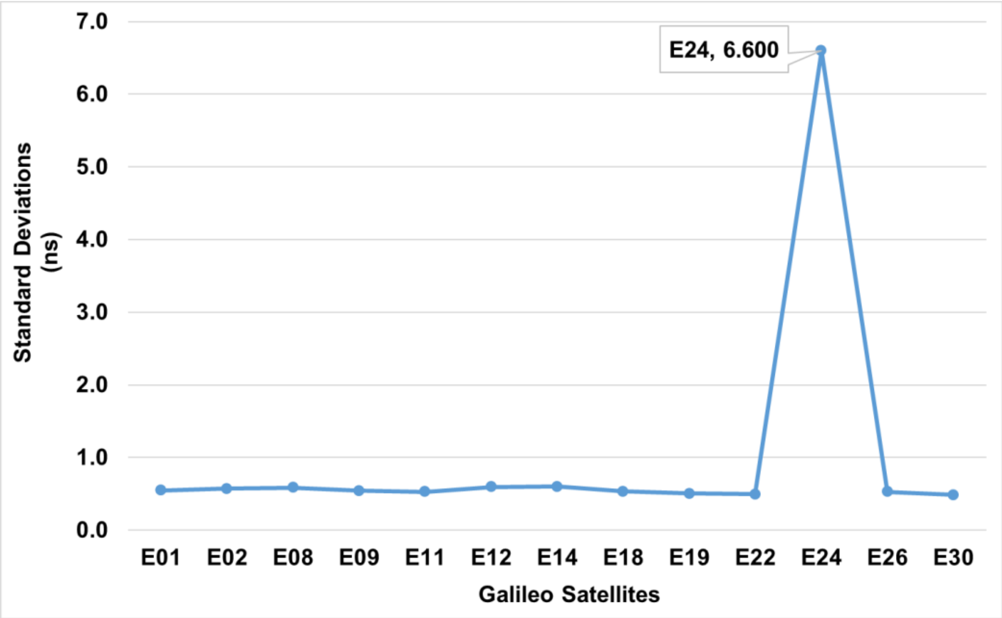

Fig. 7.7 Plot showing the standard deviations of the Galileo satellites DCBs between E1 and E5a estimated by the DCB_FIX software over a period of 43 days (Network B – Oct 4 to Nov 15, 2016).

Figures 7.8 to 7.10 show that the stability of the receiver DCB estimates is rather poor for the newer signals as opposed to the legacy signals. The stations with abnormally higher standard deviations were investigated against the impact of the ionospheric activity by plotting the DCB estimates and the Ap indices over a period of 43 days, as shown in Figures 7.11 to 7.13. As such, no correlation was found to exist between the estimated DCBs and the state of the ionosphere. A possible explanation for these abnormalities and relatively higher standard deviations is that the hardware technology that is currently in place to transmit and process these newer signals is still under a test phase and is in the process of refinement. It will take some time for them to reach the level of the legacy signals.

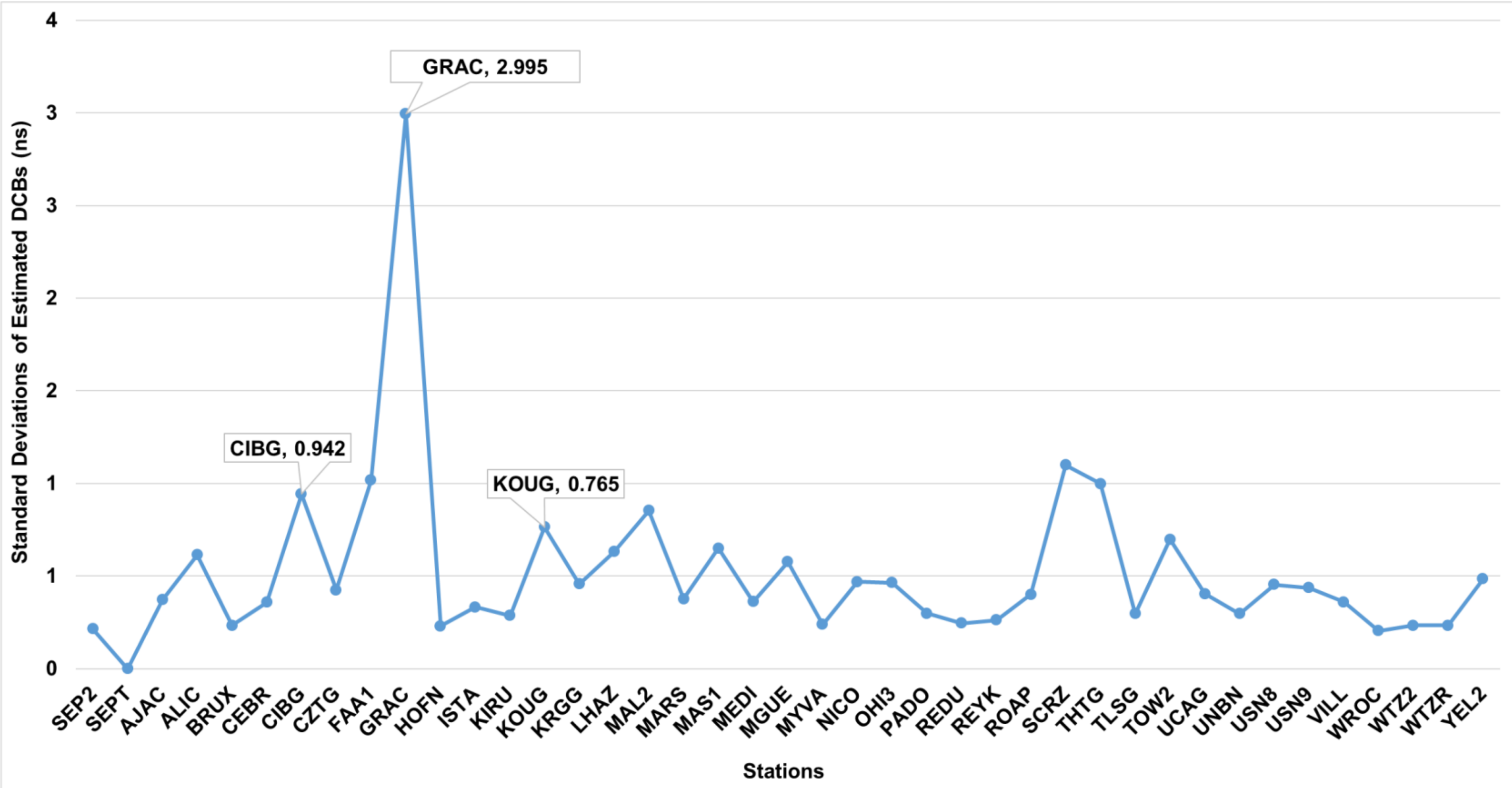

Fig. 7.8 Plot showing the standard deviations of the receivers DCBs between C1 and P2 as estimated by the DCB_FIX software over a period of 43 days (Network B – Oct 4 to Nov 15, 2016).

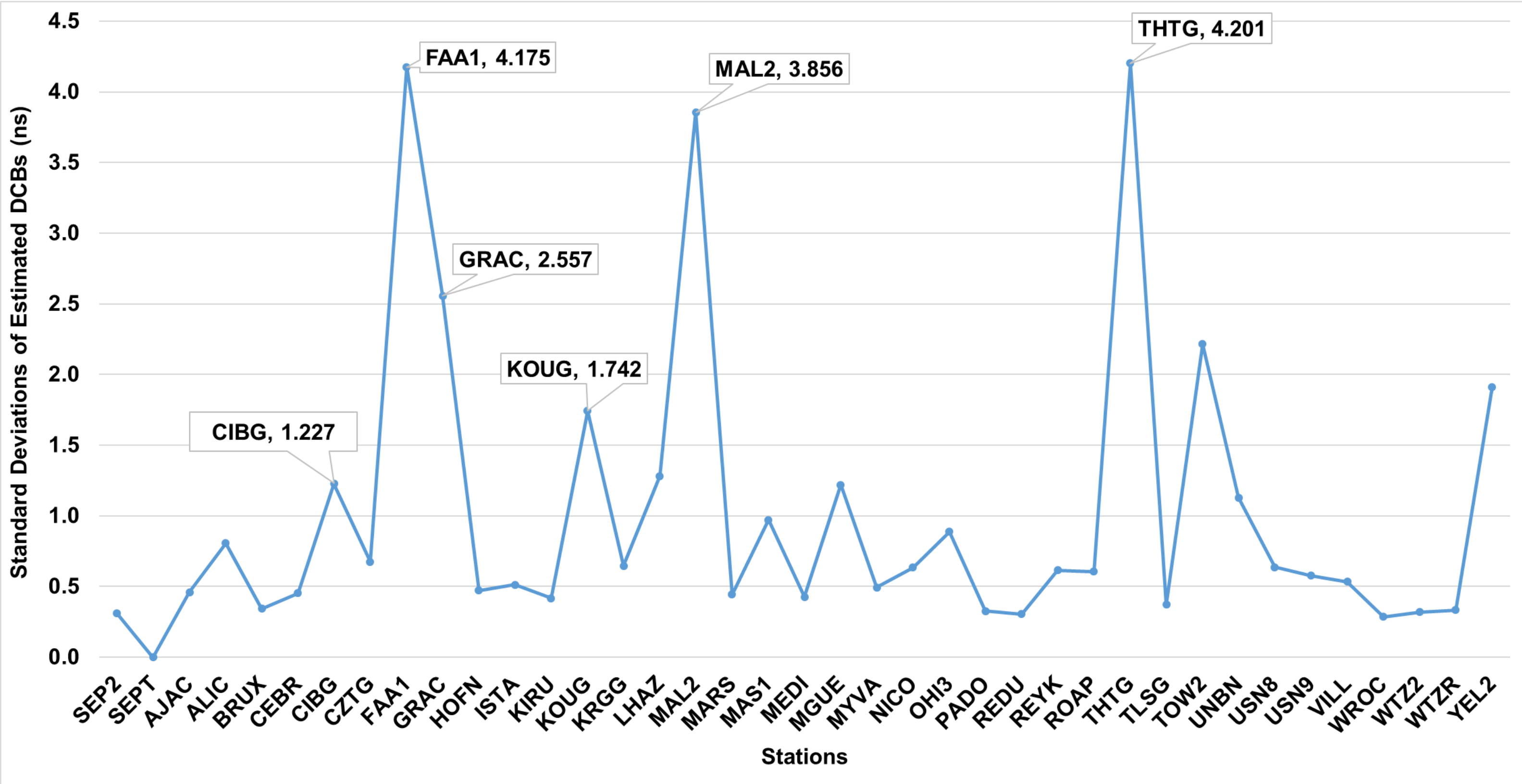

Fig. 7.9 Plot showing the standard deviations of the receivers DCBs between C1 and C5 as estimated by the DCB_FIX software over a period of 43 days (Network B – Oct 4 to Nov 15, 2016).

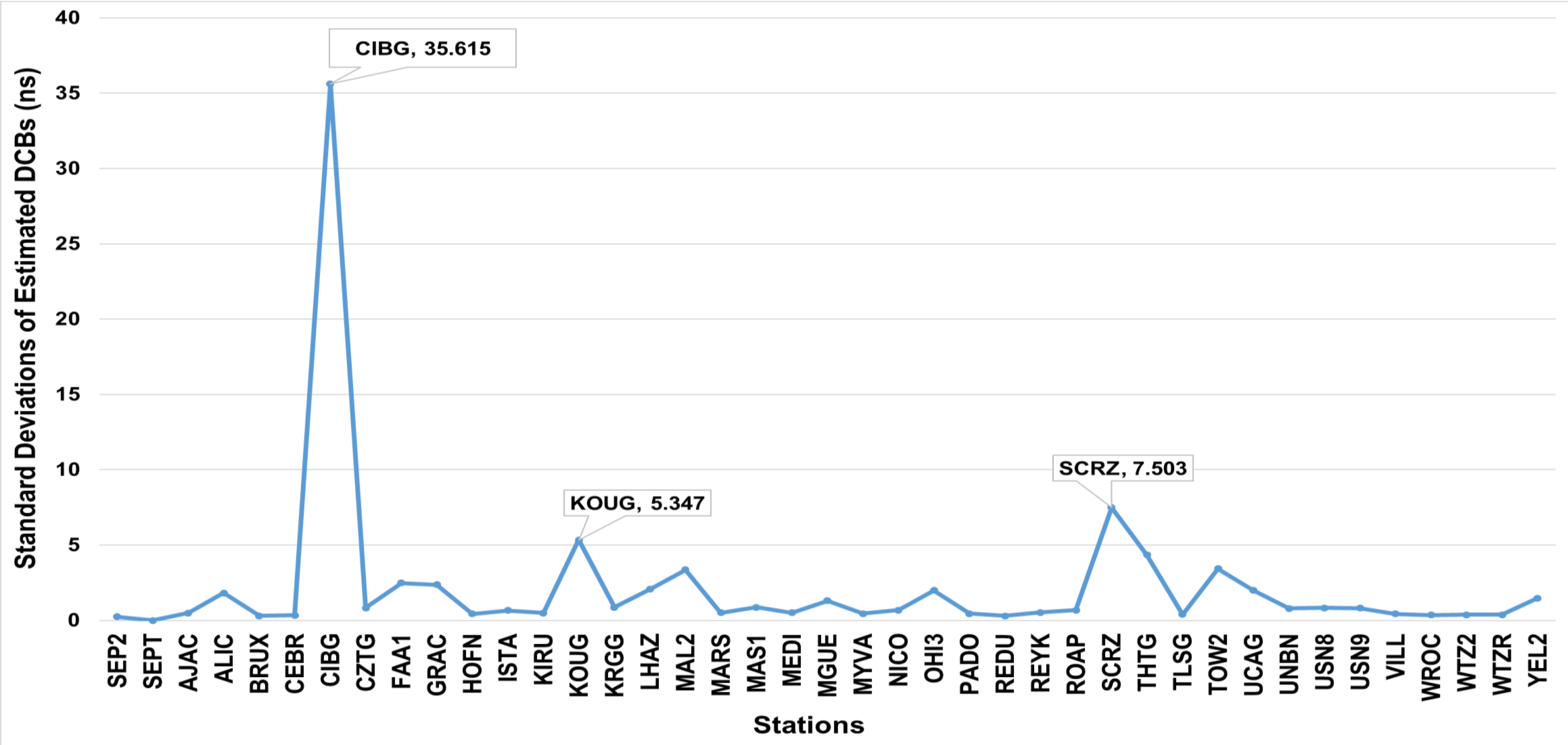

Fig. 7.10 Plot showing the standard deviations of the receivers DCBs between E1 and E5a as estimated by the DCB_FIX software over a period of 43 days (Network B – Oct 4 to Nov 15, 2016).

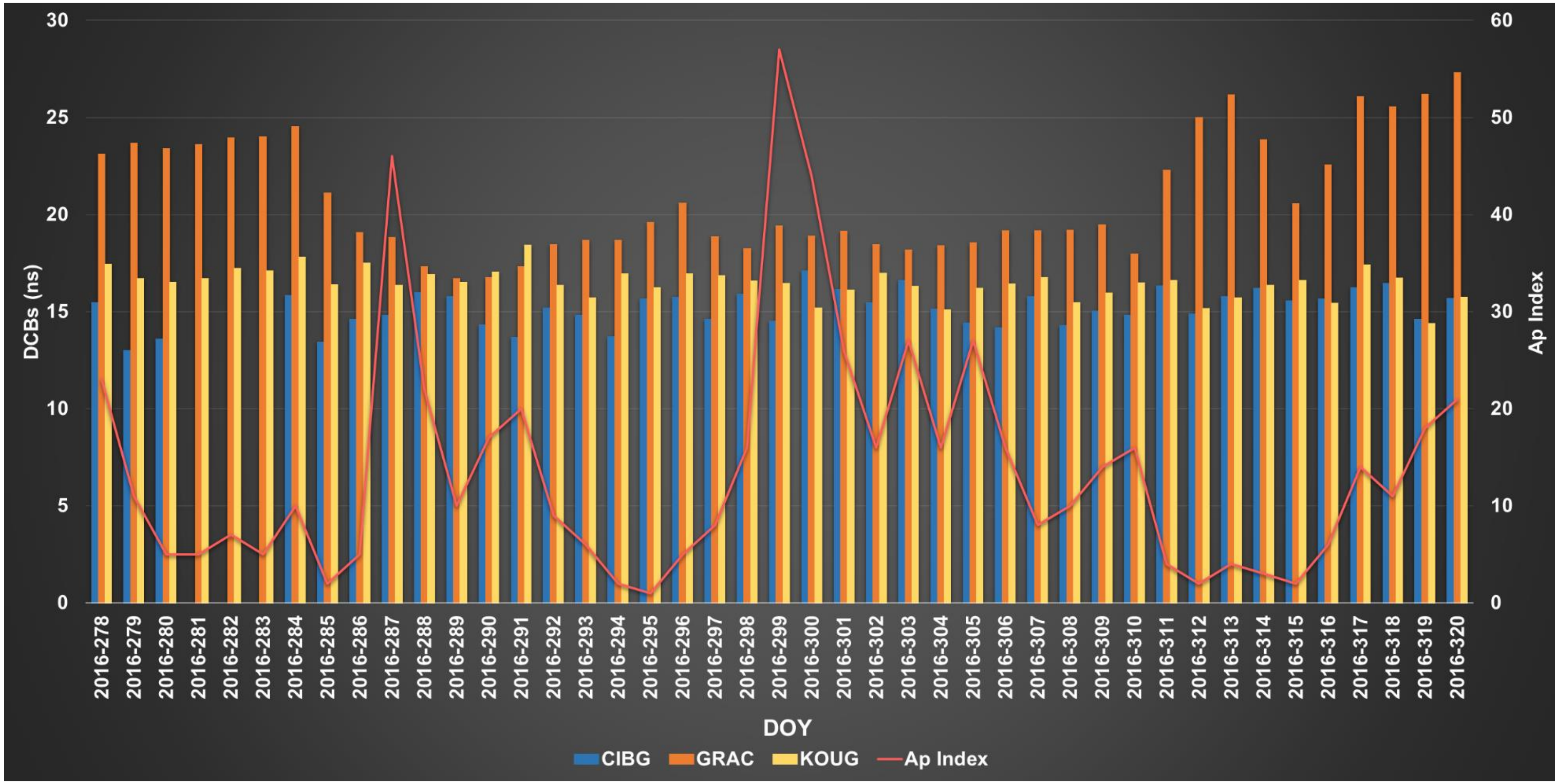

Fig. 7.11 Plot showing the daily DCB estimate of four different stations between GPS C1 and P2 as estimated by the DCB_FIX software and the Ap indices over a period of 43 days (Network B – Oct 4 to Nov 15, 2016).

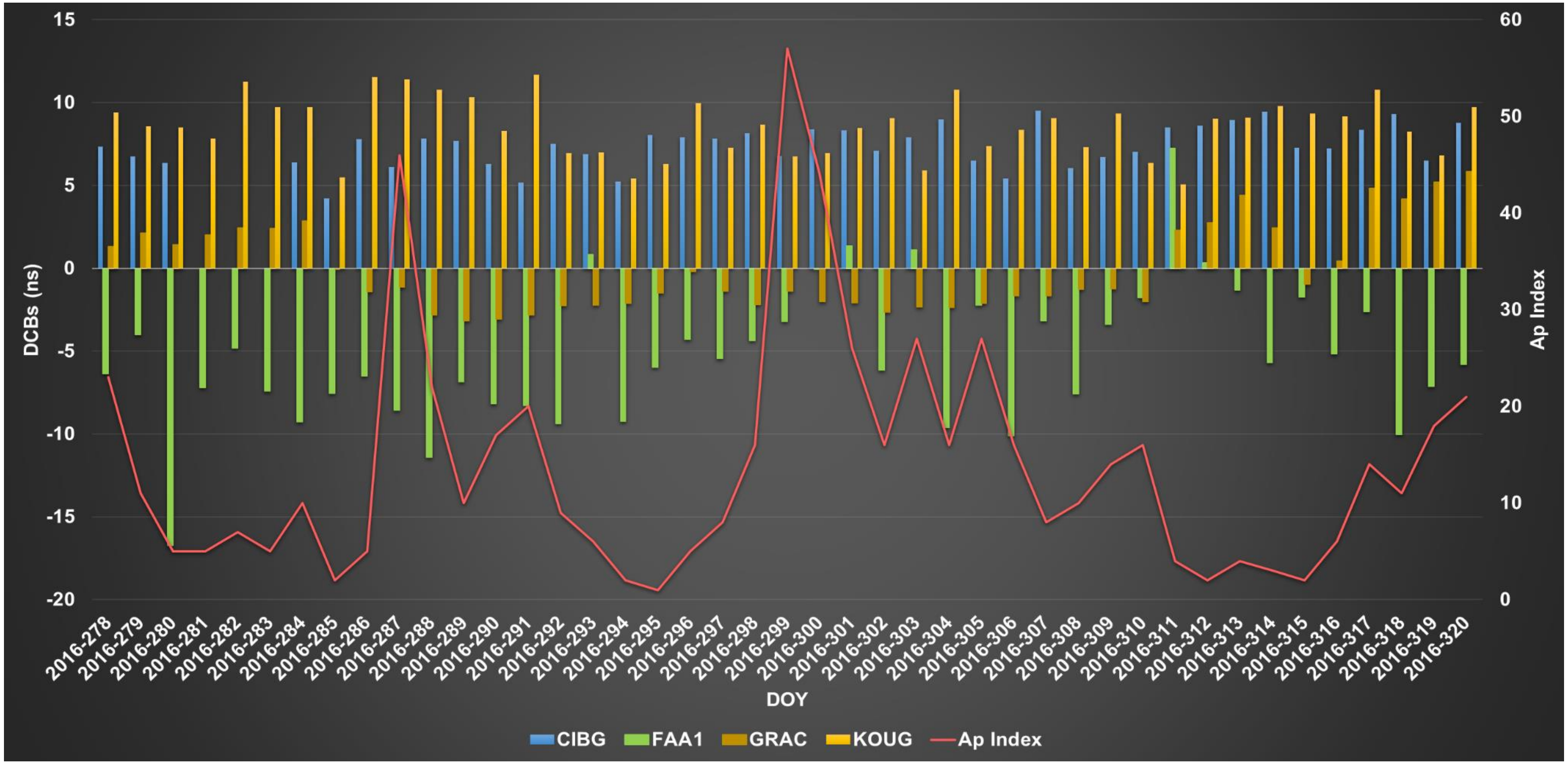

Fig. 7.12 Plot showing the daily DCB estimate of four different stations between GPS C1 and C5 as estimated by the DCB_FIX software and the Ap indices over a period of 43 days (Network B – Oct 4 to Nov 15, 2016).

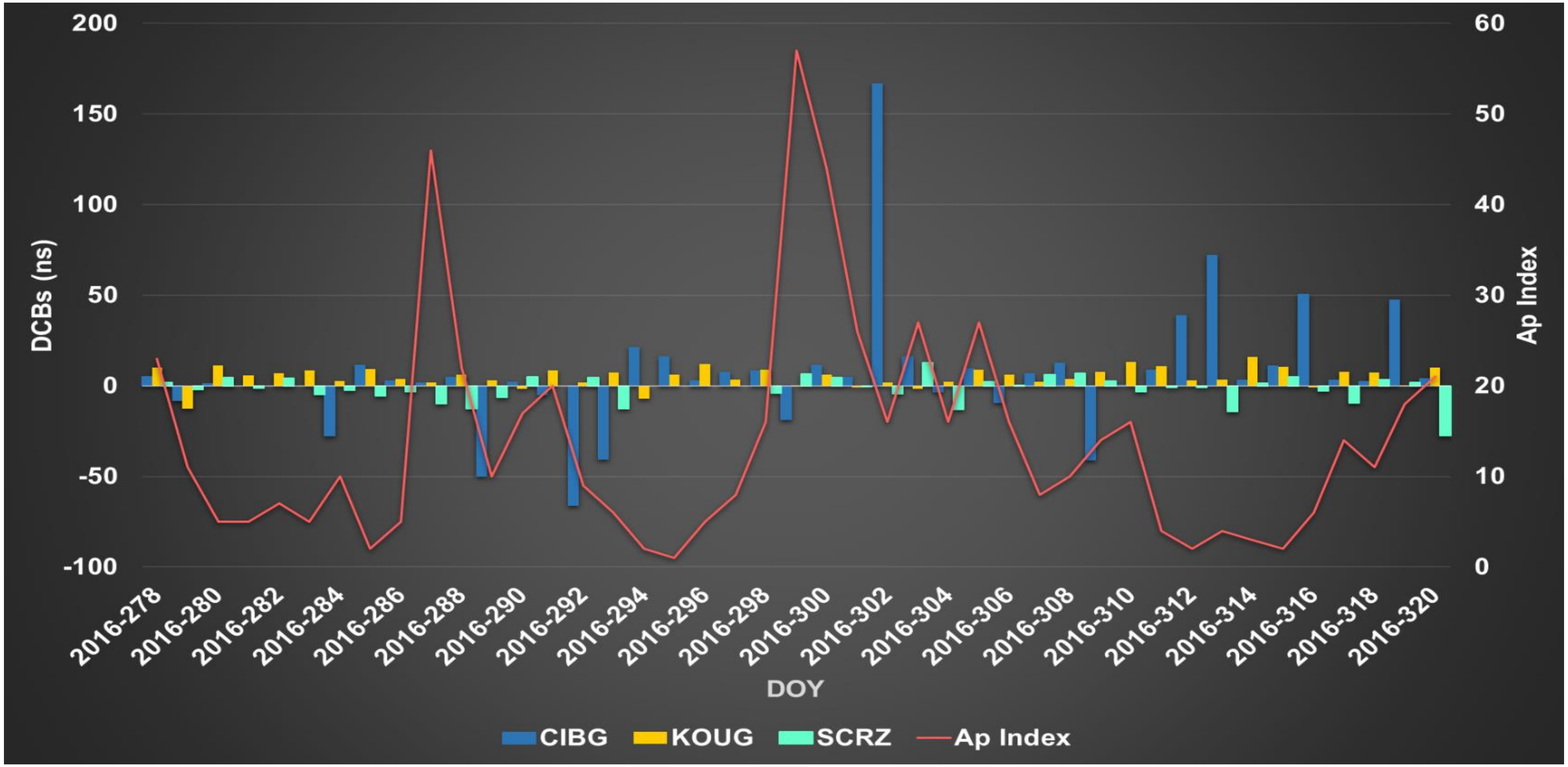

Fig. 7.13 Plot showing the daily DCB estimate of three different stations between Galileo between E1 and E5a as estimated by the DCB_FIX software and the Ap indices over a period of 43 days (Network B – Oct 4 to Nov 15, 2016).

7.3 Estimated STEC using different Calibration Strategies (Based on Uncalibrated GSS8000 Simulator and GPS P1/P2 only):

Based on equation (3.16) and using daily RINEX datasets, the STEC is estimated for different co-located receivers in the network, with the purpose of comparing the different STEC estimation strategies. To reiterate, the uncalibrated STEC refers to the case where no DCBs were applied and the calibrated STEC refers to the case where either IGS published DCBs or DCB_FIX estimated DCBs were applied.

Figure 7.14 shows the STEC plots constructed on the basis of different calibration strategies for PRN 24, as observed by the three NGI receivers, i.e. SEPT, SEP2 and JAVD, on the ionospherically quiet day of Mar 26, 2016 (Ap index of 2: ftp://ftp.gfz-potsdam.de/pub/home/obs/kp-ap/tab/kp1603.tab). Note that all three receivers were connected separately to three different antennas and were operating under the default tracking parameters, as presented in Table 5.2. The improvement and consistency in the estimated STEC as observed by three different receivers can be clearly seen from these plots between uncalibrated and calibrated solutions. It is also apparent that if receiver and satellite DCBs can be properly estimated, the geodetic grade receiver, the Javad Triumph–1, can also be used to generate almost similar STEC to the highly specialized ISMRs such as SEPT and SEP2. Here, one minor concern would be the increased noise level in the JAVD's TEC measurements even after the application of smoothing. However, as previously stated, a fair comparison would only be possible by using a consistent set of tracking parameters for all three receivers.

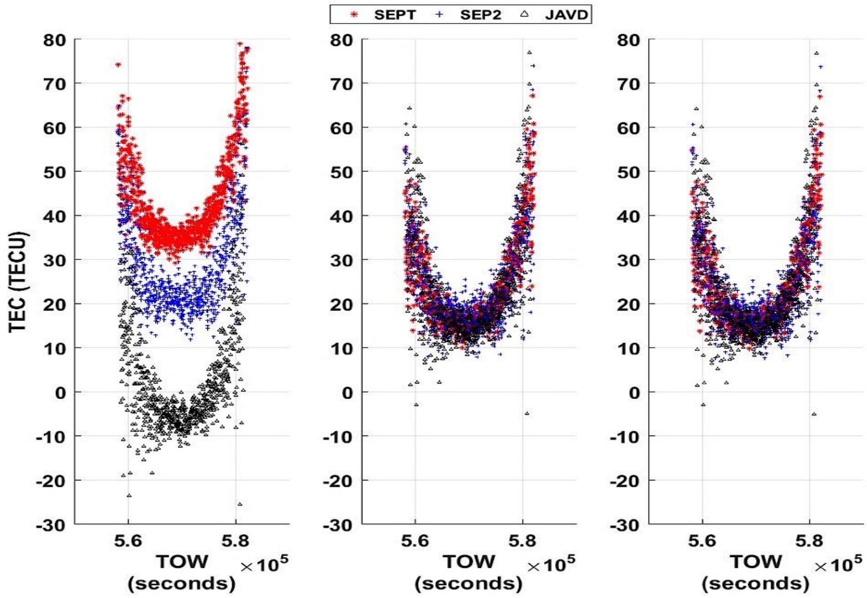

Fig. 7.14 Uncalibrated (Left), IGS or DCB_ZM Calibrated (Center) and DCB_FIX Calibrated (Right) STEC plots for PRN 24 as observed by SEPT, SEP2 and JAVD receiver systems (Mar 26, 2016)

From Figure 7.14, it can also be observed that there is a good agreement between IGS (or DCB_ZM) calibrated and DCB_FIX calibrated STEC plots. This demonstrates that for all practical purposes of ionospheric modelling, using the 'known' receiver DCB as an external constraint in comparison to the IGS strategy, represents a perfectly valid way of resolving the rank deficiency problem.

7.4 Estimated STEC using different Calibration Strategies (Based on Uncalibrated GSS8000 Simulator and GPS C1/P2, GPS C1/C5 and Galileo E1/E5a):

Based on equations (3.16) and (3.17), and using daily RINEX datasets, the STEC is estimated for different co-located receivers in the network, with the purpose of comparing the different STEC estimation strategies. Unlike network A, there were not many co-located stations in network B. Again, the uncalibrated STEC refers to the case where no DCBs were applied and the DCB FIX calibrated STEC refers to the case where DCB estimates from the DCB FIX processing were applied.

Figure 7.15 shows the STEC plots constructed on the basis of different calibration strategies for GPS PRN 1 and Galileo PRN 8, as observed by the two available NGI receivers, i.e. SEPT and SEP2, on the ionospherically quiet day of October 11, 2016 (Ap index of 2: ftp://ftp.gfz-potsdam.de/pub/home/obs/kp-ap/tab/kp1610.tab). Note that both the receivers are connected separately to two different antennas and were operating under the default tracking parameters, as presented in Table 5.2. Considering that both SEPT and SEP2 are highly specialised Septentrio receivers, the improvement in the estimated STEC is not as visible as when the Javad receiver is brought into the comparison.

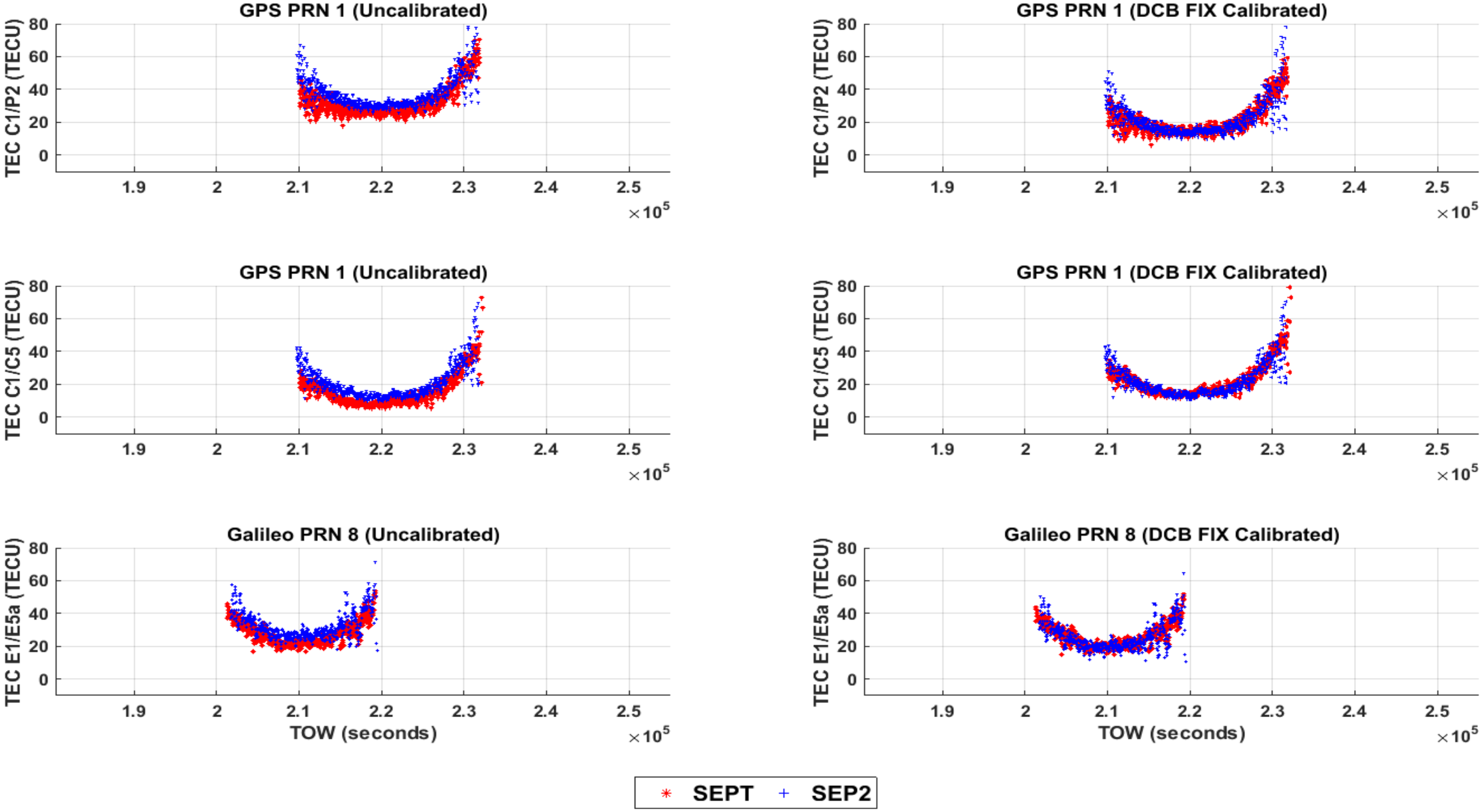

Fig. 7.15 Uncalibrated (Left) and DCB_FIX Calibrated (Right) STEC plots for GPS PRN 24 and Galileo PRN 8 as observed by SEPT and SEP2 receiver systems (Oct 11, 2016)

7.5 Estimation of Simulator DCB: Network Based Approach (For GPS P1/P2 Only):

To avoid relying on the in-lab calibration, a strategy was devised to estimate the contribution of the simulator in the DCB estimation by involving the IGS AMC2 station. From the log file of AMC2 station (https://igscb.jpl.nasa.gov/igscb/station/log/amc2_20140915.log), it can be seen that the individual hardware delays existing between different components of the system such as antenna, antenna cable, antenna splitter, receiver, etc. have already been measured and applied to the raw code based pseudoranges. Although not knowing exactly how these individual delays are measured, it is considered here that the measurements are made accurately enough. Based on that assumption, one can expect to get a DCB value close to 0 for this station when estimating DCBs using a ‘known’ receiver DCB, provided that the ionosphere has been correctly modelled. As shown in Figure 7.2, by using the DCB_FIX software, a mean DCB value of +1.62 ns was estimated for this station, implying therefore that despite some uncertainty, this can be interpreted to represent the DCB between GPS P1 and P2 signals of the simulator itself. Hence, it can be inferred that the simulator DCB for a certain signal combination can be measured by exploiting the proposed strategy in conjunction with an available station receiver with accurately known hardware delays and this would further push the estimated DCBs toward their physical values. Unfortunately, no such receiver with known hardware delays was available for the other signal combinations.

7.6 Estimation of Simulator DCB: Relative Calibration Approach (For all available signal pairs):

The DCB estimates of the SEPT receiver for different signal combinations corrupted by the DCBs of the simulator i.e. GSS8000 have been presented and discussed in Section 6.4. Working with the GSS9000 simulator, the actual DCBs (i.e. the ones that are corrected for simulator DCBs) of the SEPT receiver for different signal combinations have been presented in Table 6.5. Apart from the simulator, another discrepancy between these DCB estimates is that the estimated DCBs from the GSS8000 simulator involved a 20-meter cable, whereas, the ones from the GSS9000 simulator are based on a 1-meter cable. From Table 6.6, it has already been established that the effect coming from the cable is very small and can be assumed as negligible. Hence, the DCB values for the NGI's GSS8000 can be computed by subtracting the actual DCBs of the SEPT receiver as presented in Table 6.5 from the corrupted ones as presented in Section 6.4. Table 7.3 gives the DCBs of the NGI's GSS8000 simulator. The higher quality of the Galileo signal generator of the GSS8000 simulator is evident from the low DCB value between E1 and E5a. This can be justified on the basis that since purchase, the GPS signal generator has been more rigorously used by the NGI researchers and hence, it has undergone more wear and tear internally. On the other hand, the Galileo signal generator being linked with an emerging new constellation, has not been used that frequently by the researchers at NGI. One must remember that the GPS and Galileo signal generators are completely independent signal generator units and as such, they cannot undergo similar degradation over their operational lives.

Table 7.3 Estimated DCBs of NGI's GSS8000 hardware signal simulator

Signal Combination	DCB (ns)
P1 – P2	– 0.42
C1 – P1	0.01
C1 – P2	– 0.41
C1 – C5	– 0.31
E1 – E5a	– 0.08

The DCB values of NGI's GSS8000 simulator given in Table 7.3 are also compared with the DCB estimates that were derived for the same simulator on the basis of original calibration at the time of purchase and given in Table 5.1. It can be seen that the DCB between the L1 (P1) and L2 (P2) pair is almost similar in magnitude but opposite in sign. If the original calibration values for the simulator are to be trusted then this means that the P2 pseudorange that was initially lagging behind the P1 pseudorange, is now leading the P1 pseudorange by almost a similar amount. In the case of L1 (C1) and L5 (C5), the initial delay was 0 and that is, they were being generated at the very same instant but now, the C5 pseudorange is leading the C1 pseudorange. In the case of Galileo E1 and E5a signal pair, there is only a minor difference between the old and current calibration value.

An important point to highlight here is that the relative calibration will only be as good as the absolute calibration of the first simulator (GSS9000 in this case) that has been done initially to start the relative calibration procedure.

7.7 Estimated Satellites and Receivers DCBs (Based on Calibrated Simulators):

Using the DCB_FIX software separately with the archived RINEX data of Network A (22 days) and of Network B (43 days), respectively, and the SH expansion of degree and order 15 in both the cases, all the LSQ data processing was re-run on a day to day basis with the solution constrained to the known DCB values of the SEPT receiver system, corrected for the simulator DCBs. These corrected DCBs were specified earlier in Table 6.5. The results obtained were very similar to the results presented in the earlier sections, and that is why these are not presented here. However, the important deductions derived from this re-processing are as follows:

- In the case of Galileo E1 and E5a signals, as the quality of the signal generator is very good as shown by the small DCB value (Table 7.3), the DCB estimates of the IOV satellites have shown a very small improvement, in the order of 0.02 – 0.04 ns in comparison to the manufacturer measured on ground DCBs (Table 7.2). However, in the case of the GPS P1/P2, C1/P2 and C1/C5 signal pairs, there seems to be some improvement because of the slightly higher simulator DCBs (Table 7.3). However, as there is no external reference available, it was not possible to do any comparative analysis of the estimated DCBs.
- With reference to the network-based simulator calibration approach described in Section 6.11, a DCB value of 2.05 ± 0.61 ns was estimated for the AMC2 station instead of 1.62 ± 0.49 ns, while working with the corrected GPS P1/P2 DCB of the SEPT receiver. This is significantly different from the actual

simulator DCB between P1 and P2 presented in Table 6.10 on the basis of relative calibration. The unexpectedly higher DCB estimate of the AMC2 station along with a standard deviation of almost half a nanosecond show that although principally true, the network-based approach is not proving to be a good indicator of the simulator DCB. Two possible explanations for this inadequacy could be the inherent inefficiency of the ionospheric model to accurately represent the ionospheric activity or the probable low accuracy of the procedure that was followed at the AMC2 station to calibrate all the hardware delays. Another aspect that could be problematic is the behaviour of the receiver DCB itself. Although the DCBs are considered stable over relatively long periods of time, the standard deviation of approximately 0.5 ns clearly shows that there is an inherent fluctuating trend associated with it. This was observed to be even higher in the case of other network stations and there is a need to study and investigate these DCBs by estimating them on a shorter interval rather than every 24 hours, which is the current norm. The argument presented here is strengthened in the next sub-section, describing the DCB anomalies that have been witnessed in this research without any reasonable explanation.

7.8 DCB Anomalies of IGS's SANT and VALD Stations:

During the estimation of satellite and receiver DCBs from the network of IGS stations, it has been observed that the station SANT, located in Santiago, Chile, has a relatively unstable DCB. To investigate this further, Figure 7.16 shows the IGS published DCB for the SANT station for the month of April 2016. Because of the unavailability of SEPT observation data for most of the days in April 2016, the DCB estimates from the DCB_FIX software have not been plotted. The fluctuations in the station DCB can be readily picked up from the figure with a maximum value of -19.96 ns and a minimum value of -3.82 ns. The average monthly DCB was found to be -13.13 ns with a high standard deviation of ± 4.76 ns. No change in the receiver and no problem in the hardware configuration were reported in the station log file. The behaviour of the SANT receiver in terms of stand-alone positioning and PPP was also investigated but nothing unusual was found in the positioning solutions. This can be explained on the basis that in the stand-alone positioning, the receiver DCB can be absorbed by the receiver clock offset, whereas in PPP, the DCBs cancel out once the ionospheric free (IF) observable is employed (see Section 3.7). Similarly, the DCBs also cancel out in the double difference positioning solution. As a last attempt, the estimated DCB for the SANT station was studied against the ionospheric activity but again, it was hard to find any specific correlation between the two, as shown in Figure 7.16.

Moving on to the second IGS station VALD, located in Val D'Or, Canada, it has been observed that after the replacement of a broken antenna cable under the heavy snowfall, the estimated DCB of that station dropped by almost 11 ns, turning negative, as shown in Figure 7.17 and then recovered to its past estimated value over a period of more than a week. This was an unexpected phenomenon and an investigation was carried out to study the estimated DCB against the temperature variation. However, nothing conclusive was observed to relate the mean temperature variation in that area with the estimated DCB of the VALD

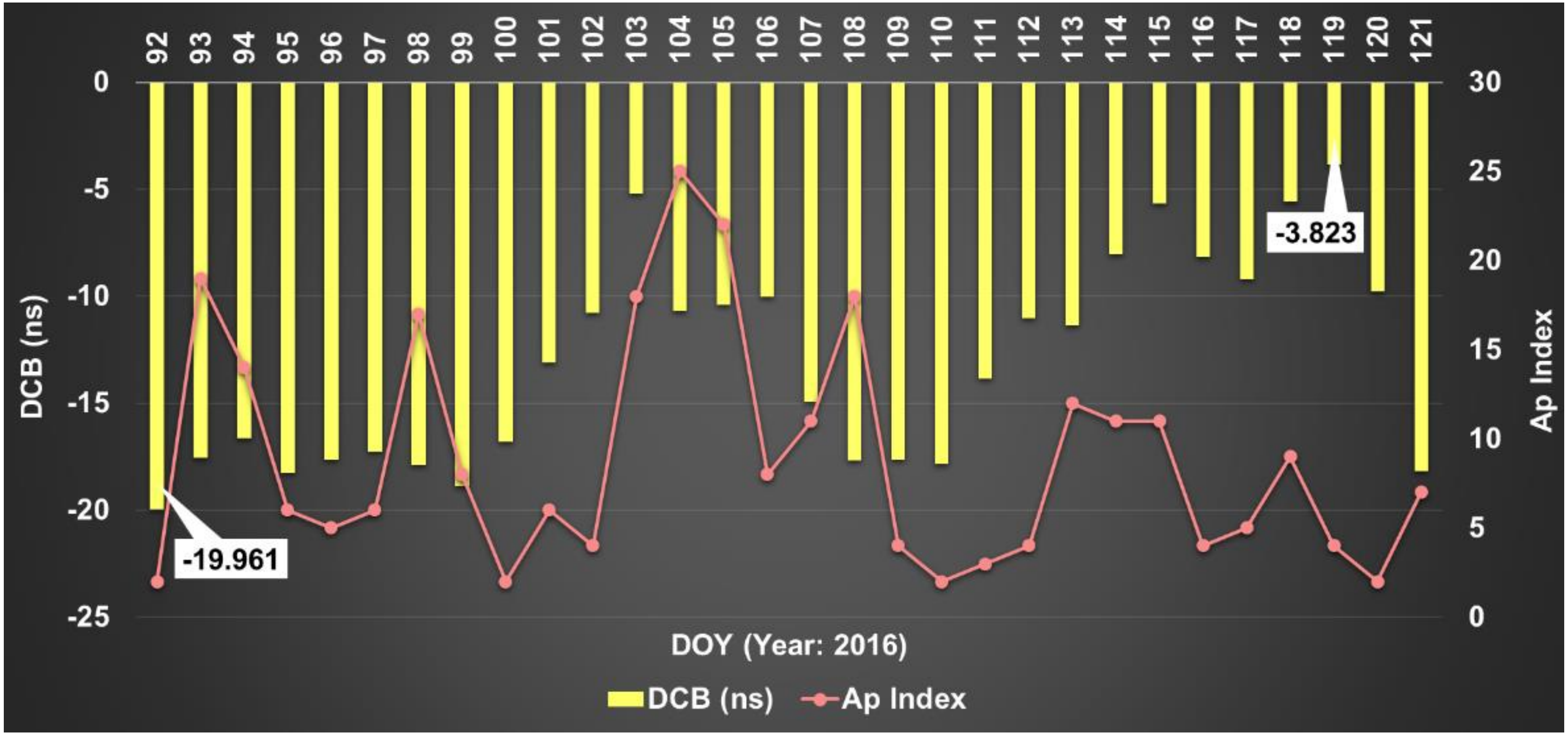

Fig. 7.16 Published DCB of the IGS SANT station between GPS P1 and P2 signals along with the Ap Indices for the month of April 2016.

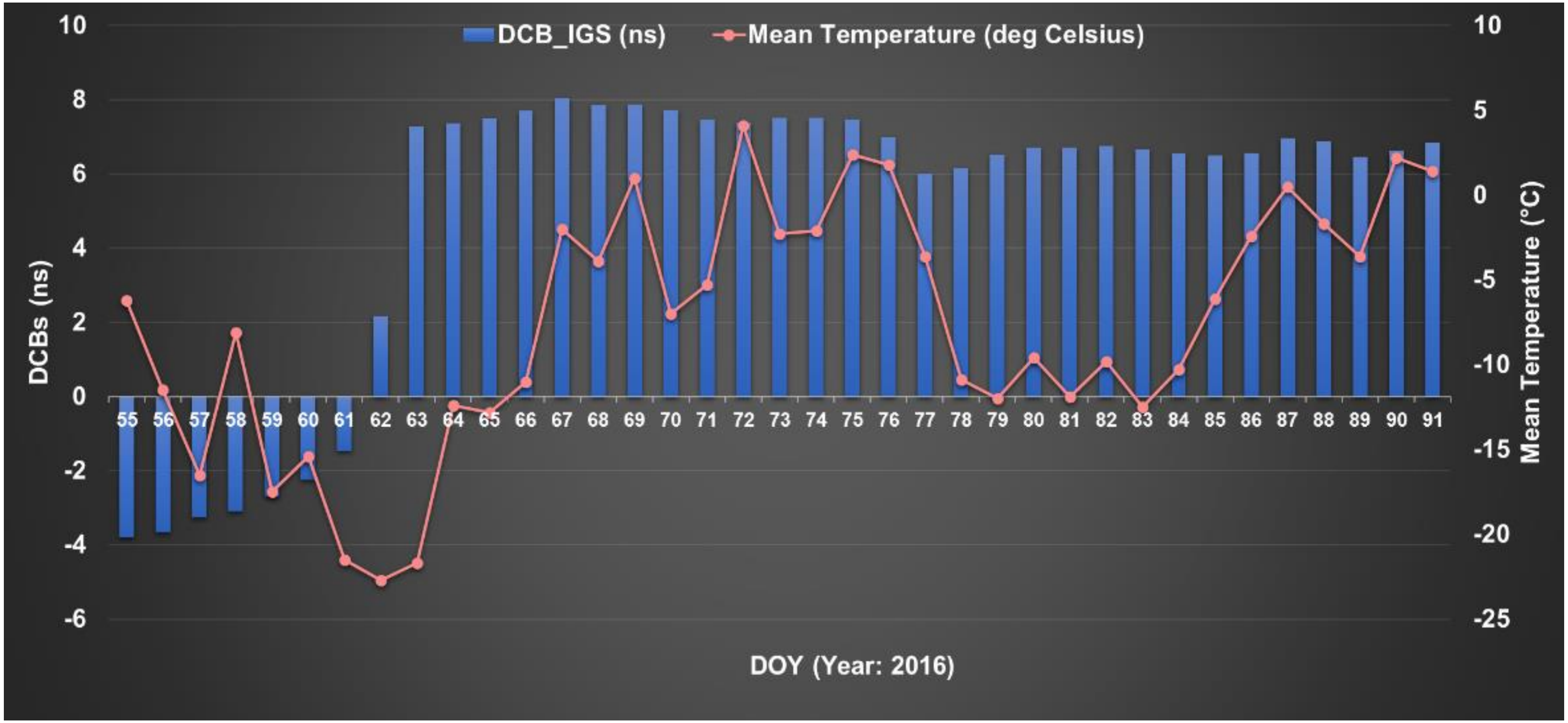

Fig. 7.17 Published DCB of the IGS VALD station between GPS P1 and P2 signals along with the mean temperature variation over a period of 37 days (Feb 24 to Mar 31, 2016).

station, as shown in Figure 7.17. The ionospheric activity was also found to be really quiet during these days

Looking at the behaviour of these above-mentioned stations, the sensitivity of the DCBs must be given due importance, especially in the case of ionospheric monitoring. Rather than using the monthly averages of the published DCBs, one must refer to daily estimated values of the receiver and satellite DCBs in STEC estimation. Also, it would be better to investigate the estimation of DCBs on shorter intervals rather than 24 hours to have a better picture of variations that can exist within the estimated DCBs.

7.9 Effect of Ionospheric Activity on DCBs' Estimation:

The impact of extreme vs quiet ionospheric activity on DCB estimation was studied during a period of 22 days i.e. 20 Oct to 11 Nov 2003. This period includes the famous Halloween Storm of 2003. Using the methodology already described for estimating terrestrial DCBs, the LSQ processing was run on a daily basis with varying degree and order of the SH expansion and by using the 56 available P1/P2 stations of Network A. As no station with 'known' receiver DCB was available, the ZM was used as an external constraint to resolve the rank deficiency and to separate the receiver DCBs from the satellite DCBs. Figure 7.18 shows the variation in the a-posteriori unit variance or the standard error of observation of the daily LSQ processing with varying degrees and orders of the SH expansion over the above specified period. It can be seen that by increasing the degree and order of the SH expansion, there is a decrease in the a-posteriori unit variance. On the other hand, the effect of increased ionospheric activity with the respective increase in the a-posteriori unit variance can also be clearly observed from the same figure. The DCBs are believed to play a dominant role in the LSQ processing as a very minor change in picoseconds is observed across the different degrees and orders of the SH expansion. As a side note, the primary effect was observed on the ionospheric coefficients, which were not studied in this research.

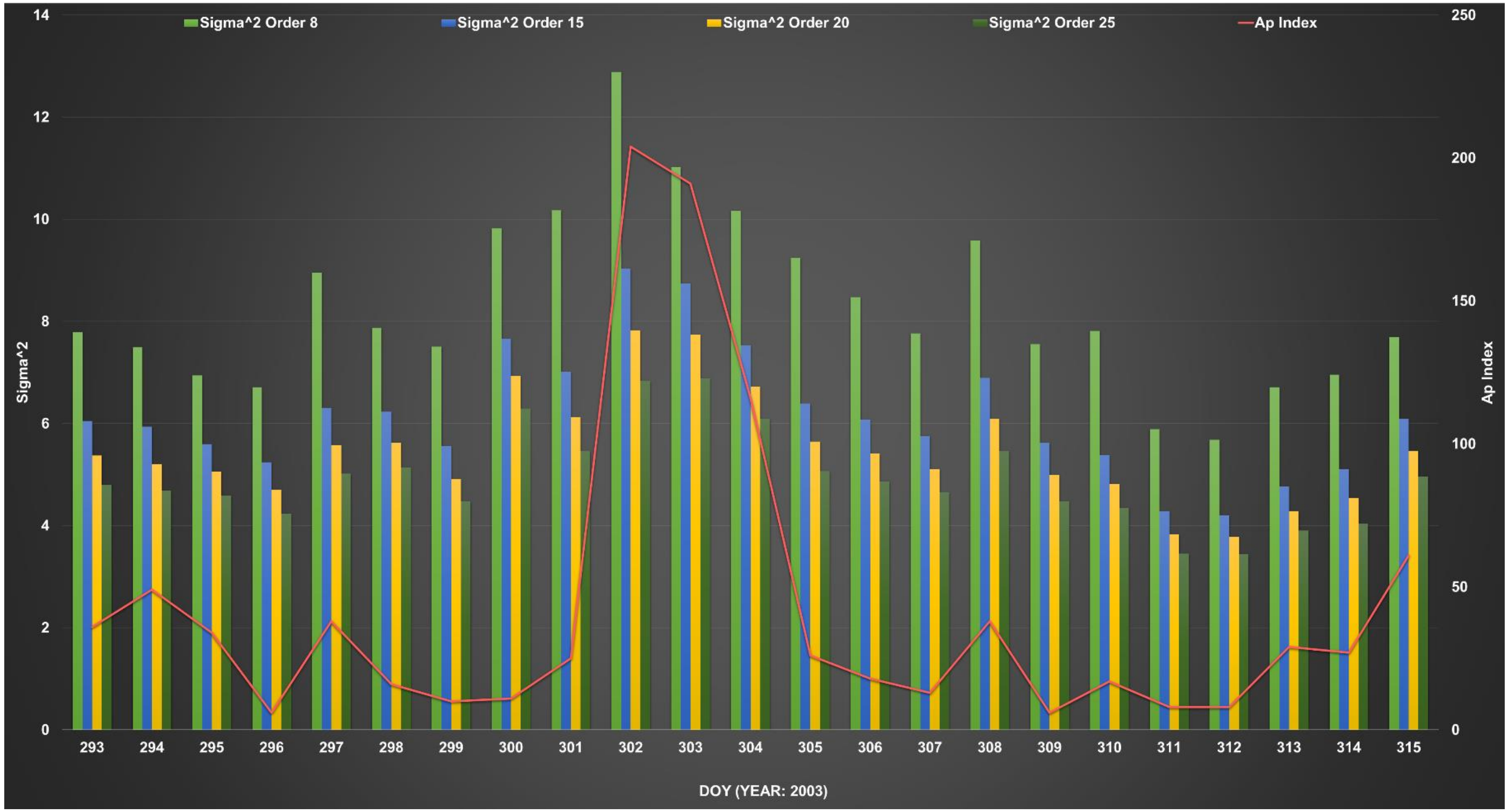

Fig. 7.18 Variation in a-posteriori unit variances of the LSQ processing (based on zero mean constraint) with varying degrees and orders of the SH expansion and the Ap Indices over a period of 22 days including the Halloween Storm (Oct 20 to Nov 11, 2016).

CHAPTER 8

CONCLUSIONS AND RECOMMENDATIONS FOR FUTURE WORK

8.1 Conclusions

The conclusions that have been drawn from this research are as follows:

1. The hardware signal simulator is an important component of this research and it must be regularly maintained and calibrated. Simulator calibration might not be an issue for differential GNSS processing but working with uncombined raw GNSS observations, the corresponding biases coming from the associated equipment need to be carefully estimated and accounted for. It has been clearly observed that with the blocked inlet air filters and the very high internal operating temperatures, variable delays were experienced by the signals propagating through different channel cards of the Spirent GSS8000 simulator. These initially gave the wrong impression of systematic biases existing between the simulator channels and considerable time was spent in trying to understand and analyse them. However, once the inlet air filters were washed and replaced, not only the internal operating temperatures decreased, but the channel alignment as recommended by Spirent and performed through the SimGEN™ software appeared to be more effective and produced more precise and consistent results. This is another case that the channel alignment at present only works for Galileo signal generator. The malfunctioning of the channel alignment utility in the case of GPS signal generator can be explained on the basis that the GPS signal generator has been more frequently used in simulations by different

research groups of NGI rather than the Galileo signal generator. As a result, it has undergone more wear and tear than the Galileo signal generator and as a consequence, the simulated GPS signals are too misaligned, and this misalignment is beyond the capability of the channel alignment utility to fix. It is believed that the calibration of the individual channel cards of the GSS8000 simulator can fix the misalignment issue and in turn the failure of the channel alignment utility. The Spirent GSS9000 hardware simulator is advantageous here as it allows calibration of all the signal banks through the ACU using an initial physical calibration of only one channel bank.

2. As per Montenbruck (2014), the DCB products generated by IGS lack self-consistency i.e. DCB(a-b) + DCB(b-c) $\neq$ DCB(a-c) where a, b & c represent three different individual code delays. In this research, it has been found that a hardware signal simulator such as the Spirent GSS8000 can be used effectively to estimate a consistent and more realistic set of DCBs between different signal pairs for any multi frequency, multi constellation receiver. The improvement in the proposed technique with the use of a calibrated simulator was not prominent because of two primary reasons. The first one is the lack of availability of reference GPS satellite DCBs already measured on the ground by the manufacturer. The second reason is that the Galileo signal generator of NGI's GSS8000 simulator is still satisfactorily calibrated and the channel alignment utility is working really well with it. As a consequence, while working with good quality and precise Galileo signals, very minor improvement was observed in the DCB estimates.

3. The receiver DCB is often mistaken as a function of the receiver hardware only. This is especially not true because in an open sky situation, the receiver DCB refers to the DCB of the entire 'system' comprising of antenna, cable and the receiver itself. Therefore, it should be ensured that if a particular receiver DCB is to be used to estimate the satellites and receivers DCBs in a regional or global network, the DCB of the whole system is used to constrain the solution, otherwise one can expect variations in the estimated DCBs with the changing system components such as antenna, cable, splitter, etc. Accordingly, it is important to note that the DCBs estimated by the IGS/MGEX represent the DCB of the entire receiver system.

4. A good agreement was found to exist between the estimated DCBs for both the SEPT and SEP2 receivers and the nominal DCBs as supplied by the manufacturer. This clearly demonstrates that the proposed technique of estimating receiver DCBs using simulated signals represents an effective way for estimating the receiver DCBs closer to their true physical values.

5. Since the IGS is generating DCBs for only a selected number of terrestrial stations, the proposed technique offers an alternative way of locally estimating the DCB of any receiver–satellite system using the DCB_FIX software. The advantage is that the changes in the constellation will not affect the DCB estimation, unlike when any other constraint is used.

6. With the advancement of technology, one would expect to see better hardware configuration and hence lower DCBs on board the newer satellites

of legacy constellation such as GPS, in comparison to their older satellites. This research work has successfully shown that the GPS IIF satellites appear to have lower DCBs than their older counterparts. This statement, however, cannot be applied to relatively new emerging constellations such as Galileo because these are still under development and also incorporate more sophisticated and complex signals.

7. A good agreement at the level of 1 to 2 ns was found to exist between the estimated DCBs from the DCB_FIX software and the absolute DCBs measured by the manufacturer on the ground for the 3 Galileo IOVs satellites, as published by ESA. This would have been more interesting to observe in the case of GPS satellites but despite all the efforts made by the author, it was not possible to obtain the DCBs measured on the ground by the manufacturer for the GPS satellites.

8. The comparison between calibrated and uncalibrated STEC estimation clearly shows the improvement and consistency in the estimated STEC techniques between the different receiver types. Relative to highly specialized ionospheric scintillation monitor receivers, a geodetic grade receiver like Javad Triumph–1 can also be used to compute STEC provided that the receiver and satellite DCBs are properly estimated and applied. However, the increased noise on STEC measurements in the case of Javad Triumph-I receiver clearly shows the importance of using OCXO in scintillation monitors instead of TCXO.

9. A good agreement between the IGS (or DCB_ZM) and DCB_FIX calibrated STEC plots was exhibited. This also proves that for all practical purposes of ionospheric modelling, using the ‘known’ receiver DCB as an external constraint is a valid way of resolving the rank deficiency problem that arises while computing DCB estimation for receiver/satellite network.

10. Working with cable lengths from 1 meter to 30 meter, it has been observed that with the increasing length of the cable, there is a corresponding increase in the thermal noise due to the increase in electrical resistance resulting in corresponding noisier STEC measurements. The variation in the receiver DCB with varying cable lengths from 1 meter to 30 meters was found to be of the order of 0.1 TECU to 0.2 TECU with a 1σ standard deviation of 0.025 to 0.045 TECU. Remarkably, while analysing the impact of different cable lengths on the estimation of receiver DCB, the Septentrio PolaRxS Pro receivers were found to be quite good in tracking GNSS signals at a reduced C/N0 of 15 dB-Hz without losing lock. This again highlights the importance of using an OCXO on board scintillation receivers, which in turn allows the receiver to track relatively noisy signals.

8.2 **Recommendations for Future Work**

These are some of the recommendations that can be pursued in the future with reference to the work undertaken in this research:

1. While trying to assess the possible impact of the estimated DCBs in PPP processing using the NGI’s POINT software (a research piece of software developed as part of the iNsight project, www.insight-gnss.org), two

different DCB sets were to be involved. The first set comprises of the DCBs as published by the AC whose precise products are to be used in the PPP processing. This is to carry out Type I and Type II DCB corrections as described in Section 3.7. The second set comprises of the DCBs estimated from this research to correct for the ionospheric delay. For the sake of consistency in carrying out the PPP processing, it would have been ideal to use just one DCB dataset to correct for the precise clocks and to mitigate the ionospheric delay. This would have been possible only if the DCBs estimated from this research are first used to generate the precise products and those precise products were then used in the PPP processing. There are chances that following this route might not bring any improvement, but it would be worth a try. Unfortunately, this was not possible to attempt in this research due to the time constraint and due to the main objectives of the work.

Another problem that appears while correcting the ionospheric delay with the estimated DCBs from this research and using PPP based on uncombined raw GNSS observations, was that the DCB estimates were derived from relatively noisy pseudoranges in comparison to the carrier phase observations and as such, they are not suitable to be used with carrier phase data for correcting the ionospheric delay in precise positioning. This needs to be further investigated in future.

2. The impact of the proposed technique in DCB estimation can be investigated by working with other constellations such as GLONASS and Beidou. This

however needs availability of a hardware signal simulator that is capable of generating simulated signals for both these constellations. This would also allow investigations into the inter system biases which are essential in the time transfer and other precise positioning applications.

3. From the data processing with DCB_FIX or DCB_ZM software, the quality of the LSQ solution is analysed based on the a-posteriori unit variance, which is generally found to be independent of the external constraints, whether artificial or real. This indicates the constraints are so-called ‘minimum’ constraints, whose purpose is to resolve the rank deficiency only. All the research was carried out using the global representation of VTEC based on SH expansion only. It would be worth trying to replicate the current research by using other available ionospheric models and compare their impact on the estimated DCBs.

REFERENCES

Ammar, M. (2011) Calibration of Ionospheric Scintillation and Total Electron Content Monitor Receivers. MSc Dissertation, University of Nottingham.

Andreotti, M. – Personal Communication (email), 2016.

ANOVA-I (2015) *MathWorks One-way analysis of variance* [online] Available at: https://uk.mathworks.com/help/stats/one-way-anova.html [6 October 2015]

Arikan, F., H. Nayir, U. Sezen, and O. Arikan (2008) Estimation of single station interfrequency receiver bias using GPS-TEC, *Radio Science*, 43(4). doi:10.1029/2007RS003785.

Aquino, M., Rodrigues, F. S., Souter, J., Moore, T., Dodson, A. and Waugh, S., 2005. Ionospheric scintillation and impact on GNSS users in Northern Europe: Results of a 3 year study, *Space Communications*, 20(1/2), 17-30.

Basile, F., Moore, T. and Hill, C., (2018) Analysis on the Potential Performance of GPS and Galileo Precise Point Positioning using simulated Real-Time products, International Navigation Conference (INC), 2017.

Bassiri, S. and Hajj, G. A. (1993) Higher-Order Ionospheric effects on the GPS observable and means of modelling them, *Manuscripta Geodaetica*, 18: 280-289.

Basu, S., Basu, Sa., Weber, E.J., & Coley, W.R. (1988), "Case study of polar cap scintillation modeling using DE 2 irregularity measurements at 800 km", *Radio Science*, Vol. 23, pp. 545-553.

Beach, T. L. and Kintner, P. M. (2000) Development and use of a GPS ionospheric scintillation monitor, IEEE Transactions on Geoscience and Remote Sensing, Vol. 39, No. 5, 2001.

Brunini, C., Meza, A. and Bosch, W. (2005) Temporal and spatial variability of the bias between TOPEX- and GPS-derived total electron content. *Journal of Geodesy*, 79: 175-188.

Brunner, F. K. and Gu, M. (1991) An improved model for the dual frequency ionospheric correction of GPS observations. *Manuscripta Geodaetica*, 16(3):205–214.

Bougard, B., Sleewaegen, J-M., Spogli, L., Veettil, Sreeja Vadakke, Monico, J.F. Galera (2011), "CIGALA: Challenging the Solar Maximum in Brazil with PolaRxS," *Proceedings of the 24th International Technical Meeting of The Satellite Division of the Institute of Navigation (ION GNSS)*, Portland, OR, September 20-23, pp. 2572-2579.

Box Plots (2016) *MathWorks Box Plots* [online] Available at: https://uk.mathworks.com/ help/stats/box-plots.html [10 May 2016]

Carrano, C. S. (2012) 'Ionospheric propagation effects on GNSS satellite signals' Presentation delivered during a course on *propagation effects, channel models and related error sources on GNSS*, ESAC, Madrid, Spain, October 15-17.

Chambers, J. M., William S. C., Beat K. and Paul A. T. (1983) "Comparing Data Distributions." *Graphical Methods for Data Analysis*, 62. Belmont, California: Wadsworth International Group. ISBN 0-87150-413-8, International ISBN 0-534-98052-X

Ciraolo, L., Azpilicueta, F., Brunini, C., Meza, A. and Radicella, S. M. (2007) Calibration errors on experimental slat total electron content (TEC) determined with GPS, *Journal of Geodesy*, 81(2): 111-120.

Coco, D. S., Coker, C., Dahlke, S. R. and Clynch, J. R. (1991) Variability of GPS satellite differential group delay biases. IEEE Transactions on Aerospace and Electronic Systems, 27(6):931–938.

CODE (2015) *Processing Description* [online] Available at: http://www.aiub.unibe.ch/research/code___analysis_center/global_ionosphere_maps_produced_by_code/index_eng.html [22 August 2015]

Conte, J. F., Azpilicueta, F. and Brunini, C. (2011) Accuracy assessment of the GPS-TEC calibration constants by means of a simulation technique. *Journal of Geodesy*, 85(10):707–714. doi:10.1007/s00190-011-0477-8.

Dach, R., Hugentobler, U., Fridez, P., Meindl, M. (2007) The Bernese GPS Software Version 5.0, Astronomical Institute, University of Berne, Bern, Switzerland.

David’s Statistics (2016) *Notched Box Plots* [online] Available at: https://sites.google.com/site/davidsstatistics/home/ notched-box-plots [21 June 2016]

Davies, K. (1990) *Ionospheric Radio.* 1st ed. UK: Institution of Engineering and Technology (IET).

Defraigne, P., Aerts, W., Cerretto, G., Cantoni, E. and Sleewaegen, JM. (2014) Calibration of Galileo signals for time metrology. IEEE transactions on Ultrasonics Ferroelectrics and Frequency control, 61(12):1967-75.

Dodson, A. H., Moore, T., Aquino, M. H. and Waugh, S. (2001) Ionospheric Scintillation Monitoring in Northern Europe. Proc. ION ITM, Institute of Navigation, Salt Lake City, UT, September 11-14, 2490-2498.

Durmaz, M., Karslioglu, M. O. (2015) Regional vertical total electron content (VTEC) modeling together with satellite and receiver differential code biases (DCBs) using semi-parametric multivariate adaptive regression B-splines (SP-BMARS). *Journal of Geodesy*, 89(4):347–360. doi:10.1007/s00190-014-0779-8.

Dyrud, L., Jovancevic, A., Brown, A., Wilson, D. and Ganguly, S. (2008), Ionospheric measurement with GPS: Receiver techniques and methods, *Radio Science*, 43(6) doi:10.1029/2007RS003770.

Elmas, Z. G. (2013) Exploiting New GNSS Signals to Monitor, Model and Mitigate the Ionospheric Effects in GNSS, PhD dissertation, Nottingham Geospatial Institute, The University of Nottingham, Nottingham, UK.

Feltens, J. (2007) Development of a new three-dimensional mathematical ionosphere model at European Space Agency/European Space Operations Centre, *Space Weather*, 5(12).

Feltens, J. (1998) Chapman Profile Approach for 3-d Global TEC Representation, *Proceedings of the 1998 IGS analysis centers workshop,* ESOC, Darmstadt, Germany, pp 285–297.

Galileo (2016) *Galileo IOV Satellite Metadata* [online] Available at: https://www.gsc-europa.eu/support-to-developers/galileo-iov-satellite-metadata [11 Sep 2016]

Geo-matching (2017) *Javad GNSS Triumph-I* [online] Available at: https://geo-matching.com/category/gnss-receivers/triumph-1 [19 Jul 2018]

GPS Silicon Valley (2004) GSV4004/GSV4004A GPS Ionospheric Scintillation and TEC Monitor (GISTM) User's Manual.

Hartmann, G. and Leitinger, R. (1984) Range errors due to ionospheric and tropospheric effects for signal frequencies above 100MHz, *Journal of Geodesy*, 58(2), 109-136.

Hatch, R. (1982) The synergism of GPS code and carrier measurements, Journal of Geodesy, 57(1 – 4), 207 – 208.

Hauschild, A. and Montenbruck, O. (2016) A study on the dependency of GNSS pseudorange biases on correlator spacing. *GPS Solutions*, 20(2):159-171. doi:10.1007/s10291-014-0426-0.

Hernández-Pajares, M., Juan, J. M., Sanz, J., Orus, R., Garcia-Rigo, A., Feltens, J., Komjathy, A., Schaer, S. C., Krankowski, A. (2009) The IGS VTEC maps: a reliable source of ionospheric information since 1998, *Journal of Geodesy*, 83, 263–275, http://dx.doi.org/10.1007/s00190-008-0266-1.

Hernández-Pajares, M., Juan, J. M., and Sanz, J. (1997) Neural network modelling of the ionospheric electron content at global scale using GPS data, *Radio Science*, *32*(3), 1081-1089.

Hofmann-Wellenhof, B., Lichtenegger, H., and Collins, J. (2013) *Global positioning system: theory and practice*, Springer Science & Business Media.

Hu, L., Xinan, Y. and Ning, B. (2017) Development of the Beidou Ionospheric Observation Network in China for space weather monitoring, *Space Weather*, 15, 974–984, doi:10.1002/2017SW001636.

Hunsucker, R. D. (1991) Radio Techniques for Probing the Ionosphere, Springer Verlag, New-York.

Iijima, B. A., Harris, I. L., Ho, C. M., Lindqwister, U. J., Mannucci, A. J., Pi, X., Reyes, M. J., Sparks, L. C., Wilson, B. D. (1999) Automated daily process for global ionospheric total electron content maps and satellite ocean altimeter ionospheric calibration based on global positioning system data. *J. Atmos. Sol. Terr. Phys.*, 61, 1205–1218..

IS-GPS-200H (2014) *Navstar GPS space segment/navigation user interface control document* [online] Available at: https://www.gps.gov/technical/icwg/IS-GPS-200H.pdf [13 Mar 2015].

Jakowski, N., E. Sardon, E. Engler, A. Jungstand, and D. Klaehn (1996) Relationships between GPS-signal propagation errors and EISCAT observations, *Annales Geophysicae*, 14(12):1429–1436.

Jin, R., Jin, S. G., Feng, G. (2012) M_DCB: Matlab code for estimating GNSS satellite and receiver differential code biases. *GPS Solutions*, 16 (4), 541–548.

Klobuchar, J. A. (1987) Ionospheric Time-Delay Algorithm for Single-Frequency GPS Users. *IEEE Transactions on Aerospace and Electronic Systems*, Vol. AES-23, No. 3, pp. 325-331. doi:10.1109/TAES.1987. 310829.

Klobuchar, J. A. (1996) Ionospheric Effects on GPS, *Global Positioning Systems: Theory and Applications*, *Vol I*, ed. B.W. Parkinson and J.J. Spilker Jr., American Institute of Aeronautics and Astronautics, Washington DC, pp. 485-516.

Komjathy, A. (1997). Global Ionospheric Total Electron Content Mapping Using the Global Positioning System, Ph.D. dissertation, Department of Geodesy and Geomatics Engineering Technical Report NO. 188, University of New Brunswick, Fredericton, New Brunswick, Canada, 248pp.

Komjathy A, Sparks L, Wilson BD, Mannucci AJ (2005) Automated daily processing of more than 1000 ground-based GPS receivers for studying intense ionospheric storms. *Radio Science*, 40(6). doi:10.1029/2005RS 003279.

Langley, R.B. (1996). ‘Propagation of the GPS Signals’ in GPS for Geodesy, International School, Delft, The Netherlands, 26 March - 1 April, 1995. Springer Verlag, New York.

Lanyi, G. and Roth, T. (1988) A comparison of mapped and measured total ionospheric electron content using global positioning system and beacon satellite observations, *Radio Science*, 23(4):483-492.

Leica Customer Support Team – Personal Communication (email), 2016.

Leick, A. (2004) *GPS Satellite Surveying*. 3rd ed. New Jersey: John Wiley & Sons, Inc.

Li M, Yuan Y, Wang N, Li Z, Li Y, Huo X (2017) Estimation and analysis of Galileo differential code biases. *Journal of Geodesy*, 91(3):279-293. doi: 10.1007/s00190-016-0962-1.

Li Z, Yuan Y, Fan L, Huo X, Hsu H (2014) Determination of the differential code bias for current BDS satellites. IEEE Transactions on Geoscience and Remote Sensing, 52(7):3968–3979. doi: 10.1109/TGRS.2013.2278545.

Lin, L. S. (2001) Remote sensing of ionosphere using GPS measurements. Proc. 22nd Asian Conference on Remote Sensing, Singapore, Vol. 1, pp. 69-74.

Ma, G., Gao, W., Li, J., Chen, Y., and Shen, H. (2014) Estimation of GPS instrumental biases from small scale network, *Advances in Space Research*, 54(5), 871-882.

Ma, G. and T. Maruyama (2003) Derivation of TEC and estimation of instrumental biases from GEONET Japan. *Annales Geophysicae*, 21(10):2083-2093.

Mannucci, A. J., Wilson, B. D., Yuan, D. N., Ho, C. H., Lindqwister, U. J., Runge, T. F. (1998) A global mapping technique for GPS derived ionospheric electron content measurements. *Radio Science*, 33, 565–582.

Matsakis, D. (2007) The Timing Group Delay (TGD) Corrections and GPS Timing Biases, Proc. ION 63rd Annual Meeting, Institute of Navigation, Cambridge, MA, April 23-25, 49-54.

Mayer C, Becker C, Jakowski N, Meurer M (2011) Ionosphere monitoring and inter-frequency bias determination using Galileo: first results and future prospects. *Advances in Space Research*, 47(5):859–866.

Memarzadeh, Y. (2009) Ionospheric Modelling for Precise GNSS Applications. PhD thesis, Delft University of Technology, Netherlands.

Montenbruck, O., Hauschild, A. and Steigenberger, P. (2014) Differential Code Bias Estimation using Multi-GNSS Observations and Global Ionosphere Maps. *Navigation*, 61(3): 191–201.

Montenbruck, O. and Hauschild, A. (2013) Code Biases in Multi-GNSS Point Positioning, Proc. ION ITM, Institute of Navigation, San Diego, California, January 29-27, 616-628..

MultCompare (2016) *Multiple Comparisons* [online] Available at: https://uk.mathworks.com/help/stats/multiple-comparisons.html [15 May 2016]

Mylnikova, A. A., Yasyukevich, Yu. V., Kunitsyn, V. E., Padokhin, A. M. (2015) Variability of GPS/GLONASS differential code biases. Results in Physics, Vol. 5, pp. 9-10.

NIST/SEMATECH (2016) *e-Handbook of Statistical Methods* [online] Available at: https://www.itl.nist.gov/div898/handbook/ [12 May 2016]

NovAtel (1997) *THE CSMOOTH COMMAND - PRELIMINARY* [online] Available at: https://www.novatel.com/assets/Documents/Bulletins/apn014.pdf [10 Mar 2015].

NovAtel (2018a) *GPS-702GG Dual-Frequency GPS + GLONASS Pinwheel® Antenna* [Online] Available at: https://www.novatel.com/products/gnss-antennas/high-performance-gnss-antennas/gps-702-gg/ [23 Apr 2018]

NovAtel (2018b) *GPS-703GG Triple Frequency Pinwheel® Antenna* [Online] Available at: https://www.novatel.com/products/gnss-antennas/high-performance-gnss-antennas/gps-703-ggg/ [23 Apr 2018]

Otsuka, Y., Ogawa, T., Saito, A., Tsugawa, T., Fukao, S., Miyasaky, S. (2002) A new technique for mapping of total electron content using GPS in Japan. *Earth Planets Space*, 54(1):63–70.

Ratcliffe, J. A. (1972) *An introduction to the ionosphere and magnetosphere.* 1st ed. Cambridge: Cambridge University Press.

Rao, GS. (2007) GPS satellite and receiver instrumental biases estimation using least squares method for accurate ionosphere modelling. *Journal of Earth System Science*, 116(5):407–411. doi: 10.1007/s12040-007-0039-x.

Sardón, E., Rius, A., Zarraoa, N. (1994) Estimation of the transmitter and receiver differential biases and the ionospheric total electron content from Global Positioning System observations, *Radio Science*, 29(3):577–586.

SCCS (2018) *Leica AR10 Multi-Purpose GNSS Antenna with Integrated Radome* [online] Available at: https://www.sccssurvey.co.uk/leica-ar10-multi-purpose-gnss-antenna-with-integrated-radome.html [11 Mar 2018]

Schaer, S., Gurtner, W., and Feltens, J. (1998) IONEX: The ionosphere map exchange format version 1. *Proceedings of the IGS AC workshop, Darmstadt, Germany*, Vol. 9, No. 11.

Schaer, S. (1999) Mapping and predicting the Earth's ionosphere using the Global Positioning System. PhD thesis, University of Bern.

Septentrio (2015a) PolaRxS Pro Application Manual Version 2.5.0, Septentrio Satellite Navigation, Belgium.

Septentrio (2015b) RxTools v1.10.5, Septentrio Satellite Navigation, Belgium.

Septentrio Customer Support Team – Personal Communication (email), 2015.

Septentrio (2018) *PolaNt Choke Ring B3/E6* [Online] Available at: https://www.septentrio.com/products/accessories/antennas/chokering-b3-e6 [7 May 2018]

Shanmugam, S., Jones, J., Macaulay, A., and Van Dierendonck, A. J. (2012) Evolution to modernized GNSS ionoshperic scintillation and TEC monitoring. In *Position Location and Navigation Symposium (PLANS)*, IEEE/ION 2012, pp. 265-273).

Sleewaegen, J-M. – Personal Communication (email), 2017.

Sleewaegen, J-M. – Personal Communication (email), 2015.

Sleewaegen, J-M. (2015) 'Code inter-frequency biases in GNSS receivers' Presentation delivered during IGS Workshop on *GNSS biases*, University of Bern, Switzerland, November 5-6. Available at: www.biasws2015.unibe.ch/pdf/bws15_5.3.4.pdf.

Sleewaegen, J-M. (2012) 'Optimizing GNSS receivers for scintillation monitoring. Application to the CIGALA network' Presentation delivered during a course on *propagation effects, channel models and related error sources on GNSS*, ESAC, Madrid, Spain, October 15-17.

SILSO (2017) *Sunspot Index and Long-term Solar Observations* [online] Available at: http://www.sidc.be/silso/yearlyssnplot [5 June 2017].

Spirent Communications (2009a) – Signal Generator Hardware User Manual.

Spirent Communications (2009b) – SimGEN Software User Manual.

Spirent Customer Support Team – Personal Communication (email), 2017a.

Spirent Communications (2017b) *GSS9000 Multi-Frequency, Multi-GNSS RF Constellation Simulator* [online] Available at: https://www.spirent.com/-/media/Datasheets/Positioning/GSS9000_Specifications.pdf [25 August 2017]

Sunehra, D., Satyanarayana, K., Viswanadh, C. S. and Sarma, A. D. (2010) Estimation of total electron content and instrumental biases of low latitude global positioning system stations using Kalman filter. *IETE J. Res.* 56, 235–241.

Tascione, T.F. (1988). *Introduction to Space Environment*, Orbit Book Company, Malibar, Florida.

Teunissen, P. J. G. and Montenbruck, O. (2017) Springer Handbook of Global Navigation Satellite Systems, Springer International Publishing.

Van Dierendonck, A. J. (1999) Eye on the ionosphere: Measuring ionospheric scintillation events from GPS signals, *GPS Solutions*, 2(4):60–63, doi: 10.1007/PL00012769.

Van Dierendonck, A.J., Klobuchar, John, Hua, Quyen, (1993) "Ionospheric Scintillation Monitoring Using Commercial Single Frequency C/A Code Receivers," Proceedings of the 6th International Technical Meeting of the Satellite Division of The Institute of Navigation (ION GPS 1993), Salt Lake City, UT, September 1993, pp. 1333-1342.

Van Dierendonck, A. J. and Q. Hua (2001) Measuring ionospheric scintillation effects from GPS signals, Proc. ION 57th Annual Meeting, Institute of Navigation, Albuquerque, NM, June 11-13, 391-396.

Van Dierendonck, A. J. and Arbesser-Rastburg, B. (2004) "Measuring Ionospheric Scintillation in the Equatorial Region Over Africa, Including Measurements from SBAS Geostationary Satellite Signals," Proceedings of the 17th International Technical Meeting of the Satellite Division of The Institute of Navigation (ION GNSS), Long Beach, CA, September 21-24, pp. 316-324.

Wang N, Yuan Y, Li Z, Montenbruck O, Tan B (2016) Determination of differential code biases with multi-GNSS observations. *Journal of Geodesy*, 90(3): 209–228

Wanninger, L. (1993) "Effects of the Equatorial Ionosphere on GPS." GPS World, Vol.4, No.7, pp. 48-53.

Wernik, A.W., L. Alfonsi and M. Materassi (2004) Ionospheric irregularities, scintillation and its effect on systems, *Acta Geophysica Polonica*, 52 (2), 237-249.

Wilson, B. D. and Mannucci, A. J. (1993) Instrumental Biases in Ionospheric Measurements derived from GPS data. Proc. ION GPS 1993, Institute of Navigation, Salt Lake City, UT, September 22-24, 1343-1351..

Wilson, B. D., Mannucci, A. J., Edwards, C. D. (1995) Sub daily northern hemisphere ionospheric maps using an extensive network of GPS receivers. *Radio Science,* 30, 639–648.

Yuan Y. B., Huo X. L., Ou J. K. (2007) Models and methods for precise determination of ionospheric delay using GPS. Progress in National Science, 17(2):187–196.

Zennaro, M. and Fonda, C. (2004) Radio Laboratory Handbook, Vol. 1, ICTP, Trieste, Italy.

Zhang, D. H., Shi, H., Jin, Y. Q., Zhang, W., Hao, Y. Q. and Xiao, Z. (2014) The variation of the estimated GPS instrumental bias and its possible connection with ionospheric variability, Science China Technological Sciences, 57(1), 67-79.

Zhang, D. H., Zhang, W., Li, Q., Shi, L. Q., Hao, Y. Q., and Xiao, Z. (2010) Accuracy analysis of the GPS instrumental bias estimated from observations in middle and low latitudes, *Annales Geophysicae,* 28, 1571-1580.

Zhang, W., Zhang, D. H., and Xiao, Z. (2009) The influence of geomagnetic storms on the estimation of GPS instrumental biases, *Annales Geophysicae*, 27, 1613-1623.

Zhang, Y., Wu, F., Kubo, N., Yasuda, A. (2003) TEC measurement by single dual-frequency GPS Receiver. Proc. International Symposium on GPS/GNSS, Tokyo, Japan, 351-358.

Zhong, J., Lei, J., Dou, X., And Yue, X. (2015) Is the long-term variation of the estimated GPS differential code biases associated with ionospheric variability? *GPS Solutions*, 20(3):313–319.

Zolesi, B. and Cander, L. R. (2014) Ionospheric prediction and forecasting, Springer Geophysics, Heidelberg, Germany, ISBN 978-3-642-38429-5, DOI: 10.1007/978-3-642-38430-1.

Zumberge, J. F., Heflin, M. B., Jefferson, D. C., Watkins, M. M. & Webb, F. H. (1997) Precise point positioning for the efficient and robust analysis of GPS data from large networks. *Journal of Geophysical Research: Solid Earth*, 102, 5005-5017.

APPENDIX A

JOURNAL PAPER

GPS Solutions (2018) 22:32
https://doi.org/10.1007/s10291-018-0700-7

ORIGINAL ARTICLE

Estimation and analysis of multi-GNSS differential code biases using a hardware signal simulator

M. Ammar[1,2] · M. Aquino[1] · S. Vadakke Veettil[1] · M. Andreotti[3]

Received: 2 August 2017 / Accepted: 6 January 2018

Abstract
In ionospheric modeling, the differential code biases (DCBs) are a non-negligible error source, which are routinely estimated by the different analysis centers of the International GNSS Service (IGS) as a by-product of their global ionospheric analysis. These are, however, estimated only for the IGS station receivers and for all the satellites of the different GNSS constellations. A technique is proposed for estimating the receiver and satellites DCBs in a global or regional network by first estimating the DCB of one receiver set as reference. This receiver DCB is then used as a 'known' parameter to constrain the global ionospheric solution, where the receiver and satellite DCBs are estimated for the entire network. This is in contrast to the constraint used by the IGS, which assumes that the involved satellites DCBs have a zero mean. The 'known' receiver DCB is obtained by simulating signals that are free of the ionospheric, tropospheric and other group delays using a hardware signal simulator. When applying the proposed technique for Global Positioning System legacy signals, mean offsets in the order of 3 ns for satellites and receivers were found to exist between the estimated DCBs and the IGS published DCBs. It was shown that these estimated DCBs are fairly stable in time, especially for the legacy signals. When the proposed technique is applied for the DCBs estimation using the newer Galileo signals, an agreement at the level of 1–2 ns was found between the estimated DCBs and the manufacturer's measured DCBs, as published by the European Space Agency, for the three still operational Galileo in-orbit validation satellites.

Keywords Differential code biases · Total electron content · Hardware delays · STEC · Simulator

Introduction

In the last few decades, specialized Global Navigation Satellite System (GNSS) Ionospheric Scintillation Monitor Receivers (ISMRs), such as the NovAtel/AJ Systems GSV4004 and the Septentrio PolaRxS Pro, have been developed with a view to support continuous ionospheric modeling by estimating total electron content (TEC) and different scintillation parameters. However, it is not a straightforward task to derive accurate TEC information from these specialized receivers because the recorded code-based pseudorange measurements are contaminated by instrumental biases, the so-called differential code biases (DCBs), existing between the code observations from different frequencies, at both the satellite and receiver ends (Wilson and Mannucci 1993). Considering these existing hardware delays to be stable for reasonable periods of time, the recorded TEC measurements have been used quite successfully on a relative basis in a number of experiments. Yet, to enable the calculation of absolute TEC for ionospheric monitoring, these receivers must be calibrated to account for their respective DCBs. Ignoring the satellite and receiver DCBs when computing TEC may result in an error of up to 20 TECU (or 7 ns) for satellites and 40 TECU (or 14 ns) for receivers, and their cumulative effect can reach as much as 100 TECU (or 35 ns) in extreme cases (Sardón et al. 1994). If not accounted for, these can also sometimes lead to non-physical negative TEC values (Ma and Maruyama 2003; Mylnikova et al. 2015). This could become even worse for the more recent new GNSS signals and hence cannot be ignored (Montenbruck et al. 2014; Wang et al. 2016).

✉ M. Ammar
Muhammad.Ammar@nottingham.ac.uk

1 Nottingham Geospatial Institute, University of Nottingham, Nottingham, UK

2 NUST Institute of Civil Engineering, National University of Sciences & Technology (NUST), Islamabad, Pakistan

3 NovAtel Inc., Calgary, AB, Canada

Published online: 13 January 2018

With the advent of modernized GPS, GLONASS and the new Galileo and Beidou signals in addition to the legacy GPS and GLONASS signals, a variety of signal pairs is available to compute TEC. However, the associated DCBs and different available tracking modes, such as pilot only and combined, make the accurate TEC computation even more challenging.

Van Dierendonck (1999) and Van Dierendonck and Hua (2001) defined a calibration procedure for GSV4004 monitors, by comparing their estimated TEC data with a 'reference' TEC, such as that generated by the International GNSS Service (IGS) or a space-based augmentation system (SBAS), an approach attempted in Dodson et al. (2001). Additionally, different algorithms for computing these DCBs have also been proposed in the past. For single station receiver DCB estimate, these can be roughly categorized in two groups (Arikan et al. 2008; Komjathy et al. 2005; Li et al. 2014, 2016). The first group models vertical TEC (VTEC) as a polynomial that is a function of ionospheric pierce point coordinates in a coordinate system referenced to the earth–sun axis. Both the satellite and receiver DCBs are considered as unknowns along with other coefficients and are solved for in a least squares (LSQ) solution (Lanyi and Roth 1988; Sardón et al. 1994; Jakowski et al. 1996; Lin 2001; Otsuka et al. 2002, Rao 2007; Yuan et al. 2007; Mayer et al. 2011; Durmaz and Karslioglu 2015). The second group uses the method of minimization of the standard deviation of VTEC using different receiver trial biases and the one that minimizes the standard deviation of computed VTEC is chosen as the receiver bias for that particular station (Ma and Maruyama 2003; Zhang et al. 2003; Komjathy et al. 2005; Arikan et al. 2008, Montenbruck et al. 2014).

The published DCB products are routinely estimated by different analysis centers (ACs) of the IGS as a by-product of their local or global ionospheric analyses for almost all the available satellites in different constellations and a selected number of IGS or Multi-GNSS Experiment (MGEX) stations. A linear geometric combination of code-based pseudoranges is employed by the ACs to derive the DCBs on a daily basis along with a set of ionospheric coefficients. However, this is a rank deficient system and an external constraint must be employed to break the rank deficiency and separate the satellite DCBs from the receiver DCBs. This is normally achieved by constraining the mean of the satellites DCBs to zero, in a so-called 'zero mean constraint.' Consequently, with the routine changes carried out in the satellite constellations, frequent jumps can be observed in the estimated DCBs (Zhong et al. 2015). On the other hand, the problem of rank deficiency can also be resolved by constraining the solution to a known receiver DCB in the network instead. The advantage of using this approach is that a more realistic and stable set of satellite and receiver DCBs are estimated.

For global TEC monitoring and other related applications, it would be straightforward to carry out the analysis provided the receiver with the known DCB is part of the IGS/MGEX network. However, as in a general situation this receiver will not be part of the network, its DCB must be obtained from the manufacturer or otherwise carefully estimated through a technique that can ensure that it is consistent with the available set of satellite DCBs. We hereby introduce a technique for satellite and receiver DCB estimation by first estimating the DCB of an available receiver through simulation and afterward 'inserting' this receiver in a global network for processing. For carrying out this technique, a Septentrio PolaRxS Pro ISMR, referred to hereafter as 'SEPT,' was used in conjunction with the Spirent GSS8000 hardware simulator, in a simulation where the state of the ionosphere, troposphere and the other group delays could be controlled, as demonstrated in Ammar (2011). Once the receiver DCB has been estimated, it is then used to constrain the solution in a global network of stations following the strategy implemented by the Centre of Orbit Determination in Europe (CODE), to ultimately estimate the DCBs of the satellites and all the other receivers involved in the network (Schaer 1999). The final results should produce a consistent set of stable DCBs, which are now closer to their physical values and therefore more representative to be employed in any TEC monitoring application. For validation purposes, another Septentrio PolaRxS Pro ISMR and a Javad Triumph-I receiver are also involved. These are referred to hereafter as 'SEP2' and 'JAVD,' respectively. Moreover, the idea of working with an ISMR as a primary receiver was originally conceived because of the specific feature of this receiver to estimate TEC for ionospheric monitoring purposes, where the estimation of DCBs is desirable so that absolute and calibrated TEC can be obtained. Nevertheless, the proposed technique can be applied to any conventional multi-frequency, multi-constellation receiver, as long as its capabilities can be reflected in the GNSS simulator.

It is important to remember that the calibrated DCBs obtained via simulators can vary between simulators based on their ability to generate high quality signals and on their intrinsic hardware delays. Further complications can arise from the fact that there may exist differences between live and simulated signals depending on correlator spacing and multipath mitigation techniques (Hauschild and Montenbruck 2016). This would not be a problem in TEC monitoring due to relative time independence of the satellites and receivers DCBs, but for other precise operations such as time transfer, this must be given due consideration.

DCB in the context of TEC estimation

For a specific GNSS constellation, the difference of two code-based pseudorange measurements obtained from two signals, in linear units, equals the sum of the differential ionospheric path delays and the respective satellite and receiver DCBs. If both signals share the same frequency, as in the case of C_1 and P_1, the combined satellite and receiver DCB equals the average difference of the respective code measurements (Montenbruck and Hauschild 2013). This can be written as follows:

$$P^s_{ir} - P^s_{jr} = \left(I_i - I_j\right) + \mathrm{DCB}^s_{Pi-Pj} + \mathrm{DCB}_{r,Pi-Pj} \tag{1}$$

Here, the superscript 's' and the subscript 'r' are used to refer to satellite and receiver, respectively. The subscripts '*i*' and '*j*' can be 1, 2 or 5 depending upon the carrier frequency in use. Also, $P^s_{i,r}$ and $P^s_{j,r}$ are the code pseudorange observables on carrier frequencies L_i and L_j with corresponding ionospheric delays as I_i and I_j, respectively. The frequency-dependent ionospheric delay (in meter) can be further written in the generalized form as follows:

$$I = \frac{40.3}{f_L^2} \times \mathrm{STEC} \tag{2}$$

f_L refers to the frequency (in Hz) of the signal L, and STEC is the Slant TEC (in meter) between the satellite transmitter and the receiver antenna.

Working with GPS, the correction parameter for the satellite DCB between P1 and P2 pseudoranges on GPS L1 and L2 signals (or DCB^s_{P1-P2}) is referred to as the estimated group delay differential or T_{GD} and this is provided to the users through the broadcast message. The relation between satellite DCB^s_{P1-P2} and T_{GD} is given as follows (IS-GPS-200H 2014):

$$T_{GD} = \frac{1}{1-\gamma}\mathrm{DCB}^s_{P1-P2} \tag{3}$$

where for GPS L1 and L2 frequencies,

$$1-\gamma = 1 - \frac{f_{L1}^2}{f_{L2}^2} = 1 - \frac{\left(1575.42\times10^6\right)^2}{\left(1227.60\times10^6\right)^2} = -0.647 \tag{4}$$

Using (2)–(4) and the definition of 1 TEC Unit (TECU) which is equal to 10^{16} electrons/m^2, the standard equation that can be used in any dual frequency receiver generating P_1 and P_2 to compute STEC in TECU can be written as follows:

$$\mathrm{STEC} = 9.5238 \times \left[\left(P_2 - P_1\right) - 0.647T_{GD} + \mathrm{DCB}_{r,P1-P2}\right] \tag{5}$$

Similarly, working with Galileo E_1 and E_{5a} code observables, the STEC equation can take the following form:

$$\mathrm{STEC} = 7.764 \times \left[\left(E_{5a} - E_1\right) - 0.7933B_{GD} + \mathrm{DCB}_{r,E1-E5a}\right] \tag{6}$$

where $\mathrm{DCB}_{r,E1-E5a}$ is the differential code bias between Galileo E_1 and E_{5a} signals and B_{GD}, i.e., the broadcast group delay is the correction parameter for DCB^s_{E1-E5a} as transmitted in the navigation message by the Galileo satellites.

For either (5) or (6), if the terms STEC, T_{GD} and B_{GD} are controlled in simulation by setting them to 0, then the DCB of the receiver can directly be estimated from the observations. Here we assume that the simulator DCB is negligible and can be ignored.

M_DCB software

Jin et al. (2012) developed an open-source M_DCB software package in MATLAB to estimate the global or regional receivers and GPS satellites DCBs. This is based on the CODE's global ionospheric analysis strategy in which the VTEC is expressed as a spherical harmonic expansion of a degree and order 15. Differences of less than 0.7 ns and an RMS of less than 0.4 ns were found to exist between the M_DCB software and IGS ACs products (e.g., JPL, CODE and IGS combined). We modify this software to not only handle the external constraint of known receiver DCB but also to handle the newer GPS L5 and Galileo E_1 and E_{5a} signals, which were not covered in the original package. Hereafter, the revised version of the M_DCB software with the external constraint of zero mean condition on the satellites DCBs is referred to as the 'DCB_ZM,' whereas with the external constraint of known receiver DCB, it is referred to as the 'DCB_FIX.'

Receiver DCB estimation using simulation (methodology)

The approach that was followed to estimate the receiver DCB was to use the Spirent GSS8000 hardware signal simulator to generate all possible GNSS signals without ionospheric and tropospheric delays, as well as eliminating simulated satellite signal delays such as T_{GD} and B_{GD} by setting them to 0. The Septentrio PolaRxS (SEPT) receiver was set to track these simulated signals under default tracking loop parameters with no multipath mitigation as presented in Table 1. From the recorded RINEX observations, the STEC was computed based on (5) for GPS and (6) for Galileo depending upon the signal combination, using all the available satellites. The mean of the computed STEC for all the satellites essentially gave the DCB of the receiver for a particular signal combination. The same methodology was followed for the DCB estimation of SEP2 and JAVD receivers, and the different tracking parameters applied to these receivers are also presented in Table 1.

Cable DCB

The antenna cable is commonly considered a non-dispersive medium (Defraigne et al. 2014). However, Dyrud et al.

Table 1 Different tracking parameters applied during simulations and real data collection for the different receiver systems

Receiver system	Delay locked loop (DLL) tracking loop		Smoothing interval (s)	Multipath mitigation
	Bandwidth (Hz)	Order		
SEPT	0.25	2	Not applied	Off
SEP2	0.25	2	Not applied	Off
JAVD	3	1	100 (default)	Off

(2008) showed that a small constant variation of 0.004 m or approximately 13 ps (picoseconds) can exist in the absolute DCB of the receiver system while working with different cable lengths. Working on a similar strategy with different lengths of the RG213 coaxial cables ranging from 1 to 30 m, Ammar (2011) also showed variations of up to 35 ps in the estimated DCB between P1 and P2 pseudoranges using simulated data. These small variations in the absolute DCB of the receiver system with varying cable lengths can be explained on the basis of the additional noise that the longer cables introduce in the pseudorange measurements in comparison to the shorter ones. To rule out any minor effect coming from the cable, the same antenna cable of 20 m length was used with the SEPT receiver both to connect it with the simulator and to connect it with the antenna for open sky data collection. On the other hand, the same was not possible for the other two receivers, SEP2 and JAVD, because of the difficulty in taking existing routed cables out of the building fixtures. Therefore, to keep the noise level to a minimum, the smallest available 1-m cable was used to connect them to the simulator during the estimation of their respective DCBs.

Antenna DCB

The antenna DCB (also referred to as the differential group delay) should also be given due importance because in an open sky situation it obviously forms part of the overall DCB of the data recording system comprising the antenna, the cable and the receiver itself.

For the specific NovAtel GPS 702GG antenna that was used initially with the SEPT receiver, the DCB of − 2.7 ns was provided by the manufacturer between L1 and L2. It was measured at 23 °C and with 4.53 V power supply (NovAtel 2016).

For the Leica AR10 antennas that were used initially with the SEP2 and JAVD receivers, the DCB value of 3 ns between L1 and L2 was provided (Leica 2016). This is not antenna specific and is just the maximum DCB value as estimated by the manufacturer at 22 °C for all the Leica AR10 antennas. More recently, to accommodate the newer GPS L5 and Galileo signals, the antenna used with the SEPT receiver has been upgraded to the NovAtel GPS 703GGG. For this particular antenna, the DCBs between L1 and L2 and between L1 and L5, as computed by the manufacturer at 25 °C and with 4.5 V power supply, are 2.2 and 1.3 ns, respectively (NovAtel 2016). SEP2 antenna has also been upgraded to Septentrio choke ring antenna, but no differential group delay value has been provided by the manufacturer.

Satellites and receivers DCBs estimation from real data (methodology)

Initially 'Network A' of 96 stations, comprising of 93 IGS stations and 3 additional stations, namely SEPT, SEP2 and JAVD that were set up at the Nottingham Geospatial Institute (NGI), was chosen to be part of the global ionospheric analysis using the DCB_FIX software. These stations are represented by red dots in Fig. 1. For consistency and compatibility with the original M_DCB software, these stations were specifically selected to consist of GPS P1, P2 receiver types only. The estimated DCBs from the DCB_FIX software are later compared with the IGS published daily DCB estimates given in IONEX format. The estimated ionospheric coefficients as part of the LSQ processing are not analyzed in any way for the generation of global ionospheric maps (GIMs).

To incorporate the modernized GPS L5 signal and the newer Galileo E_1 and E_{5a} signals, a new network of 41 stations comprising of 39 IGS or MGEX stations and 2 NGI stations, i.e., SEPT and SEP2, was chosen to be part of the DCB estimation using the DCB_FIX software.

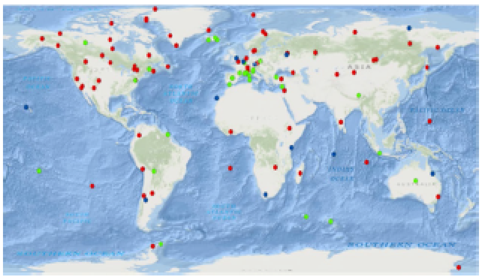

Fig. 1 Red—Network A; green—Network B; blue—common stations in both the networks

This network is referred to as 'Network B,' and the corresponding stations are represented by green dots in Fig. 1. Also, this network selection was dictated by the fact that the SEPT receiver incorporates a pilot only tracking technique and limited receivers in the IGS or MGEX network are currently available with the same tracking technique. While Li et al. (2016) were able to use a network of 100 plus stations tracking Galileo based on their localized ionospheric modeling, it can still be a problem for the research groups working with a global ionospheric model to obtain a good spread of stations worldwide. Finally, the blue dots in Fig. 1 are the stations that are common in both the networks.

Results for estimated receivers DCBs using simulation

To estimate the DCB of the SEPT receiver, data from three 26-h simulations was captured, where the ionosphere, troposphere and the group delays are set to 0. The simulated signals are recorded by the SEPT receiver using a 20 m RG213 coaxial cable. The first two hours of the simulations are discarded to allow for the simulator and receiver hardware to reach stable operating temperatures. The DCBs for the desired signal combinations are computed independently from the code-based pseudoranges as recorded in the RINEX files.

Figures 2 and 3 show the estimated DCBs for the SEPT receiver between GPS P1/P2, C1/P1, C1/P2, C1/C5 and Galileo E_1/E_{5a}. The mean and one sigma standard deviation of these DCBs (in ns) across the three simulations were found to be − 1.70 ± 0.53, 0.03 ± 0.09, − 1.67 ± 0.52, − 4.97 ± 0.44 and − 5.21 ± 0.26, respectively. The consistency between these estimates was confirmed by verifying the following relation:

$$\mathrm{DCB}\,(\mathrm{C1-P1}) + \mathrm{DCB}(\mathrm{P1-P2}) = \mathrm{DCB}(\mathrm{C1-P2}) \quad (7)$$

Following the same methodology, Figs. 4 and 5 show the DCB estimates for SEP2 and JAVD receivers, respectively, for only the GPS P1/P2 code combination. The mean and one sigma standard deviation of these DCBs (in ns) across the three simulations were found to be − 1.90 ± 0.31 and 6.83 ± 1.35, respectively.

From Figs. 2 to 5, it can be seen that the ISMRs present a lower noise level than the JAVD receiver even without the application of carrier phase smoothing. However, keeping in mind that the ISMRs are working under different tracking parameters (Table 1), a fair comparison would only be possible by using a consistent set of tracking parameters for all the three receivers.

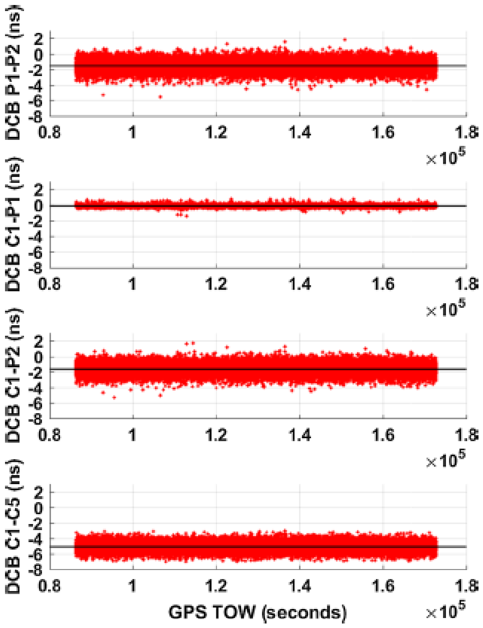

Fig. 2 Plots showing DCBs between different GPS signal combinations (in ns) versus GPS Time of Week—TOW (in seconds) as observed by all the satellites in one simulation run (SEPT Receiver)

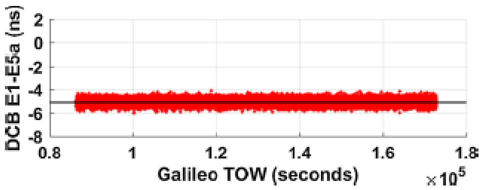

Fig. 3 Plot showing DCB between Galileo E_1 and E_{5a} (in ns) versus Galileo TOW (in seconds) as observed by all the satellites in one simulation run (SEPT receiver)

Results for estimated satellites and receivers DCBs using Network A (GPS P1/P2 only)

Using the DCB_FIX software with the archived RINEX data of 96 stations (Network A) from March 17 to April 7, 2016 (22 days), and the spherical harmonics of degree and order 15, the processing was run on a day to day basis with the solution constrained to the known DCB value of the SEPT receiver system. A known DCB value of − 4.41 ns

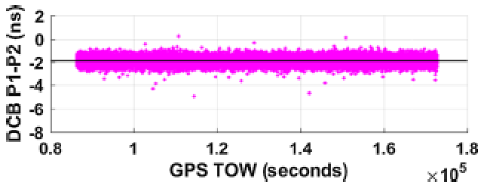

Fig. 4 Plot showing DCB between GPS P1 and P2 (in ns) versus GPS TOW (in seconds) as observed by all the satellites in one simulation run (SEP2 receiver)

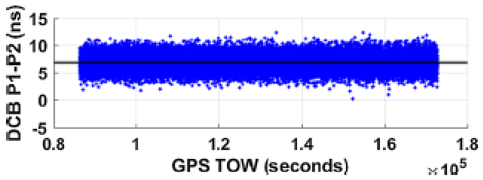

Fig. 5 Plot showing DCB between GPS P1 and P2 (in ns) versus GPS TOW (in seconds) as observed by all the satellites in one simulation run (JAVD receiver)

was used for the SEPT receiver system which is the sum of the antenna DCB (see the section on antenna DCB) and the mean receiver DCB as computed in the previous section. Also, the selection of these 22 days was made on the basis that two additional receivers, i.e., SEP2 and JAVD, were available during that time to validate the results along with their antenna DCBs.

In Figs. 6 and 7, the red curves show the mean DCBs as estimated by the IGS, whereas the blue curves show the mean DCBs as estimated by the DCB_FIX software. Note that the mean DCB for both the satellites and receivers is computed over a period of 22 days. Also, in Fig. 6, the GPS satellites are grouped together as per the different family blocks to which they belong. It can be observed that a similar pattern exists between the IGS computed DCBs and the DCBs estimated through the DCB_FIX software. However, stable mean offsets of − 3.47 ns for satellites and + 3.54 ns for receivers were found to exist between the estimated DCBs and the IGS published DCBs. A possible explanation is that the zero mean satellite DCB constraint, although effective to break the rank deficiency, imposes an artificial shift on the estimated DCBs. By using a more realistic constraint in the form of a properly estimated receiver DCB, the resulting DCBs are closer to their actual values. The more accurate the known DCB used to constrain the solution, the more accurate the estimated DCBs for the other receivers and satellites.

The DCB estimates for SEP2 and JAVD receiver systems from the DCB_FIX software and the DCB_ZM software are investigated as per in Table 2:

Since the maximum DCB value of 3 ns for Leica AR10 antenna has been used to compute the overall known DCB of the two receiver systems as discussed in the earlier section on antenna DCB, it is quite remarkable that the DCB_FIX software has been able to estimate the DCBs for the two receiver systems within few tenths of a nanosecond. The accuracy of the DCB estimated by the DCB_FIX is also independent of the fact that the SEP2 receiver is of a relatively higher quality in comparison with the geodetic grade JAVD receiver. When constrained by the zero mean condition, the DCB_ZM software produces DCB estimates comparable to the IGS DCB solution and it can be seen from Table 2 that the latter are over estimated by about 3.5 ns. On the other hand, the satellite DCBs estimated by IGS are under estimated by approximately the same amount when compared to those estimated by the DCB_FIX software (Fig. 6).

Fig. 6 Plot showing the average GPS satellite DCBs between P1 and P2 estimated by the DCB_FIX software (SEPT = − 4.41 ns) and IGS (CODE) over a period of 22 days (March 17 to April 7, 2016)

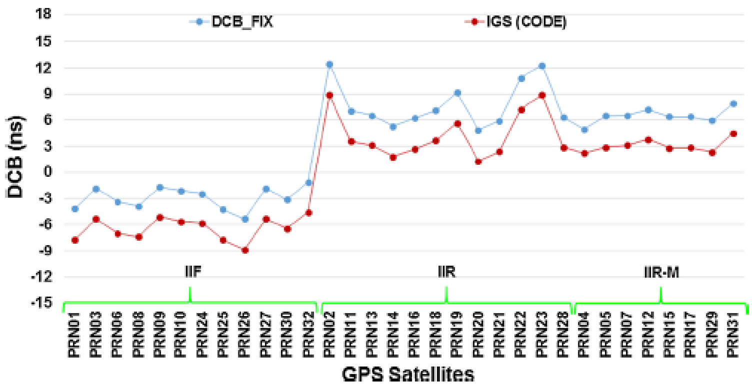

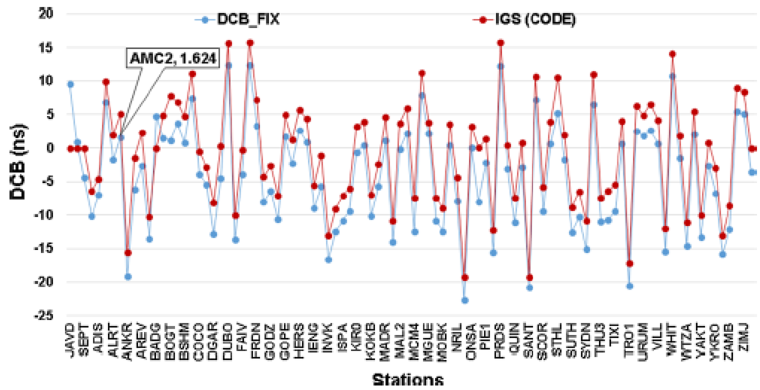

Fig. 7 Plot showing the average receivers' DCBs between P1 and P2 estimated by the DCB_FIX software (SEPT = − 4.41 ns) and IGS (CODE) over a period of 22 days (March 17 to April 7, 2016)

Table 2 DCB estimates of SEP2 and JAVD receiver systems from the simulator/antenna combination, DCB_FIX software and DCB_ZM Software (IGS)

Receiver system	DCB P1-P2 estimates (in ns)		
	Receiver/cable (simulator) + antenna (manufacturer)	DCB_FIX	DCB_ZM
SEP2	1.10	0.92 ± 0.27	4.40 ± 0.22
JAVD	9.83	9.60 ± 0.53	13.05 ± 0.6

It can also be seen from Fig. 6 that the satellite DCBs for the newer generation of GPS block IIF satellites are lower than the previous generation of satellites. One possible explanation can be that with the advancement in technology, the newer satellites are better equipped in terms of quality of hardware to handle in-orbit temperatures and hence possess lower DCBs. The temperature sensitivity for signals transmitted by satellites in orbit is discussed in Coco et al. (1991).

Stability of estimated DCBs (GPS P1/P2 only)

To investigate the stability of the estimated DCBs using the DCB_FIX software, the standard deviations of both the satellites and the receivers DCBs are plotted in Figs. 8 and 9 respectively. The estimated DCBs are generally stable over time for both the satellites and the receivers. The average standard deviations of the estimated satellite and receiver DCBs are found to be 0.15 and 0.45 ns, respectively. Sudden jumps in standard deviations may indicate a possible replacement of the satellite or receiver or any part of the receiver system, such as antennas and cables. In some cases, it can also indicate potential hardware issues within the receiver or receiver architecture. These are, however, difficult to investigate because of the independent working

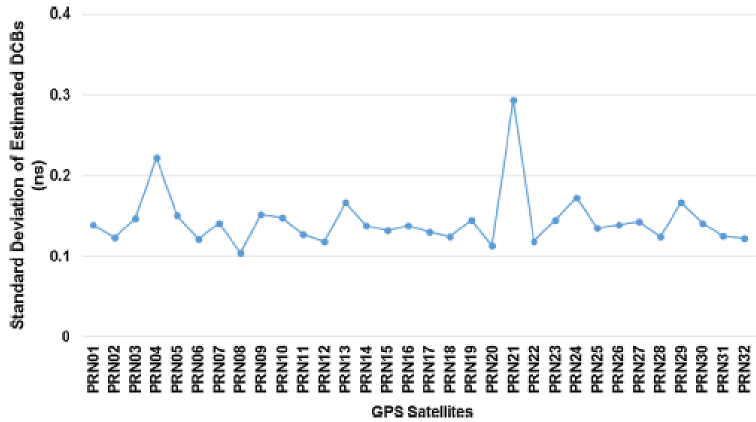

Fig. 8 Plot showing the standard deviations of the GPS satellites DCBs between P1 and P2 estimated by the DCB_FIX software over a period of 22 days (Network A—March 17 to April 7, 2016)

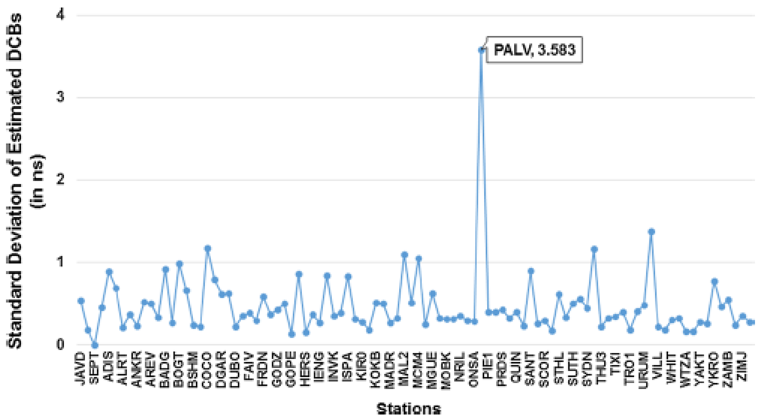

Fig. 9 Plot showing the standard deviations of the receivers DCBs between P1 and P2 as estimated by the DCB_FIX software over a period of 22 days (Network A—March 17 to April 7, 2016)

of the IGS and MGEX stations. In Fig. 9, a peak can be observed in the standard deviation of 'PALV' receiver system DCB—this is because the receiver was changed on the March 29, 2016, as published in the station log file (https://igscb.jpl.nasa.gov/igscb/station/log/ palv20160329.log) and the replacement receiver has a significantly different DCB. As receivers from the same brand have relatively similar DCBs, it can be difficult to identify their replacement based on the standard deviations' figures only.

In all the above data processing with DCB_FIX or DCB_ZM software, the quality of the LSQ solution is analyzed based on the a posteriori unit variance or the standard error of observation, which is generally found to be independent of the external constraints, whether artificial or real. Therefore, the quality of the LSQ solution can only be improved by using a more refined model in the global ionospheric analysis.

Results for estimated satellites and receivers DCBs using Network B (Galileo E_1/E_{5a} only)

Using the DCB_FIX software with the archived RINEX data of 41 stations (Network B) from October 4, 2016, up to November 15, 2016 (43 days), and a degree and order of 15 for the spherical harmonics, the processing was run on a day to day basis, constrained by the known DCB value between Galileo E_1 (C1C) and E_{5a} (C5Q) signals for the SEPT receiver system. This value was estimated in simulation using the previously explained strategy as − 3.91 ns.

From the estimated satellite and receiver DCBs, the results with a relatively higher average standard deviation of 0.54 and 1.24 ns, respectively, have been observed. Also, the DCB estimates of some of the stations and the Galileo E24 satellite have been ignored in the computation of these standard deviations because abnormally high DCBs were estimated on some days of the processing. One possible explanation for these abnormalities and relatively higher standard deviations is that the hardware technology that is currently in place to transmit and process these newer signals is still under test phase and in the process of refinement. For the sake of conciseness, the figures showing the estimated satellites and receivers DCBs are not presented. Table 3 compares for three Galileo IOV (in-orbit validation) satellites, the DCBs estimated using the DCB_FIX software with the manufacturer measured DCBs that have recently been published by the European Space Agency (ESA) on its website (Galileo 2016). Note that these published values for IOVs are based on absolute calibration carried out on ground against a payload verification system.

It can be seen from Table 3 that the DCB estimates from the DCB_FIX software agree with the manufacturer measured on ground DCBs at the level of 1 to 2 ns. The results obtained by the DCB_FIX software are expected to improve further once the simulator DCB is accounted for in this processing strategy. Minor improvements have also been observed in the DCB estimation by increasing the degree and order of the spherical harmonics in the global VTEC expression.

Results for estimated STEC using different calibration strategies (GPS P1/P2 only)

Based on Eq. (5) and using daily RINEX datasets, the STEC is estimated for different co-located receivers in the network, with the purpose of comparing the different STEC estimation strategies. The uncalibrated STEC refers to the case where no DCBs were applied and the calibrated STEC refers

Table 3 Comparison of Galileo IOV Satellite DCBs as estimated from the DCB_FIX Software with the ESA published manufacturer measured on ground DCBs

Galileo PRN	DCB E_1–E_{5a} estimates (in ns)			
	ESA published DCBs (I)	DCB_FIX software (II)	DCB derived from B_{GD}	Difference between (II) and (I)
E11	9.71 ± 0.38	11.07 ± 0.52	16.62	1.36
E12	6.97 ± 0.41	8.80 ± 0.37	14.77	1.83
E19	2.15 ± 0.48	3.06 ± 0.29	8.12	0.91

to the case where either IGS published DCBs or DCB_FIX estimated DCBs were applied.

Figure 10 shows the STEC plots constructed on the basis of different calibration strategies for PRN 24, as observed by the three NGI receivers, i.e., SEPT, SEP2 and JAVD, on the ionospherically quiet day of March 26, 2016. The improvement and consistency in the estimated STEC as observed by three different receivers can be clearly seen from these plots between uncalibrated and calibrated solutions. It is also apparent that, in comparison with the highly specialized ISMRs such as SEPT and SEP2, the geodetic grade receiver, the Javad Triumph – 1, can also be used to generate almost similar STEC, if receiver and satellite DCBs can be properly estimated. Here, one minor concern would be the increased noise level in the JAVD's TEC measurements even after the application of smoothing. However, as previously stated, a fair comparison would only be possible by using a consistent set of tracking parameters for all three receivers. Note that all three receivers are connected separately to three different antennas and were operating under different tracking parameters, as presented in Table 1.

From Fig. 10, it can also be observed that there is a good agreement between IGS (or DCB_ZM) calibrated and DCB_FIX calibrated STEC plots. This demonstrates that for all practical purposes of ionospheric modeling, using the 'known' receiver DCB as an external constraint in comparison to the IGS strategy represents a perfectly valid way of resolving the rank deficiency problem.

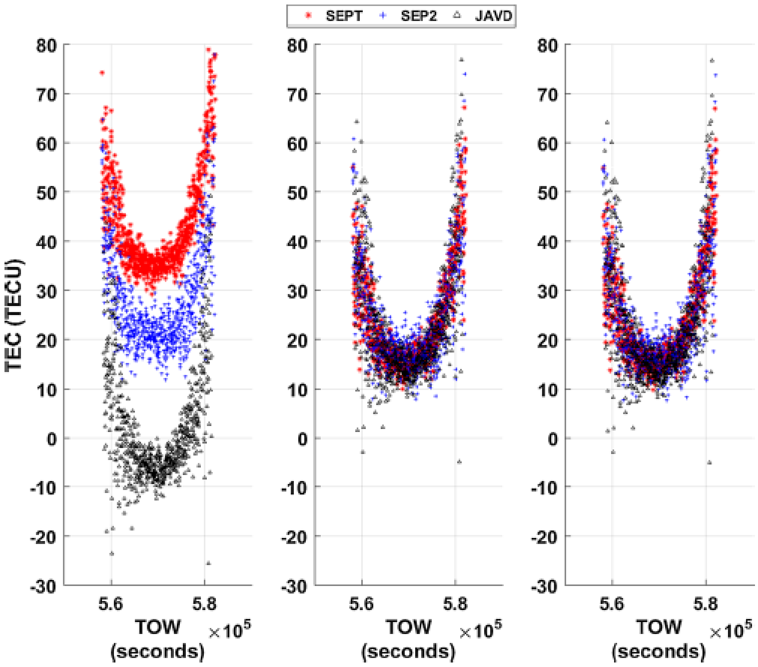

Fig. 10 Uncalibrated (left), IGS or DCB_ZM calibrated (center) and DCB_FIX calibrated (right) STEC plots for PRN 24 as observed by SEPT, SEP2 and JAVD receiver systems (March 26, 2016)

Estimation of simulator DCB (For GPS P1/P2 Only)

As contrary to our earlier assumption of negligible simulator DCB, a strategy was devised to estimate the contribution of the simulator in the DCB estimation by involving the IGS AMC2 station. From the log file of AMC2 station (https://igscb.jpl.nasa.gov/igscb/station/log/amc2_20140915.log), it can be seen that the individual hardware delays existing between different components of the system such as antenna, antenna cable, antenna splitter, receiver, etc., have already been measured and applied to the raw code-based pseudoranges. Although not knowing exactly how these individual delays are measured, it is considered here that the measurements are done accurately enough. Based on that assumption, one can expect to get a DCB value close to 0 for this station when estimating DCBs using a 'known' receiver DCB, provided that the ionosphere has been correctly modeled. As shown in Fig. 7, by using the DCB_FIX software, a mean DCB value of + 1.62 ns was estimated for this station, implying therefore that a value of − 1.62 ns with some uncertainty can be interpreted to represent the DCB of the simulator itself existing between GPS P1 and P2 signals. Hence, it can be inferred that the simulator DCB for a certain signal combination can be measured by exploiting the proposed strategy in conjunction with a station receiver with accurately known hardware delays and this would further push the estimated DCBs toward their physical values.

Conclusions

1. A hardware signal simulator such as the Spirent GSS8000 can be effectively used to estimate a consistent set of DCBs between different signal combinations for any multi-frequency, multi-constellation receiver. The proposed technique can be improved further by accounting for the simulator delays as well.
2. The receiver DCB is often mistaken as a function of the receiver hardware only. This is in fact not true because in an open sky situation, the receiver DCB refers to the DCB of the entire 'system' comprising of antenna, cable and the receiver itself. Therefore, it should be ensured that if a receiver DCB is to be used to estimate the satellites and receivers DCBs in a regional or global network, the DCB of the whole system is used to constrain the solution; otherwise, one can expect variations in the estimated DCBs with the changing system components such as antenna, cable, splitter.
3. Since the IGS is generating DCBs for only a selected number of terrestrial stations, the technique proposed offers an alternative way of locally estimating the DCB of any receiver—satellite system using the DCB_FIX software. The advantage would be that the changes in the constellation will not affect the DCB estimation, unlike when any other constraint is used.
4. A good agreement at the level of 1 to 2 ns was found to exist between the estimated DCBs from the DCB_FIX software and the manufacturer measured on ground absolute DCBs for the 3 Galileo IOVs satellite as published by the ESA.
5. The comparison between calibrated and uncalibrated STEC estimation clearly shows the improvement and consistency in the estimated STEC techniques between the different receiver types. Relative to highly specialized ionospheric scintillation monitor receivers, a geodetic grade receiver like Javad Triumph − 1 can also be used to compute STEC provided that the receiver and satellite DCBs are properly estimated and applied.
6. A good agreement between the IGS (or DCB_ZM) and DCB_FIX calibrated STEC plots was demonstrated. This also demonstrates that for all practical purposes of ionospheric modeling, using the 'known' receiver DCB as an external constraint is a demonstrated valid way of resolving the rank deficiency problem that arises when computing DCB estimations for receiver/satellite network.

Acknowledgements M. Ammar is grateful to the National University of Sciences and Technology (NUST), Pakistan, and to the Faculty of Engineering at the University of Nottingham for sponsoring this research. This work was supported by the Engineering and Physical Sciences Research Council (Grant No. EP/H003479/1). The authors would also like to thank the International GNSS Service, the Multi-GNSS Experiment Service, NovAtel Inc., Spirent Communications plc and Leica Geosystems AG for supporting this research work. A special acknowledgement is given to Septentrio and, in particular, to Jean-Marie Sleewaegen for providing us with invaluable support during the entire research.

References

Ammar M (2011) Calibration of ionospheric scintillation and total electron content monitor receivers. M.Sc. Dissertation, University of Nottingham

Arikan F, Nayir H, Sezen U, Arikan O (2008) Estimation of single station interfrequency receiver bias using GPS-TEC. Radio Sci. https://doi.org/10.1029/2007RS003785

Coco DS, Coker C, Dahlke SR, Clynch JR (1991) Variability of GPS satellite differential group delay biases. IEEE Trans Aerosp Electron Syst 27(6):931–938
Defraigne P, Aerts W, Cerretto G, Cantoni E, Sleewaegen JM (2014) Calibration of Galileo signals for time metrology. IEEE Trans Ultrason Ferroelectr Freq Control 61(12):1967–1975
Dodson AH, Moore T, Aquino MH, Waugh S (2001) Ionospheric scintillation monitoring in northern Europe. In: Proceedings of ION ITM. Institute of Navigation, Salt Lake City, UT, Sept 11–14, pp 2490–2498
Durmaz M, Karslioglu MO (2015) Regional vertical total electron content (VTEC) modeling together with satellite and receiver differential code biases (DCBs) using semi-parametric multivariate adaptive regression B-splines (SP-BMARS). J Geod 89(4):347–360. https://doi.org/10.1007/s00190-014-0779-8
Dyrud L, Jovancevic A, Brown A, Wilson D, Ganguly S (2008) Ionospheric measurement with GPS: receiver techniques and methods. Radio Sci. https://doi.org/10.1029/2007rs003770
Galileo (2016) Galileo IOV satellite metadata. https://www.gsc-europa.eu/support-to-developers/galileo-iov-satellite-metadata
Hauschild A, Montenbruck O (2016) A study on the dependency of GNSS pseudorange biases on correlator spacing. GPS Solut 20(2):159–171. https://doi.org/10.1007/s10291-014-0426-0
IS-GPS-200H (2014) Navstar GPS space segment/navigation user interface control document. http://www.gps.gov/technical/icwg/IS-GPS-200H.pdf
Jakowski N, Sardon E, Engler E, Jungstand A, Klaehn D (1996) Relationships between GPS-signal propagation errors and EISCAT observations. Ann Geophys 14(12):1429–1436
Jin R, Jin SG, Feng G (2012) M_DCB: matlab code for estimating GNSS satellite and receiver differential code biases. GPS Solut 16(4):541–548
Komjathy A, Sparks L, Wilson BD, Mannucci AJ (2005) Automated daily processing of more than 1000 ground-based GPS receivers for studying intense ionospheric storms. Radio Sci. https://doi.org/10.1029/2005RS003279
Lanyi G, Roth T (1988) A comparison of mapped and measured total ionospheric electron content using global positioning system and beacon satellite observations. Radio Sci 23(4):483–492
Leica Support Team – Personal Communication (email) (2016)
Li Z, Yuan Y, Fan L, Huo X, Hsu H (2014) Determination of the differential code bias for current BDS satellites. IEEE Trans Geosci Remote Sens 52(7):3968–3979. https://doi.org/10.1109/TGRS.2013.2278545
Li M, Yuan Y, Wang N, Li Z, Li Y, Huo X (2016) Estimation and analysis of Galileo differential code biases. J Geodesy 91(3):279–293. https://doi.org/10.1007/s00190-016-0962-1
Lin LS (2001) Remote sensing of ionosphere using GPS measurements. In: Proceedings of 22nd Asian conference on remote sensing, vol 1. Singapore, pp 69–74
Ma G, Maruyama T (2003) Derivation of TEC and estimation of instrumental biases from GEONET Japan. Ann Geophys 21(10):2083–2093
Mayer C, Becker C, Jakowski N, Meurer M (2011) Ionosphere monitoring and inter-frequency bias determination using Galileo: first results and future prospects. Adv Space Res 47(5):859–866
Montenbruck O, Hauschild A (2013) Code biases in multi-GNSS point positioning. In: Proceedings of ION ITM. Institute of Navigation, San Diego, California, Jan 29–27, pp 616–628
Montenbruck O, Hauschild A, Steigenberger P (2014) Differential code bias estimation using multi-GNSS observations and global ionosphere maps. Navigation 61(3):191–201
Mylnikova AA, Yasyukevich YuV, Kunitsyn VE, Padokhin AM (2015) Variability of GPS/GLONASS differential code biases. Results Phys 5:9–10
NovAtel Support Team – Personal Communication (email) (2016)
Otsuka Y, Ogawa T, Saito A, Tsugawa T, Fukao S, Miyasaky S (2002) A new technique for mapping of total electron content using GPS in Japan. Earth Planets Space 54(1):63–70
Rao GS (2007) GPS satellite and receiver instrumental biases estimation using least squares method for accurate ionosphere modelling. J Earth Syst Sci 116(5):407–411. https://doi.org/10.1007/s12040-007-0039-x
Sardón E, Rius A, Zarraoa N (1994) Estimation of the transmitter and receiver differential biases and the ionospheric total electron content from Global Positioning System observations. Radio Sci 29(3):577–586
Schaer S (1999) Mapping and predicting the Earth's ionosphere using the Global Positioning System. Ph.D. thesis, University of Bern
Van Dierendonck AJ (1999) Eye on the ionosphere: measuring ionospheric scintillation events from GPS signals. GPS Solut 2(4):60–63. https://doi.org/10.1007/PL00012769
Van Dierendonck AJ, Hua Q (2001) Measuring ionospheric scintillation effects from GPS signals. In: Proceedings of ION 57th annual meeting. Institute of Navigation, Albuquerque, NM, June 11–13, pp 391–396
Wang N, Yuan Y, Li Z, Montenbruck O, Tan B (2016) Determination of differential code biases with multi-GNSS observations. J Geod 90(3):209–228
Wilson BD, Mannucci AJ (1993) Instrumental biases in ionospheric measurements derived from GPS data. In: Proceedings of ION GPS 1993. Institute of Navigation, Salt Lake City, UT, Sept 22–24, pp 1343–1351
Yuan YB, Huo XL, Ou JK (2007) Models and methods for precise determination of ionospheric delay using GPS. Prog Natl Sci 17(2):187–196
Zhang Y, Wu F, Kubo N, Yasuda A (2003) TEC measurement by single dual-frequency GPS receiver. In: Proceedings of international symposium on GPS/GNSS. Tokyo, 351–358
Zhong J, Lei J, Dou X, Yue X (2015) Is the long-term variation of the estimated GPS differential code biases associated with ionospheric variability? GPS Solut 20(3):313–319

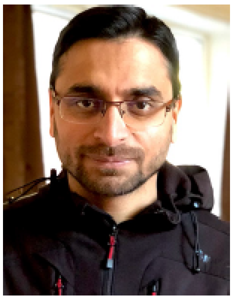

M. Ammar is a postgraduate researcher at the Nottingham Geospatial Institute of the University of Nottingham, UK. His research involves estimation and analysis of multi-GNSS instrumental biases. He received his B.Sc. in Civil Engineering from National University of Sciences and Technology, Pakistan, and completed his M.Sc. in Engineering Surveying and Space Geodesy from the University of Nottingham, UK.

M. Aquino is an Associate Professor at the Nottingham Geospatial Institute of the University of Nottingham in the UK. He pioneered the deployment of ionospheric scintillation and TEC monitoring receivers in Northern Europe in 2001. His research has focused on ionospheric effects on GNSS, including system vulnerability to ionospheric disturbances and relevant countermeasures.

S. Vadakke Veettil is a senior research fellow at the Nottingham Geospatial Institute of the University of Nottingham in the UK, involved in European Commission, European Space Agency and UK research council funded projects. Her research focuses on assessing the effects of space weather on GNSS receivers and positioning errors aiming to improve the modeling of scintillation and to develop mitigation tools.

M. Andreotti is a Senior GNSS Receiver System Designer at NovAtel Inc., Canada, since 2012. He received B.Sc. and M.Sc. Degrees in Electrical Engineering from CEFET, Brazil, and a Ph.D. in Engineering Surveying and Electrical Engineering from the University of Nottingham, UK. Marcus has 20+ years of experience in industry and academy, working with R&D groups in signal processing and hardware development in Brazil, the UK, New Zealand and Canada.

APPENDIX B

DCBS IN PRECISE CLOCKS ESTIMATION

The precise ionospheric free satellite clock estimate δt^{s*} does not reflect the true satellite clock offset δt^{s} but is corrupted by the ionospheric free linear combination $b^{s,3}$ of the individual code biases b_{P1}^{s} and b_{P2}^{s} (Schaer, 1999). The superscript 's' denotes the satellite and the subscripts P1 and P2 denotes the pseudoranges on L1 and L2 signals, respectively. Mathematically, this can be written as follows:

$$\delta \mathrm{t}^{\mathrm{s},3} = \delta \mathrm{t}^{\mathrm{s}} - b^{s,3} \quad \text{(B-1)}$$

where:

$$b^{s,3} = \left(\frac{f_1^2}{f_1^2 - f_2^2}\right) b_{P1}^{s} + \left(\frac{-f_2^2}{f_1^2 - f_2^2}\right) b_{P2}^{s}$$

or more simply:

$$b^{s,3} = k_1 b_{P1}^{s} + k_2 b_{P2}^{s} \quad \text{(B-2)}$$

where:

$$k_1 = \left(\frac{f_1^2}{f_1^2 - f_2^2}\right) \quad \text{(B-3)}$$

and

$$k_2 = \left(\frac{-f_2^2}{f_1^2 - f_2^2}\right) \quad \text{(B-4)}$$

Also, the satellite DCB for the P1 and P2 signal pair can be written as follows:

$$\mathrm{DCB}_{P1-P2}^{s} = b_{P1}^{s} - b_{P2}^{s} \quad \text{(B-5)}$$

Equations B-2 and B-5 can be written in matrix form as follows:

$$\begin{bmatrix} b^{s,3} \\ \mathrm{DCB}^{s}_{P1-P2} \end{bmatrix} = \begin{bmatrix} k_1 & k_2 \\ +1 & -1 \end{bmatrix} \begin{bmatrix} b^{s}_{P1} \\ b^{s}_{P2} \end{bmatrix}$$

Rearranging:

$$\begin{bmatrix} b^{s}_{p1} \\ b^{s}_{p2} \end{bmatrix} = \begin{bmatrix} k_1 & k_2 \\ +1 & -1 \end{bmatrix}^{\mathbf{-1}} \begin{bmatrix} b^{s,3} \\ \mathrm{DCB}^{s}_{P1-P2} \end{bmatrix}$$

$$= \frac{1}{-k_1 - k_2} \begin{bmatrix} -1 & -k_2 \\ -1 & k_1 \end{bmatrix} \begin{bmatrix} b^{s,3} \\ \mathrm{DCB}^{s}_{p1-p2} \end{bmatrix}$$

$$= \frac{1}{-(k_1 + k_2)} . (-1) \begin{bmatrix} 1 & k_2 \\ 1 & -k_1 \end{bmatrix} \begin{bmatrix} b^{s,3} \\ \mathrm{DCB}^{s}_{p1-p2} \end{bmatrix}$$

As $k_1 + k_2 = 1$,

$$\begin{bmatrix} b^{s}_{p1} \\ b^{s}_{p2} \end{bmatrix} = \begin{bmatrix} 1 & k_2 \\ 1 & -k_1 \end{bmatrix} \begin{bmatrix} b^{s,3} \\ \mathrm{DCB}^{s}_{p1-p2} \end{bmatrix}$$

From the above matrix,

$b^{s}_{P1} = b^{s,3} + k_2 \mathrm{DCB}^{s}_{P1-P2}$ ……………………………..………………. (B-7)

$b^{s}_{P2} = b^{s,3} + (-k_1) \mathrm{DCB}^{s}_{P1-P2}$ ………………………………………….. (B-8)

The equations for satellite clock offsets δt^{s}_{P1} and δt^{s}_{P2}, comprising of pure clock offset corrupted by individual code delays, for P1 and P2 signals, respectively, can be written as follows:

$\delta t^{s}_{P1} = \delta \mathrm{t}^{\mathrm{s}} - b^{s}_{P1}$ ……………………………………………………….. (B-9)

$\delta t^{s}_{P2} = \delta \mathrm{t}^{\mathrm{s}} - b^{s}_{P2}$ ……………………………………………………… (B-10)

Putting the values of true clock offset in terms of ionospheric free precise clock estimate from Equation B-1 and using equation B-7, equation B-9 can be expanded as follows:

$$\delta t_{P1}^{s} = (\delta \mathrm{t}^{s*} + \mathrm{b}^{s,3}) - b_{p1}^{s} = \delta \mathrm{t}^{s,*} + \mathrm{b}^{s,3} - \mathrm{b}^{s,3} - k_2 \mathrm{DCB}_{P1-P2}^{s}$$

$$\delta t_{P1}^{s} = \delta \mathrm{t}^{s,*} - k_2 \mathrm{DCB}_{P1-P2}^{s} = \delta \mathrm{t}^{s,*} + \frac{f_2^2}{f_1^2 - f_2^2} \mathrm{DCB}_{P1-P2}^{s} \ldots\ldots\ldots\ldots\ldots \text{(B-11)}$$

Similarly, it can be shown that:

$$\delta t_{P2}^{s} = \delta \mathrm{t}^{s,*} + k_1 \mathrm{DCB}_{P1-P2}^{s} = \delta \mathrm{t}^{s,*} + \frac{f_1^2}{f_1^2 - f_2^2} \mathrm{DCB}_{P1-P2}^{s} \ldots\ldots\ldots\ldots\ldots \text{(B-12)}$$

Equations B-11 and B-12 have been used with basic pseudorange observation equation to generate Equations 3.23 and 3.24 in the earlier Section 3.7.

APPENDIX C

ONE WAY ANALYSIS OF VARIANCE (ANOVA-I)

The Analysis of Variance (ANOVA) is one of the most powerful statistical techniques to test the hypothesis that the means of two or more experimental datasets are equal (NIST/SEMATECH, 2016). It works under the assumption that the sampled datasets are normally distributed. One way or one factor analysis of variance (ANOVA-I) is a special case of ANOVA for one factor of interest and is a generalisation of two-sample t-test. The two-sample t-test is used to determine whether two groups (levels) of a factor have the same mean. ANOVA-I generalises this to groups where the number of groups is greater than or equal to 2 (NIST/SEMATECH, 2016). For instance, in this research, the simulated data is collected through, say, 16 channels of a simulator. This means that the data collected has one factor (channels) in 16 groups. The ANOVA-I tests whether the channels have a significant effect on the collected data or not.

In MATLAB, the ANOVA-I test is implemented using the 'anova1' function. It returns a p-value, which if low, indicates that at least one of the population means differs from the others. The ANOVA table and a box plot are also generated as part of the 'anova1' function (ANOVA-I, 2015).

A standard *ANOVA Table* shows the between-groups variation (column) and within-groups variation (Error) and is given in Table C-1 (ANOVA-I, 2015).

Table C.1 Standard ANOVA Table (ANOVA-I, 2015)

Source	**SS**	**df**	**MS**	**F**	***p*-value**
Group (Between)	SSR	$k-1$	MSR= SSR/(k–1)	MSR/MSE	$P(F_{k-1,N-k}) > F$
Error (Within)	SSE	$N-k$	MSE= SSE/(N–k)		
Total	SST	$N-k$			

Here,

Source:	Source of the variability
SS:	Sum of squares due to each source
df:	Degrees of freedom associated with each source
MS:	Mean squares for each source (SS/df)
F:	*F*-statistic
Prob > F:	*p*-value, which is the probability that the *F*-statistic can take a value larger than the computed test-statistic value
k	Number of groups
N	Number of observations

For a set of data, a *box plot* (or box and whisker plot) represents the following graphically:

- Minimum Value
- Lower quartile i.e. 25th percentile
- Median
- Upper quartile i.e. 75th and
- Maximum Value

To draw a box plot, a box representing the interquartile range (IQR) is drawn from the lower quartile to the upper quartile. A vertical line is drawn which goes through the box at the median. The whiskers add and subtract 1.5 times the IQR to the upper and lower quartiles, respectively.

The notch in the box plot represents the confidence interval around the median and is normally based on the median ± $1.57 \times IQR/\sqrt{N}$ (David's Statistics, 2016). Figure C.1 shows an example of the notched box plot highlighting its major features.

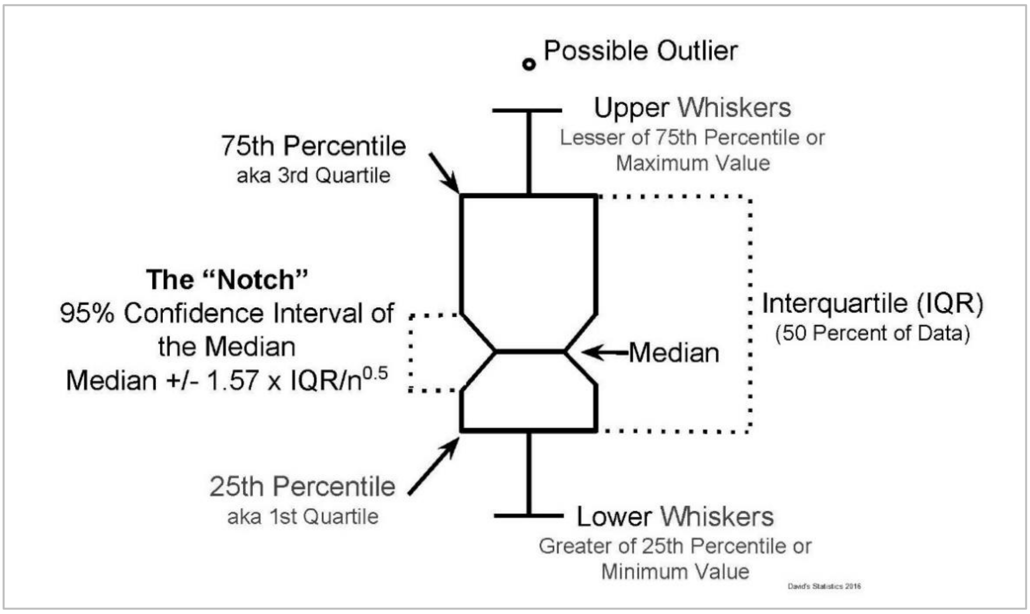

Fig. C.1 Features of a notched box plot (David's Statistics, 2016)

According to Chambers et al. (1983), if the notches of the two boxes in a notched box plot do not overlap, there is 'strong evidence' (i.e. 95% confidence) that their medians differ.

One limitation of ANOVA-I test is that it does not provide further information on which group means are different. Multiple comparison tests by using *multcompare* function in MATLAB can be run to perform multiple pairwise comparison of the group means (MultCompare, 2016).

Figures C.2 and C.3 represent an example each of the notched box plot and the multiple comparison of means plot. These were generated after running an ANOVA-I test on a Galileo based simulated data collected on NGI's simulator.

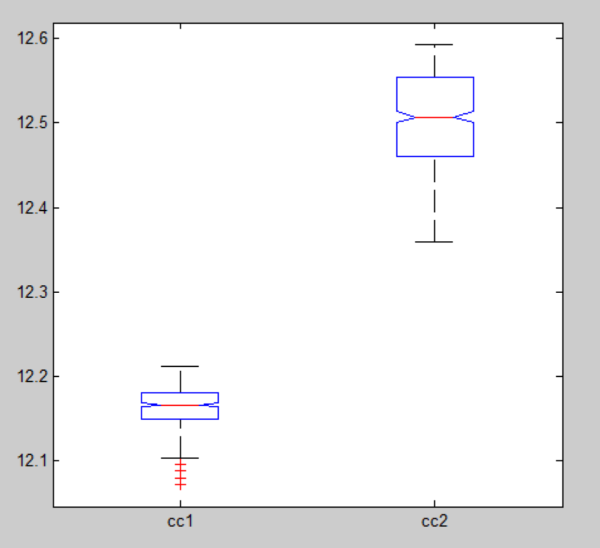

Fig. C.2 Notched box plot generated as part of this research from data (TEC) collected on channel card 1 (cc1) and channel card 2 (cc2) of NGI's simulator (Galileo only)

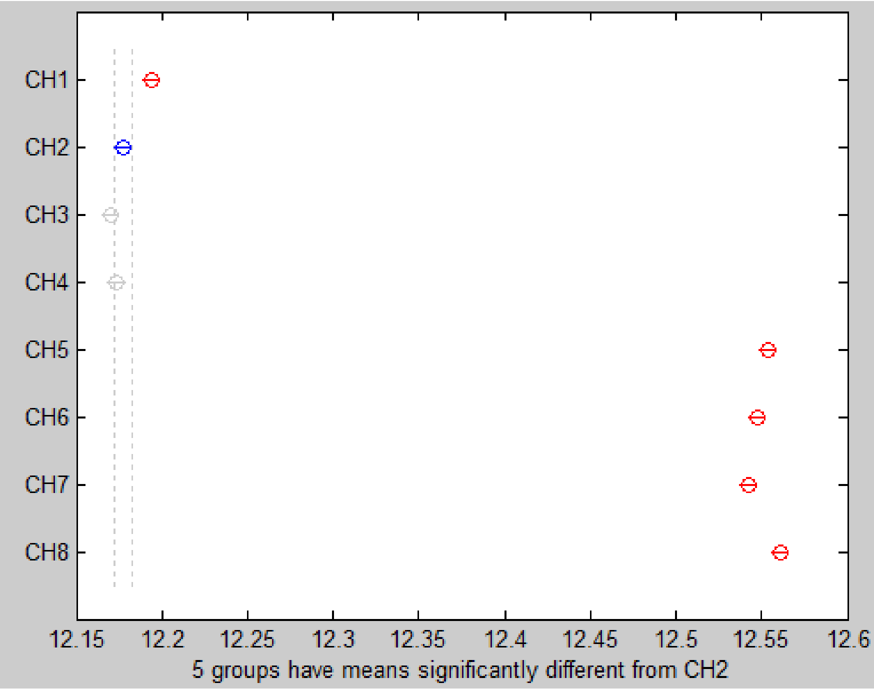

Fig. C.3 Plot generated after running Multcompare function (Multiple Comparisons of Means) in MATLAB for the data (TEC) collected using channel card 1 (CH1-CH4 channels) and channel card 2 (CH5-CH8) of the NGI's simulator (Galileo only)